DOCTORAATSPROEFSCHRIFT

2012 | Faculteit Wetenschappen

AlN thin films: stress, structural properties and optical phonons

Proefschrift voorgelegd tot het behalen van de graad van
Doctor in de Wetenschappen, Fysica, te verdedigen door:

Paulius POBEDINSKAS

Promotor: prof. dr. Ken Haenen

D/2012/2451/18

universiteit
hasselt

INSTITUUT VOOR
MATERIAALONDERZOEK
IMO-IMOMEC

Chairman:	Prof. Dr. Marc D’Olieslaeger *UHasselt & IMEC vzw*
Supervisor:	Prof. Dr. K. Haenen *UHasselt & IMEC vzw*
Members of the jury:	Prof. Dr. D. Depla *Universiteit Gent*
	Dr. J. D’Haen *UHasselt & IMEC vzw*
	Dr. V. Mortet *CNRS–LAAS*
	Dr. J. Pernot *Université Joseph Fourier & CNRS–Institut Néel*
	Prof. Dr. M.K. Van Bael *UHasselt & IMEC vzw*
	Prof. Dr. P. Wagner *UHasselt & IMEC vzw*

To my daugther Rugilė

Contents

Acknowledgements ix

List of abbreviations xi

Abstract xv

Samenvatting xvii

I State of the art 1

1 Aluminum nitride 3

1.1 Introduction 3

1.2 Deposition of AlN thin films 5

1.3 Stress in AlN thin films 6

1.4 Optical phonons in AlN thin films 6

1.5 Diamond 7

II Theory & Experiments 11

2 Experimental techniques 13

2.1 Thin film deposition 13

2.1.1 Reactive DC-pulsed magnetron sputtering 13

2.1.2 Types of thin film microstructure 15

2.1.3 Sample preparation 16

2.2 Stress measurements 18

2.2.1 Substrate curvature method 18

2.2.2 Radius of curvature 19
2.2.3 Etch-back experiment 21
2.3 UV-VIS-IR spectroscopy 21
2.3.1 Fundamental concepts 22
2.3.2 Light reflection and refraction at the interface 23
2.3.3 Transmission and reflection in thin films 26
2.3.4 Uniaxially anisotropic film 27
2.3.5 Influence of surface roughness 29
2.3.6 Experimental set-ups 30
2.4 Film thickness determination 33
2.5 Optical phonons in AlN 34
2.5.1 Theoretical model of dielectric functions 34
2.5.2 Experimental set-ups 40
2.6 NCD growth 41
2.7 Morphology 44
2.7.1 X-ray diffraction 44
2.7.2 Atomic force microscopy 44
2.7.3 Scanning electron microscopy 44

III Main results & Applications 45

3 Stress, structural properties and phonons 47
3.1 Stress 47
3.1.1 In-plane stress 47
3.1.2 Out-of-plane strain 50
3.2 Structural properties 53
3.2.1 XRD 53
3.2.2 AFM 54
3.3 Optical phonons 56
3.3.1 FTIR 57
3.3.2 Raman 62

4 Route towards applications **65**

4.1 AlN on metals 65

4.2 AlN & Diamond 70

4.2.1 AlN on NCD 70

4.2.2 NCD on AlN 70

5 Conclusions & Outlook **77**

Bibliography **81**

Publications **89**

Papers 89

Proceedings 90

Abstracts 90

Oral presentations 90

Poster presentations 92

Awards **95**

Acknowledgements

No one knows where, when and how it began. Some believe it began with the Big Bang theory, others say that space and time have always existed in an endless cycle of expansion and rebirth [1]. Zillion quantum of time has passed since then[1] and I was created by my parents, who were crated by theirs, *etc*. Thus, thank you all.

However, let's focus on perceptible events that shaped my Brownian motion through the space-time continuum towards the current point. The oldest event that I can recall and assign as deflective towards the science was my class-fellow Tomas Zaveckas,[2] thank you man! After this, somehow I beat through the infernal thickets and brush to reach my *Alma mater*. Here, I would like to thank dr. Stasys Tamošiūnas, who directed me towards the III-V semiconductor's lab when I was searching for my path to science. As well, not forgetting all my colleagues[3] at Institute of Applied Research, Vilnius University, that educated me. My deep appreciation for you, Ačiū. Well, action of some of them[4] caused me to collide with my wife Alina. Needless to say, how much grateful I am to her. Shortly after, we got trapped in deep defect level of Grenoble. Pierre Muret, Julien Pernot,[5] Pierre-Nicolas Volpe[6] *et al.* provided light relief there, whereas Joël Chevrier guided through the maze of Master studies, Merci.

Unconsciously predestined from the beginning of an inexplicable journey, now I am here at IMO, WBGM group. I want to thank all those who interacted and changed my quasi-momentum during this time period (see the next page).

Just before you will approach the names of people of merit, think deeper that all of these events and every person had their prehistorical random sequence of events too... Anyway, I am happy being in the universe that I am in now, as you never can tell what is in the parallel one.

Finally, thank you for reading this thesis.

[1] Since when?
[2] He was spinning a yarn about antimatter.
[3] You can find all their names in publications of year 2005–2007 where I am a co-author.
[4] Artūras Žukauskas, Gintautas Tamulaitis, and Rolandas Tomašiūnas.
[5] Still trapped.
[6] Successfully emitted.

People of merit:

Ken Haenen,[7]
Vincent Mortet,[8]
Johnny Baccus,[9]
Miloš Nesládek,[10,11]
Jean-Christophe Bolsée,[12,13]
Stoffel Janssens,[14]
Boumédiène BenMoussa,[15]
Yasodhaadevi Balasubramaniam,[16]
Wiebke Janssen,[6,17,18]
Pieter Robaeys,[19]
Wim Dexters,[13,18]
Weng Siang Yeap,[11]
Farnoosh Vahidpour,[20]
Matthew McDonald,[11]
Giedrius Degutis,[18,21]
Andrada Lazea,
Michaël Daenen,
Wim Deferme,[22]
Jan D'Haen,[23]
Bart Ruttens,[24]
Erik Thoonen,[25]
Christel Willems,[26]
Hilde Pellaers,[26]
Gopala Krishna Thalluri,[27]
Bart Van Grinsven,[28]
Linny Baeten,[28]
Bert Conings,[28]
Lars Grieten,[29]
Sabine Bertho,
Emilie Bourgeois,
Dieter Croux,
Fortunato Piersimoni,
Donato Spoltore,
Hong Yin,
Sathia Punniyakoti,[27]
Marc Saitner,
Lianchen Shan,
Marina Boussé,[30,31]
Lea Verboven,[31]
Rerlinde Heymans,[31]
Lisette Luyckx,[30,31]
Marc D'Olieslaeger,[32]
Jan Geebelen,[33,34]
Pieter Van Moll,[33,34]
Eli Slenders,[33]
Jan Kapteijn den Bouwmeester,[33]
Sidney Goossens,[33]
et al.

Paulius Pobedinskas
April 2012

[7] For changing a symbol arrangement in the array of symbols dedicated for transferring the information of my work.
[8] For giving the initial direction for my doctoral studies.
[9] For helping to overcome all the technical barriers that have risen in my path of PhD study.
[10] For a publication in Nature.
[11] Thank you in advance.
[12] For driving together ≈ 20 000 km.
[13] For AFM images.
[14] For sharing a secret how to arrange carbon atoms into $Fd\bar{3}m$ space group symmetry.
[15] For spiritual thoughts.
[16] For showing the path of truth.
[17] Für das Schlossbergwandern.
[18] For doing the last minute experiment.
[19] For something else.
[20] For asking wise questions.
[21] For the Raman measurements.
[22] For calmness.
[23] For SEM images.
[24] For XRD measurements.
[25] For allowing to use outdated software.
[26] For keeping us save in the chemistry lab.
[27] For a good mood.
[28] For the escape from Alcatraz.
[29] For honest-to-goodness.
[30] For obtaining unobtainable articles.
[31] For helping with all administrative processes.
[32] For solidity.
[33] For being test students in my teaching practice.
[34] For measuring stress on $\mathcal{S}_{50\%}$ samples.

List of abbreviations

Abbreviations

AFM	atomic force microscopy
APM	NH_4OH (27%), H_2O_2 (30%) and DI H_2O mixture (1:1:5 ratio by volume)
AVG	average
CVD	chemical vapor deposition
DC	direct current
DI	deionized
DLS	dynamic light scattering
ESRF	European Synchrotron Radiation Facility
EM	electromagnetic
FTIR	Fourier transform infrared
FWHM	full width at half maximum
IMO	Instituut Voor Materiaalonderzoek (Institute for Materials Research)
IR	infrared
LO	longitudinal optical
MBE	molecular beam epitaxy
MOCVD	Metal-organic chemical vapor deposition
MW PE	microwave plasma enhanced
NCD	nanocrystalline diamond
ND	nanodiamond
NIST	National Institute of Standards and Technology, Gaithersburg, MD, USA
PLD	pulsed laser deposition
PVD	physical vapor deposition
RF	radio frequency
RMS	root mean square
SEM	scanning electron microscopy
SPM	H_2SO_4 (95%) and H_2O_2 (30%) mixture (1:1 ratio by volume)
TEM	transmission electron microscopy
TO	transversal optical
UV	ultraviolet
VIS	visible
XRD	X-ray diffraction

Chemical elements & compounds

Al aluminum
AlN aluminum nitride
Al_2O_3 sapphire
Ar argon
CF_4 tetrafluoromethane
CH_4 methane
Cr chromium
Cu copper
H_2 hydrogen
HCl hydrogen chloride
HNO_3 nitric acid
H_2O water
H_2O_2 hydrogen peroxide
H_3PO_4 orthophosphoric acid
H_2SO_4 sulphuric acid
Mo molybdenum
N_2 nitrogen
Nb niobium
NH_4OH ammonium hydroxide
O_2 oxygen
Pt platinum
Si silicon
Ta tantalum
Ti titanium
V vanadium
W tungsten
Xe xenon
Zr zirconium

Symbols

A variable coefficient
$\mathcal{A}_\mathrm{H}$ the Hamaker constant (J)
B variable coefficient
$\vec{B}$ magnetic-flux density (T)
C variable coefficient
C_{ij} elastic stiffness constants (GPa)
c_0 speed of light in vacuum, $c_0 = 299\,792\,458$ m/s [2]
$\vec{D}$ electric-displacement density (C/m^2)
d_0 distance of closest approach between a surface and ND particle (≈ 0.3 nm)
$\vec{E}$ electric-field strength (V/m)
e Euler's number, $2.7182818284\,5904523536\,0287471352\ldots$
F oscillator strength
$\mathcal{F}$ force (N)
f function

$\vec{H}$	magnetic-field strength (A/m)
h	thicknesses (nm)
I	irradiance (W/m^2)
$\Im$	imaginary part of complex number
i	imaginary unit
j	integer
$\vec{k}$	angular wavenumber (rad/m)
$\mathcal{M}$	bending momentum (N m)
m	integer
N	number of points
$\tilde{N}$	complex index of refraction
n	index of refraction, the real part of complex index of refraction, $\Re(\tilde{N})$
O	the least-significant terms of approximation to a mathematical function
P	power (W)
p	variable exponent
$\mathcal{R}$	radius of curvature (m)
$\mathbb{R}$	photometrically measurable reflectance
$\Re$	real part of complex number
R	total reflected amplitude
r	the Fresnel reflection coefficient
$\tilde{r}$	radius of adhering particle (nm)
$\vec{r}$	position vector (m)
S	surface scattering factor
$\mathcal{T}$	temperature (K)
$\mathbb{T}$	photometrically measurable transmittance
T	total transmitted amplitude
t	the Fresnel transmission coefficient
v	speed of light in medium (m/s)
W	line-width (cm^{-1})
w	wavenumber (cm^{-1})
x	distance (mm)
Y	the Young's modulus (GPa)
y	height of the substrate (nm)
z	distance from substrate/film interface (nm)
β	phase angle or phase shift (rad)
$\delta_{j,m}$	Kronecker delta, $\delta_{j\neq m} = 0$ and $\delta_{j=m} = 1$
ϵ	out-of plain strain
ε	permittivity (F/m)
ε_0	permittivity of free space, $\varepsilon_0 = \frac{1}{\mu_0 c} = 8.854\,187\,817\ldots$ F/m [2]
η	ratio
θ	angle of incidence, notation used in XRD
κ	extinction coefficient, the imaginary pert of complex index of refraction, $\Im(\tilde{N})$
λ	wavelength (nm)
μ	permeability (N/A^2)
μ_0	permeability of free space, $\mu_0 = 4\pi \times 10^{-7}$ N/A^2 [2]
ν	Poisson's ratio
π	$3.1415926535\,8979323846\,2643383279\,5028841971\ldots$

ρ	surface roughness (nm)
ϱ	density (cm^{-3})
σ	in-plane stress (GPa)
τ	lifetime (ps)
ϕ	angle of incidence (0) and refraction (1,2) (degree)
χ	electric susceptibility
ω	angular frequency (rad/s)
Γ	damping constant (cm^{-1})
Δ	absolute error
Φ	radiant flux (W)
Ψ	throughput of an integrating sphere
$\hbar$	the reduced Planck's constant equivalent $\frac{1}{2\pi c_0} = 5.308\,837\,458\,\mathrm{ps\,cm^{-1}}$

Abstract

Thin aluminum nitride (AlN) films of different thickness are deposited by DC-pulsed magnetron sputtering under identical conditions on sapphire (0001) and silicon (100) substrates, and sputtered polycrystalline chromium layers. An investigation of the residual stress, morphology and structural properties is carried out. The thickness of the films covers the range from 17 nm to ≈3900 nm. A higher compressive residual stress is measured for the thinner films and the presence of a stress gradient is proven. X-ray diffraction (XRD) studies show that all AlN films are achieved with perfect *c*-axis orientation perpendicular to the film surface and that the films are biaxially strained. XRD rocking curves reveal that AlN films on sapphire are highly oriented for all film thicknesses, whereas AlN film growth on silicon and Cr layers starts highly disoriented while the film quality improves with film thickness. Surface analysis by atomic force microscopy (AFM) shows a continuous film roughening and decrease of grain boundary density with increasing film thickness.

The study of the vibrational properties of AlN thin films is performed. The frequencies and lifetimes of the E_1(TO) and A_1(LO) optical phonons are calculated from Fourier transform infrared spectra using the factorized model of a damped oscillator. Additionally, using the Raman technique the E_2^2 phonon mode is investigated. We analyze the structural properties by the XRD technique to correlate the elongation of phonon lifetimes with increasing film thickness. The lifetimes of the phonon modes in AlN thin films are compared to the values in a single crystal.

Finally, the route towards the applications of AlN is analyzed. AlN is deposited on various metals and the film quality is investigated by the XRD and Raman techniques. The combination with nanocrystalline diamond (NCD) is elaborated. The surfaces of AlN, and Si as comparison, are exposed to different gas discharge plasmas (Ar, CF_4, H_2, N_2, O_2) and the colloidal seeding procedure of the surfaces with nanodiamond (ND) particles is followed. AFM reveals different seeding densities after different plasma pretreatment. It is shown that the Van der Waals (VdW) forces plays a role in ND adhesion to the surface. The surface roughening changes the nucleation density proportionally to the VdW force that varies with roughness. Surface hydrogenation and fluorination enhances the seeding density on Si and AlN surfaces. In the latter case the seeding density improved by almost four orders of magnitude compared to an untreated surface. This allowed to grow 60 nm thick pinhole-free NCD films on AlN.

Samenvatting

Dunne aluminium nitride (AlN) films van verschillende dikte werden afgezet met behulp van DC-pulsed magnetronsputteren. Hierbij werd gebruik gemaakt van identieke condities met saffier (0001) en silicium (100) substraten, en gesputterde polykristallijne lagen van chroom. De restspanning, de morfologie en de structurele eigenschappen werden onderzocht voor films met een dikte variërend tussen 17 nm en ≈ 3900 nm. Een hogere resterende drukspanning werd gemeten voor de dunnere films en de aanwezigheid van een spanningsgradiënt werd aangetoond. X-stralendiffractie (XRD) resulaten toonden aan dat alle AlN afgezet werden met de *c*-as loodrecht op het substraat, maar dat de films biaxiale spanning vertonen. De zogenaamde XRD "rocking curves" lieten zien dat de AlN films op saffier voor alle filmdikten hoogst georiënteerd zijn, terwijl bij AlN op Si en Cr de filmgroei nietgeoriënteerd begint maar dat de filmkwaliteit met filmdikte verbeterde. De analyse van de oppervlakken met atoomkrachtmicroscopie (AFM) liet een continue stijging van de oppervlakteruwheid zien in functie van de filmdikte, samen met een daling van de dichtheid van de korrelgrenzen.

De studie van de vibrationele eigenschappen van dunne AlN films werd uitgevoerd. De frequenties en de levensduur van de optische fononen E_1(TO) en A_1(LO) werden berekend op basis van Fourier infrarood spectra, gebruik makend van het in factoren ontbonden model van een gedempte oscillator. Bovendien werd met Raman spectroscopie het gedrag van het E_2^2 fonon onderzocht. De structurele eigenschappen werden opnieuw met XRD onderzocht om de levenduur van de fononen met stijgend filmdikte te correleren. Deze waarden werden vergeleken met bekende waarde verkregen op monokristallijn AlN.

Tot slot werden het Si en AlN oppervlak blootgesteld aan verschillende plasmas (Ar, CF_4, H_2, N_2, O_2), waarna het een colloïdale oplossing met nanodiamantdeeltjes (ND) gebruikt werd als voorbehandeling. AFM toont onmiskenbaar grote verschillen in kiemdichtheid aan na verschillende plasmavoorbehandelingen. Er werd aangetoond Van der Waals krachten (VdW) een belangrijke rol spelen in de adhesie van ND aan het oppervlakt. Het opruwen van het oppervlak veranderde proportioneel de nucleatiedichtheid via de VdW-kracht die op haar beur met de oppervlakteruwheid varieert. De hydrogenering en fluorinatie van zowel Si als AlN verbeterde de nucleatiedichtheid. In het laatstgenoemde geval steeg de dichtheid met vier grootteordes in vergelijking met het onbehandelde oppervlak. Dit stond toe om compleet gesloten 60 nm dikke nanokristallijne diamantfilms op AlN te groeien.

Part I

State of the art

Chapter 1

Aluminum nitride

This Chapter gives an overview of aluminum nitride (AlN), rising the fundamental problems that are currently addressed for the research and device development. In the last Section of this Chapter, the combination of thin polycrystalline diamond films with AlN are discussed.

1.1 Introduction

Over the last two decades there has been growing interest in III-V nitrides [3–6]. They have been recognized for their marvelous properties, leading to their use in numerous semiconductor device applications. In this group, aluminum nitride (AlN) stands out with extreme properties [5, 7] (Fig. 1.1). Having the widest direct band gap (6.2 eV) among semiconductors makes it a key component of deep-ultraviolet light emitting diodes [8–12]. Furthermore, AlN is a suitable substrate material for GaN which in turn is essential for solid-state lighting [13]. High breakdown voltage of 1.5×10^6 V/cm [7], high resistivity of more than 5×10^{13} Ω cm [14] and one of the most thermally stable among the piezoelectric materials [15], promote AlN to be used for high-power, high-temperature applications [16–19]. Moreover, high sound velocities of 6 333 m/s and 10 127 m/s for shear and longitudinal waves, respectively, render AlN extremely attractive for high-frequency microelectronic devices [20–23], acoustic wave devices, e.g. SAW filters, and micro-electro-mechanical systems (MEMS), e.g. micro-cantilevers [24]. Therefore, it is also foreseen to replace other more conventional piezoelectric materials in acoustic sensors [25–27]. However, for most of the mentioned applications, the properties of the active or supporting layers are crucial for their performance.

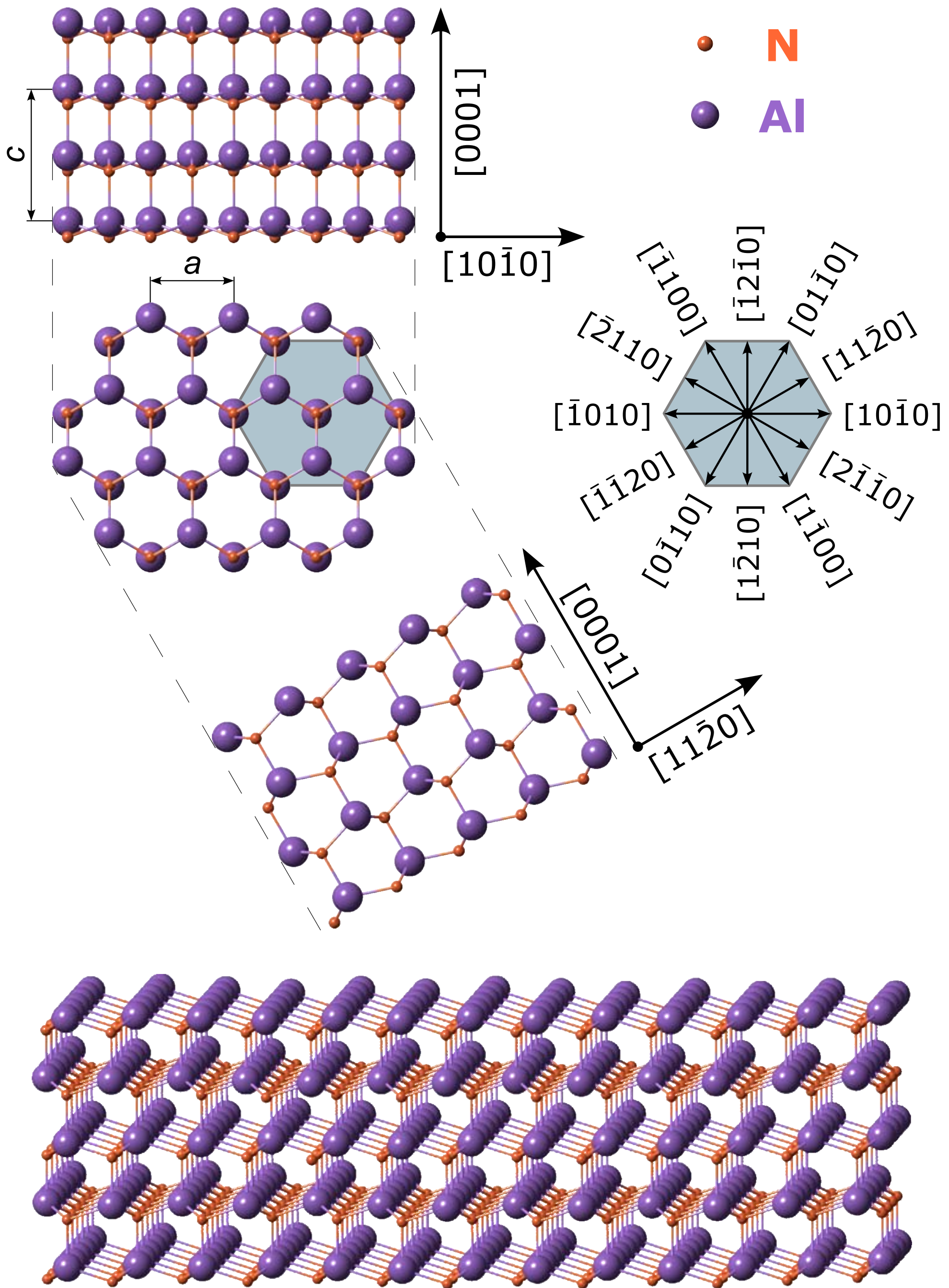

Figure 1.1: Hexagonal close-packed (hcp) aluminum nitride crystal structure belongs to the C_{6v}^4 ($P6_3mc$) space group symmetry.

1.2 Deposition of AlN thin films

AlN thin films can be achieved by various techniques (Fig. 1.2). There are two main process groups: physical and chemical vapor deposition (PVD and CVD, respectively). Each of it is subdivided into particular deposition techniques, which lead to AlN thin film deposition [28]. By means of CVD, plasma-enhanced CVD (PE CVD) [29], metalorganic chemical vapor deposition (MOCVD) [30], and thermal CVD [31] are available. On the other side, PVD methods divide into subgroups that differ in their physics, i.e. thermal and sputtering processes. The thermal techniques, in which AlN or Al is heated in reactive atmosphere, are the reactive evaporation [32], pulsed laser deposition (PLD) [33] and molecular beam epitaxy (MBE) [34].

The sputtering technique offers low temperature deposition of thin films with uniform composition and excellent adherence to the substrate [35]. In sputter deposition a material from a target, e.g. aluminum (Al), is ejected by bombarding it with energetic ions. If instead of an inert gas, usually argon, a reactive gas, e.g. nitrogen (N_2), is introduced into the sputtering chamber a chemical reaction between ejected aluminum and nitrogen ions take place and AlN is deposited on a substrate. Thus one gets so-called reactive sputtering deposition [36]. A permanent magnet behind a target is used to create a magnetic field in a closed-loop that traps electrons and reshapes their trajectory into a cycloidal path. Hereby the probability of ionization of the sputtering gas and hence the sputtering efficiency increases. During the process AlN layers form on the target and electrically insulates the target from the plasma, stops local sputtering and causes arcing. To overcome this, radio frequency (RF) sputtering has been introduced. However, RF power supplies are expensive. Therefore, direct current (DC) pulsed [37] and high power impulse [38] magnetron sputtering has been developed for the deposition of highly adherent, uniform and dense coatings of nitrides.

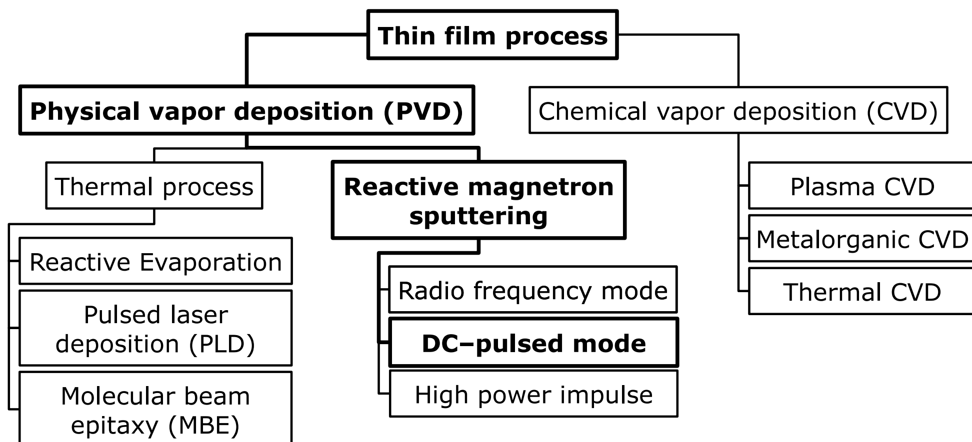

Figure 1.2: Schematic view of thin film deposition processes which are used to achieve AlN thin films.

1.3 Stress in AlN thin films

In general during manufacturing of thin films, MEMS and other devices stress is generated in both the substrate and the deposited films. Excessive film stresses can lead to deformation, cracking, delamination and other failures that can render a device unusable. Accurate assessment of the deformation caused by film stress is critical for developing controllable processes and producing high quality devices.

For devices based on AlN, fabrication and development, one is in need to know well this material. Most of the material properties depend on the distance between nearest neighbor atoms, which in turn is influenced by the stress in the film. Thus this changes the device performance or may lead to its malfunction, e.g. high stress in the AlN layer on a micro-cantilever bends and/or even breaks it (Fig. 1.5 (a)). Mechanical stress in thin films is quasi-unavoidable in heteroepitaxial growth due to the lattice mismatch and difference in thermal expansion coefficients of film and substrate. However, as the stress in the film is very much influenced by the used growth process and conditions [39], it means that stress engineering and control becomes possible. As demonstrated, sputtered thin AlN films show different properties for different film thickness [40]. One of these, the in-plane stress, had different values for different film thickness similarly as the results of Machunze and Janssen [41] on titanium nitride (TiN), where the authors proved that a stress gradient exists in their polycrystalline thin films.

In Chapter 3.1 AlN films of different thickness deposited by reactive DC-pulsed magnetron sputtering on silicon (100) and sapphire (0001) substrates are investigated. The silicon (100) substrates are of special interest because they are widely used in silicon device technology, whereas *c*-sapphire is one of the best lattice matched materials for AlN and is commonly used for optoelectronic devices. This investigation is focused on the presence of stress in AlN thin films and their morphology, which reveals that the substrate material and the subsequent quality of grown AlN determines the in-plane stress evolution with film thickness. Additionally, an etch-back experiment was done to prove the existence of a stress gradient in the films.

1.4 Optical phonons in AlN thin films

Thermal conduction, lattice specific heat and carrier scattering at high temperature are primarily determined by phonons [42]. In the case of high-current density or high photoexcitation, situations that play an important role in high power applications, polar optical phonons form the major energy relaxation path for hot carriers in polar semiconductors [43, 44]. Subsequently, generated zone-center optical phonons decay into zone-edge acoustic ones, which provide an efficient loss path for the excess energy. However, if the generation rate for optical phonons is higher than their decay a hot phonon population will emerge, slowing down the cooling process of carriers by optical phonon re-absorption and hampering device performance. Additionally,

the fundamental role of the optical phonon lifetime in the thermal conductivity of semiconductors was recently demonstrated [45].

Although the lifetimes of phonons are well examined in single crystal AlN by the Raman scattering technique [46–49], much less attention is devoted to infrared (IR) spectroscopy, where the lifetime of optical phonons can also be estimated as shown by Kazan *et al*. on a AlN single crystal [50]. IR spectroscopy is the most quantitative technique and can be easily implemented for thin film analysis, whereas the Raman technique causes difficulty when the backscattering configuration from the film cross-section needs to be engaged (Tab. 2.2). Up to now, no reports attempt to estimate the phonon lifetimes in AlN thin films because of undesirable defect levels in such films, which hinder the fundamental phonon behavior. The few investigations of vibrational properties of AlN thin films with different thickness that were made [51,52], focus mostly on the analysis of phonon frequencies and stress in such films. Moreover, the properties of sputtered AlN thin films are influenced by their thickness [40], complicating their analysis.

Chapter 3.3 focuses on the accurate determination of the energy and lifetime of optical phonons in AlN thin films based on a combination of optical experiments and theoretical modeling. The investigation of the films is performed by Fourier transform infrared (FTIR) spectroscopy recording the transmission spectra under normal and oblique angles. With the intent to extract the properties of the E_1(TO) and A_1(LO) optical phonon modes, simulations of the spectra were made using the factorized model of a damped oscillator, taking into account the presence of birefringence and the thin film interference phenomenon. As a result the E_1(TO) and A_1(LO) phonon modes were characterized by their energy and lifetime. An additional correlation with the stress and morphology of the films lead to a better fundamental understanding of the observation.

1.5 Diamond

CVD diamond is a versatile material with extreme mechanical, thermal, electronic and optical properties. Because of its very good chemical stability and bio-inertness, it is currently being studied for a range of applications that make use of its surface and bulk properties, including novel generation of neuroprosthetics [53,54] and (bio-sensing) diamond-based acoustic devices [25,27]. However, diamond does not show piezoelectricity and a heterostructure with a good piezoelectric material, like AlN, is a prerequisite to fulfill the promising role that diamond is envisaged to play. Nevertheless, there are still many issues that need to be overcome to reach the full potential of AlN/diamond heterostructures. One of those issues is the deposition of AlN on diamond and vice versa, diamond growth on AlN.

The synthesis of around 100 nm thin nanocrystalline diamond (NCD) films by the microwave plasma enhanced CVD (MW PE CVD) technique has proven an enormous step forward for this material to show its potential in action [55,56]. However, the diamond nucleation step is critical for CVD of diamond on non-diamond substrates,

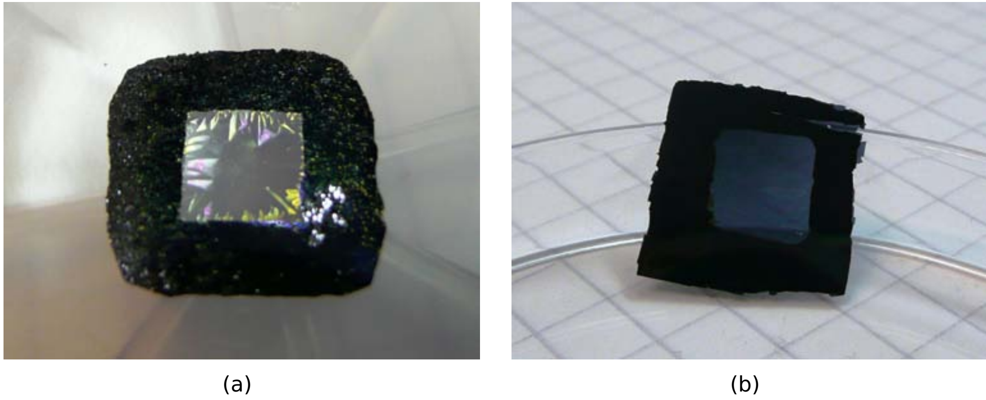

(a) (b)

Figure 1.3: Highly boron doped NCD membrane of 100 nm (a) and 200 nm (b) thickness and $6 \times 6\ mm^2$ in lateral size for soft X-ray monitor at ESRF, Grenoble, France.

i.e. for heteroepitaxial as well as polycrystalline growth. In general, growth on such foreign substrates requires artificial formation of diamond nucleation sites on the substrate's surface. The use of state-of-the-art seeding procedures based on water-based colloidal solutions of ultra dispersed nanodiamond powder, allow the deposition of closed films of less than 100 nm on 2D as well as 3D structures, minimizing deposition times while retaining an acceptable surface roughness [57]. In the seeding procedure the surface charge and nanodiamond (ND) particles' zeta-potential are the most important factors that determine the nucleation density after seeding [58]. The modification of Si surface by hydrogen plasma enables to reach extreme nu-

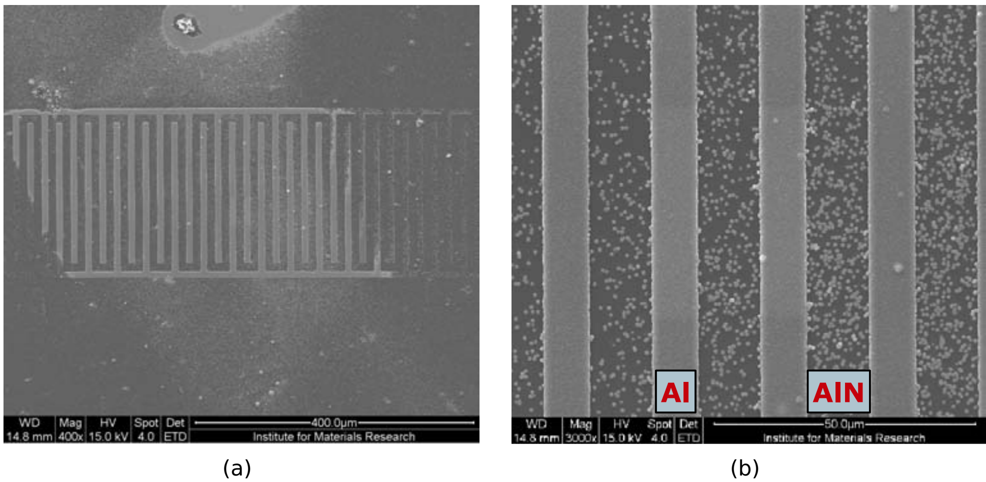

(a) (b)

Figure 1.4: An attempt to grow a NCD film on AlN with aluminum interdigitated transducer contacts. The dense and fully closed NCD layer is achieved on Al, whereas on AlN only spaciously separated NCD balls are grown.

cleation densities, which in turn allow to fabricate durable 100 nm thick NCD membranes (Fig. 1.4).

In the last part of this thesis the AlN deposition on NCD and NCD growth on AlN are analyzed. In latter case, it is shown that ND particles 10 nm in size do not adhere to the AlN surface by a simple Van der Waals force due to hydrophobic nature of AlN and a NCD film growth is impossible (Fig. 1.3). The adhesion of ND particles is strongly enhanced after surface hydrogenation or fluorination and allows the NCD coverage on AlN/Si cantilevers (Fig. 1.5 (c,d)).

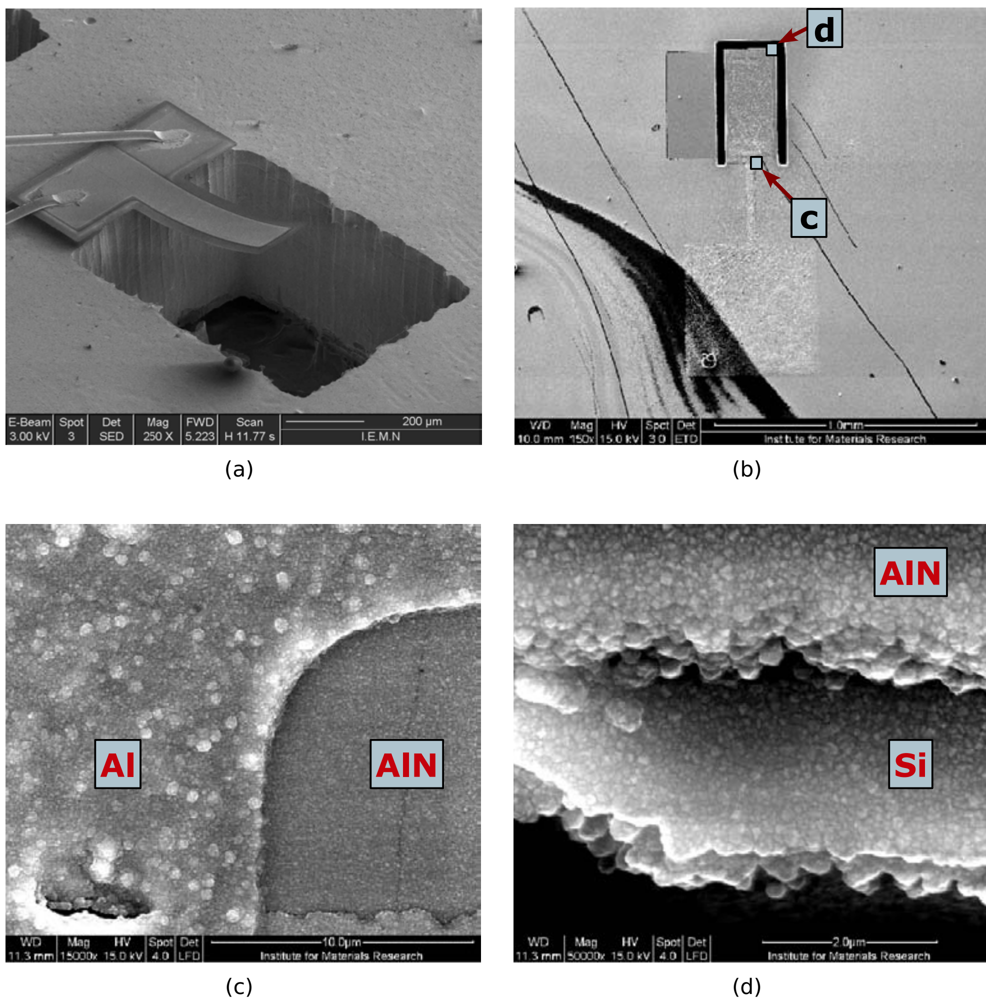

(a) (b) (c) (d)

Figure 1.5: (a) AlN/NCD cantilever, Ref. [24]. (b–d) AlN/Si cantilever, Ref. [59], covered with a NCD film at IMO.

Part II

Theory & Experiments

Chapter 2

Experimental techniques

In this Chapter, the overview of experimental techniques and underlaying fundamental theory are presented. The sample preparation by reactive DC-pulsed sputtering is shortly described in Section 2.1. The further sections compose the characterization techniques that were used for AlN thin film analysis. The main focus is put on the in-plane stress evaluation by substrate curvature method (Sec. 2.2) and optical characterization in the UV-VIS-IR spectral range (Sec. 2.3). In Section 2.4 thickness evaluation is shown. Additionally, all the experimental procedures are described briefly.

2.1 Thin film deposition

In the following Section the deposition technique and details of sample preparation is presented.

2.1.1 Reactive DC-pulsed magnetron sputtering

In order to deposit AlN films an aluminum (Al) target is sputtered using a nitrogen (N_2) gas discharge plasma with or without argon (Ar). When an electric potential difference is applied between two electrodes placed in a gas, electrons that are accelerated by the electric field collide with the gas atoms. This leads to excitation and ionization of the gas. The excited gas atoms relax by emission of photons, whereas the ionized atoms, i.e. ions, are accelerated by the electric field towards the cathode where the Al target is located. Due to ion bombardment Al atoms as well as the secondary electrons are released from the target. Sputtered Al diffuses through the plasma and reacts with the dissociation products from the N_2 gas to form AlN. The

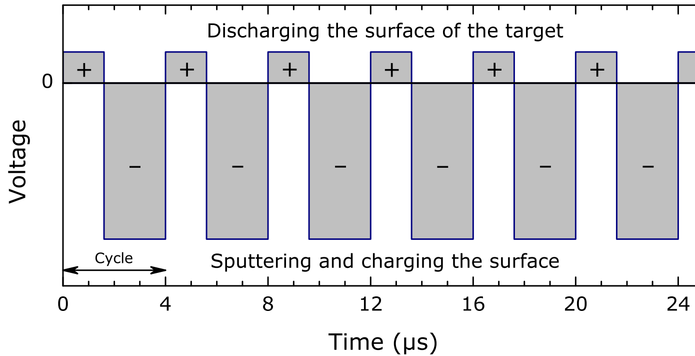

Figure 2.1: Pulsed voltage applied to the cathode during the sputtering process. Positive pulses are 1600 ns long, the cycle frequency is 250 kHz.

N_2 plasma also reacts with the target, hence the AlN is sputtered from there as well. Moreover, a dielectric layer accumulates positive charge, which causes arcing. To avoid this, a pulsed voltage is applied to the cathode with inverse voltage pulses, i.e. positive, in order to discharge the surface of the target (Fig. 2.1).

Sputtered species from the target reach a substrate with certain momentum[1]. This momentum depends on several parameters: (i) the voltage that is applied to the cathode, (ii) the mass of projectile ions, and (iii) the impact angle govern the yield of sputtering and momentum of ejected target atoms [60]. In order to eject atoms their bonds must be broken, hence (iv) the binding energy of the target material atoms determines the momentum of sputtered atoms. Sputtered atoms have to reach the substrate, thus here (v) the gas pressure rates the number of collisions, reducing the momentum of arriving atoms.

The atoms that are striking the surface have few options: to bounce immediately back from the substrate into the plasma, condensate or adsorb, sputter surface atoms or get implanted into the top layer. The probability of these events depends on the energy of the striking particle [35]. If the energy is not too high ($\gtrsim 10^{-2}$ eV) the atoms lose their energy on the impact and are physically adsorbed on the surface. The adsorbed atoms are initially not in thermal equilibrium with the substrate and move over the substrate surface. In this process they interact among themselves, forming clusters. Depending on the mobility of atoms, temperature of the substrate and the atom-surface interactions these clusters may either evaporate or grow. Clusters can grow parallel to the substrate by surface diffusion and perpendicular to it by direct impingement. Thus, the next stage is the growth of a thin film, where three primary growth modes are possible: (i) Volmer-Weber (island formation), (ii) Frank-van der Merwe (layer-by-layer), and (iii) Stranski-Krastanov (layer-plus-island).

[1] A product of a mass and velocity.

2.1.2 Types of thin film microstructure

A polycrystalline film's structure and morphology are classified in terms of structure zone models (SZM's), that are influenced by deposition parameters [61, 62]. The SZM's are constructed by the structure features dependence on the deposition temperature, considering the homologous temperature, i.e. T_s/T_m, where T_s is the substrate temperature and T_m is the melting point of the film material. These models are divided into I, T, II, and III zones, respectively with increasing T_s/T_m (Fig. 2.2).

When the ad-particles have little or no mobility, e.g. a low substrate temperature and/or small momentum of the incoming atom, they do not diffuse and stick to the growing film at the same place where they land; an amorphous-like columnar structure separated by voids develops[2] (zone Ia). Another zone, Ib, is similar as Ia and it differs by the presence of continuous bombardment by energetic sputtered particles. In this case the voids are filled by the particles and a more dense columnar structure evolves. At the elevated substrate temperature, zone Ic, the thermally induced mobility of the adatoms increases and they are able to diffuse on underlying crystal grains. Due to an anisotropy in growth rate of the different crystallographic planes, faceting of the grown film occurs in such a way that the grains are terminated by the planes of the lowest growth rate. This gives rise to a faceted columnar but random out-of-plane oriented structure. Also the voids between the columns are filled by the adatoms, thus the columns are not separated by the voids anymore, but by grain boundaries. In summary, zone I belongs to the temperature interval $0 < T_s/T_m < 0.2$ where neither the bulk diffusion nor the surface diffusion has remarkable value.

[2] Such structure can also emerge when atoms have higher mobility and a high deposition rate is present. Landed adatoms are buried by subsequently deposited ones before the first one can diffuse to another site.

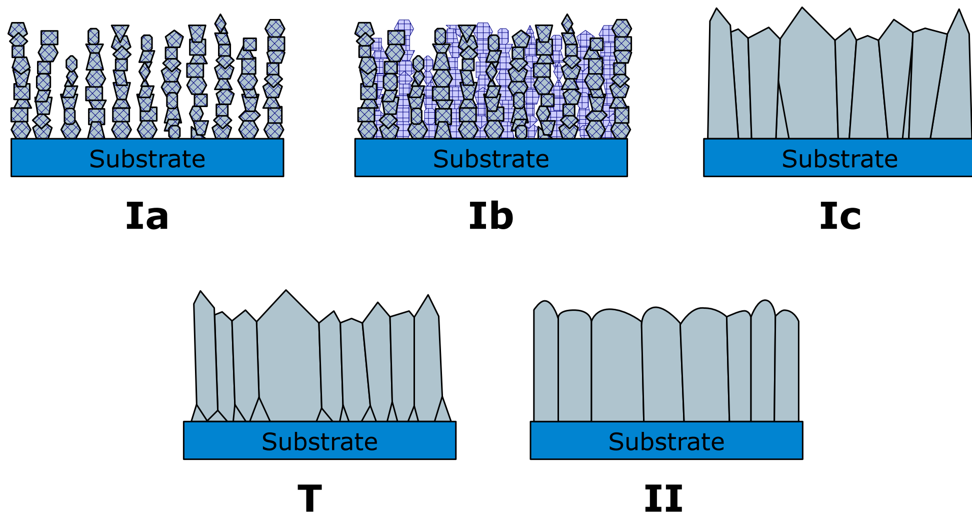

Figure 2.2: Schematic drawing of the structure zone models.

Further increase in temperature, proceeding to zone T $0.2 < \mathcal{T}_s / \mathcal{T}_m < 0.4$, increases the thermal mobility and enables adatoms to diffuse from one grain to another. The structure develops by the competitive growth of differently oriented neighboring grains. Therefore, the texture is changing with the thickness in this zone, while the grain boundary migration remains limited [61,62].

In the higher temperature range, zone II $0.4 < \mathcal{T}_s / \mathcal{T}_m$, the effect of the grain boundary migration becomes important. The first structure of randomly oriented small grains is dissolved gradually by the coalescence. The events are controlled by the interface and surface energy minimization.

As it will be seen in the next Section, AlN films were deposited without substrate heating and the $\mathcal{T}_s$ was approximately less that 500 K. The melting point temperature of AlN is around 3000 K [7] and thus $\mathcal{T}_s / \mathcal{T}_m \lesssim 0.17$, which corresponds to zone Ic [61].

2.1.3 Sample preparation

AlN thin films were deposited by reactive DC-pulsed magnetron sputtering on (100) oriented silicon, (0001) oriented sapphire substrates and metal interlayers on Si(100). The circular TORUS$^{(R)}$ balanced magnetron sputter source was provided by Kurt J. Lesker company.

Prior to deposition the substrates were ultrasonically cleaned in: acetone and ethanol, then rinsed in deionized water and dried under N_2 gas flow. The sputtering target was 99.9995% purity Al 4 inches in diameter, held on a water-cooled magnetron cathode. The distance between the target and the copper substrate holder was 5 cm. The target power supply was driven in a constant-power mode applying pulses of 1600 ns with 250 kHz repetition (Fig. 2.1). Before deposition the target was cleaned using Ar (99.9999%) gas discharge plasma for 10 min followed by a pre-sputtering stage, using the same conditions as the subsequent film deposition with shutter shielding the sample. The base pressure in the sputtering chamber was below 5×10^{-4} Pa, while the pressure during the deposition was kept at 0.6 Pa. The substrates were not additionally heated nor cooled during the deposition process. For two main series ($\mathcal{S}_{100\%}$ and $\mathcal{S}_{50\%}$, Tab. 2.1) the time of open shutter, i.e. deposition time, was varied and different film thicknesses were rendered in the range of 17 nm to 3900 nm.

The main investigation was focused on $\mathcal{S}_{100\%}$ series of samples that that were sputtered using a gas discharge plasma of pure N_2 (99.999%) on Si and Al_2O_3 substrates. Additional series of samples, $\mathcal{S}_{50\%}$, were deposited using a mixture of Ar and N_2 (1:1 ratio), on Si and Si covered with a chromium (Cr) interlayer (100 nm). The flow rates of gases were regulated by two mass flow controllers and the total gas flow rate was always kept constant at 50 sccm. AlN was sputtered on different metal interlayers under the same conditions as $\mathcal{S}_{100\%}$ series in oreder to investigate the quality of approximately 400 nm thick AlN film on mimicked electrical contacts (Sec. 4.1). For this reason metal thin films were sputtered on Si(100) substrates ($\mathcal{S}_{\mathrm{Metal}}$). Also thin films were sputtered under various powers ranging from 200 W to 900 W ($\mathcal{S}_{\mathrm{Power}}$). The deposition conditions of all investigated samples are summarized on Table 2.1.

Table 2.1: Deposition conditions of investigated AlN samples.

Deposition parameter	Series $\mathcal{S}_{100\%}$	Series $\mathcal{S}_{50\%}$	Series $\mathcal{S}_{\mathrm{Power}}$	Series $\mathcal{S}_{\mathrm{Metal}}$
Substrate	Si(100), Al_2O_3(0001), NCD[a], metal interlayer[b,c]: Al, Ti, V, Cr, Zr, Nb, Mo, Ta, W	Si(100), Cr	Si(100), Al_2O_3(0001), Al, Cr, Ta, W	Si(100)
Gas flow rate (sccm)	N_2 (50)	Ar:N_2 (25:25)	N_2 (50)	Ar (50)
Target	Al	Al	Al	Al, Ti, V, Cr, Zr, Nb, Mo, Ta, W
Target power P (W)	600	600	200, 300, 400, 500, 600, 700, 800, 900	150
Target-to-substrate distance (cm)	5	5	5	12
Base pressure (mPa)	< 0.5	< 0.5	< 0.5	< 0.5
Deposition pressure (Pa)	0.6	0.6	0.6	0.53
Deposition time (min)	0.25, 0.5, 1, 1.5, 3, 6, 12, 24, 48	0.25, 0.5, 1, 1.5, 3, 6, 12, 24, 48	20, 13, 9.5, 7.7, 6.3, 5.3, 4.7, 4.2[d]	15
Deposition rate[e] (nm/min)	64	81	$0.127 \cdot P$	45 (Al), 28 (Ti), 9 (V), 25 (Cr), 21 (Zr), 14 (Nb), 19 (Mo), 34 (Ta), 13 (W)
Film thickness[e] (nm)	17 – 3100	19 – 3900	≈ 500	680 (Al), 420 (Ti), 137 (V), 380 (Cr), 315 (Zr), 215 (Nb), 290 (Mo), 510 (Ta), 200 (W)

[a]Deposition time 15 min.
[b]Deposition time 6.25 min.
[c]For simplicity only the metal symbol is used for metal on Si(100) notation.
[d]20 min for 200 W, 13 min for 300 W, *etc.*, respectively.
[e]Relative error ±10%.

2.2 Stress measurements

In this Section the in-plane stress measurements by the substrate curvature method are described. The out-of-plain strain evaluation by X-ray diffraction (XRD) method is described in Section 2.7.1.

2.2.1 Substrate curvature method

Figure 2.3 illustrates the substrate bending due to an in-plane stress in the film that is deposited on a substrate. The growing film initially shrinks (Fig. 2.3 (a)) or expands (Fig. 2.3 (b)) relative to the substrate, e.g. due to surface tension forces or the lattice misfit. Compatibility requires that both the film and substrate have the same length. Therefore, the film stretches/contracts, while the substrate contracts/stretches. The tensile/compressive forces ($\mathcal{F}$) developed in the film are balanced by the compressive/tensile forces in the substrate. This combination is still not in mechanical equilibrium because of the uncompensated bending momenta ($\mathcal{M}$) that will elastically bend the substrate-film system in order to be compensated [35].

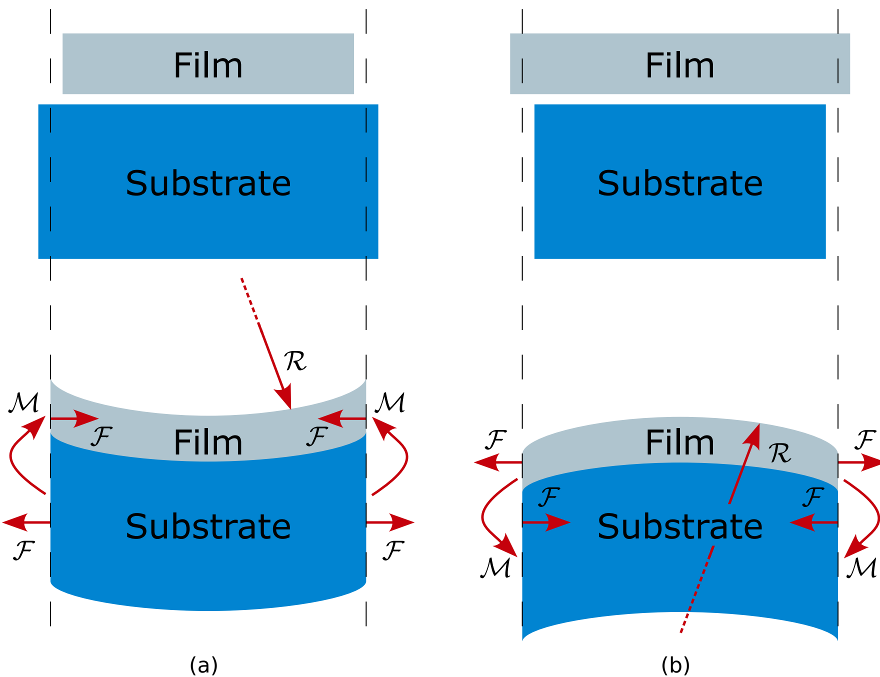

Figure 2.3: Substrate bending when a deposited thin film experiences tensile (a) and compressive (b) in-plane stress. $\mathcal{R}$ is the radius of curvature, $\mathcal{F}$ are the forces that act on the film and substrate to restore the equilibrium state, $\mathcal{M}$ are the bending momenta.

The in-plane stress σ in a film is calculated by the Stoney equation [63,64]:

$$\sigma = \frac{1}{6}\left(\frac{1}{\mathcal{R}_a} - \frac{1}{\mathcal{R}_b}\right)\frac{Y}{1-\nu}\frac{h_s^2}{h_f}\,, \tag{2.1}$$

where $\mathcal{R}_b$ and $\mathcal{R}_a$ are the radii of curvature of the substrate before and after the deposition of the film, respectively, Y is the Young's modulus and ν is Poisson's ratio for the substrate, h_s and h_f are the thicknesses of the substrate and film, respectively. The required substrate curvatures were measured with a DekTak$^{(R)}$ stylus profilometer. Elastic constants of the substrate materials, silicon and sapphire, were taken from the literature [65,66]. The thickness of the substrate was measured with an optical microscope, whereas the thickness of the films thicker than 100 nm was determined from the Fabry-Perot fringes in reflection and transmission spectra measured using a home-build system as described in chapter 2.3. The thickness of the thinner films was extrapolated with respect to the open shutter time during the deposition process.

2.2.2 Radius of curvature

The key of the stress measurements is the change of substrate's radius of curvature before and after the film deposition (Fig. 2.4 (a)). If the height of the substrate y is expressed as a continuous function of distance x along the substrate, $y = f(x)$, then the radius of curvature at any point are calculated as

$$\mathcal{R}(x) = \frac{\left[1+\left(\frac{dy}{dx}\right)^2\right]^{3/2}}{\frac{d^2y}{dx^2}}\,. \tag{2.2}$$

The measured surface profile is fitted with a parabolic function

$$y(x) = A + Bx + Cx^2\,, \tag{2.3}$$

with A, B and C the fitting parameters. Inserting the parabolic function into Eq. 2.2 yields

$$\mathcal{R}(x) = \frac{1}{2}\frac{\left[1+(B+2Cx)^2\right]^{3/2}}{C}\,. \tag{2.4}$$

Then the obtained function can be expanded as the Taylor series at the zero point, i.e. as the Maclaurin series,

$$\mathcal{R}(x) = \frac{1}{2}\frac{\left(1+B^2\right)^{3/2}}{C} + 3\sqrt{1+B^2}\,Bx + O(x^2)\,. \tag{2.5}$$

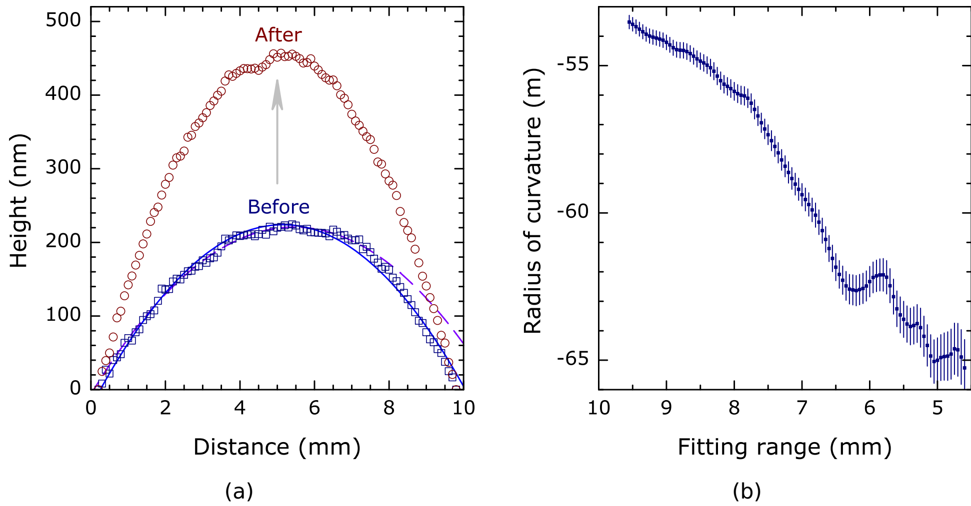

Figure 2.4: (a) Curvature of Si substrate before (squares) and after (circles) the deposition of 200 nm AlN film. The parabolic curves are fits made at different ranges: the whole measurement (solid curve), giving $\mathcal{R} = (-53.4 \pm 0.2)$ m, and the central zone of 4.6 mm (dashed curve), giving $\mathcal{R} = (-65.3 \pm 1.0)$ m. (b) Radius of curvature versus the fitting range.

If the second term is negligible one gets the radius of curvature independent of x

$$\mathcal{R} = \frac{1}{2}\frac{\left(1+B^2\right)^{3/2}}{C}\,. \tag{2.6}$$

The condition of negligibility

$$|C| \ll \left|\frac{1}{6}\frac{(1+B)^2}{B}\right| \tag{2.7}$$

was satisfied for all measurements of substrate curvature.

For the data fit a polynomial regression model of the second order is used and standard errors of the fitting parameter is estimated [67]. The absolute error of radius of curvature (Eq. (2.6)) is

$$\Delta\mathcal{R} = \sqrt{\left(\frac{\partial\mathcal{R}}{\partial B}\Delta B\right)^2 + \left(\frac{\partial\mathcal{R}}{\partial C}\Delta C\right)^2} \tag{2.8}$$

whereas the relative error is

$$\frac{\Delta\mathcal{R}}{\mathcal{R}} = \sqrt{\left(\frac{3B\Delta B}{1+B^2}\right)^2 + \left(\frac{\Delta C}{C}\right)^2} \tag{2.9}$$

Depending on the measurement length the fitting results vary and so does the calculated radius of curvature and its error (Fig. 2.4 (b)). Around 10% of the edge region

is excluded when fitting the curvature profile in order to avoid edge effects, while from the rest of values the weighted mean and its standard error are calculated. The substrate surface bending is measured in two perpendicular directions, along ⟨110⟩ directions, of a square $10 \times 10\,\mathrm{mm}^2$ sample and two slightly different $\mathcal{R}$ are obtained per sample. Those are averaged and the following error is estimated

$$\Delta\mathcal{R} = \sqrt{(\Delta\mathcal{R}_1)^2 + (\Delta\mathcal{R}_2)^2}\,. \tag{2.10}$$

Also, it should be noted that it is impossible to scan the surface of a sample in the same line before and after the deposition, thus an additional random error should be included. Finally, the stress in the film is estimated with the following absolute error

$$\Delta\sigma = \sqrt{\left(\frac{\partial\sigma}{\partial\mathcal{R}_\mathrm{a}}\Delta\mathcal{R}_\mathrm{a}\right)^2 + \left(\frac{\partial\sigma}{\partial\mathcal{R}_\mathrm{b}}\Delta\mathcal{R}_\mathrm{b}\right)^2 + \left(\frac{\partial\sigma}{\partial h_\mathrm{f}}\Delta h_\mathrm{f}\right)^2 + \left(\frac{\partial\sigma}{\partial h_\mathrm{s}}\Delta h_\mathrm{s}\right)^2}\,, \tag{2.11}$$

which upon finding and inserting the partial differentials of Eq. (2.1) reduces to

$$\frac{\Delta\sigma}{\sigma} = \sqrt{\left[\frac{\Delta\mathcal{R}_\mathrm{a}\mathcal{R}_\mathrm{b}}{\mathcal{R}_\mathrm{a}\left(\mathcal{R}_\mathrm{b} - \mathcal{R}_\mathrm{a}\right)}\right]^2 + \left[\frac{\Delta\mathcal{R}_\mathrm{b}\mathcal{R}_\mathrm{a}}{\mathcal{R}_\mathrm{b}\left(\mathcal{R}_\mathrm{b} - \mathcal{R}_\mathrm{a}\right)}\right]^2 + \Delta h_\mathrm{f}^2 + 4\Delta h_\mathrm{s}^2}\,. \tag{2.12}$$

2.2.3 Etch-back experiment

To find out whether a stress gradient is present in AlN films, a 1500 nm thick sample from the $\mathcal{S}_{100\%}$ series deposited on Si (Sec. 2.1, Tab. 2.1), was etched in steps for the evaluation of the in-plane stress at lower film thickness. The wet chemical etching was done in a piranha solution. Sulfuric acid (H_2SO_4, 95%) and hydrogen peroxide (H_2O_2, 30%) were mixed in equal ratio by volume and heated to 100°C. After each etching step the substrate curvature and the film thickness were measured and the in-plane stress was calcuated.

2.3 UV-VIS-IR spectroscopy

Optical investigation of thin films is not always straight forward. In order to interpret the reflectance or transmittance of thin films, the electromagnetic (EM) theory of light should be used to derive expressions for the complex-amplitude reflection and transmission coefficients of the film interfaces, in terms of the macroscopic optical properties that characterize the thin film. Depending on the situation the thickness, absorption, refractive index and anisotropy of the thin film, angle of incidence and wavelength of the light as well as the roughness of the present interfaces are the key factors that determine the observed spectra. In this Section, the influence of these quantities on the transmission and reflection spectra will be analyzed.

2.3.1 Fundamental concepts

Light is an EM wave (Fig.2.5) that requires four basic field vectors for their description: the electric-field strength $\vec{E}$, the electric-displacement density $\vec{D}$, the magnetic-field strength $\vec{H}$ and the magnetic-flux density $\vec{B}$. These field vectors are interrelated by Maxwell's field equations and the associated constitutive relations.[3] In general, once one of the fields is determined, e.g. $\vec{E}$, the other remaining field vectors can be found. Thus we will focus on the electric field vector $\vec{E}$ to describe the light waves and their interaction with the thin film of interest.

Maxwell's equations lead to $\vec{E}$ and $\vec{H}$ satisfying the wave equation for which the solutions are linear combinations of plane waves traveling at the speed of light c_0:

$$c_0 = \frac{1}{\sqrt{\epsilon_0 \mu_0}}\,, \tag{2.13}$$

with ϵ_0 and μ_0 the permittivity and permeability of free space, respectively. The electric field observed at a fixed point in space $\vec{r}$ varies with time t as

$$\vec{E}(\vec{r},t) = E_0 \mathrm{e}^{i\left(\vec{r}\cdot\vec{k}-\omega t+\beta\right)}\,, \tag{2.14}$$

with E_0 the electric field amplitude, $\vec{k}$ the angular wavenumber, ω the oscillation angular frequency and β the phase shift. The propagation of light in a medium is governed by the complex index of refraction $\widetilde{N}$ which is expressed as

$$\widetilde{N} = n - i\kappa\,, \tag{2.15}$$

[3] The constitutive relations specify the relations between $\vec{E}$ and $\vec{D}$, and between $\vec{H}$ and $\vec{B}$.

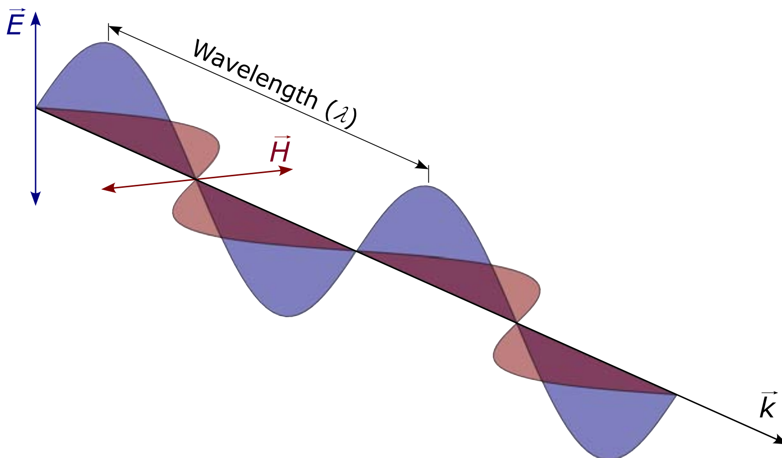

Figure 2.5: Linearly polarized electromagnetic plane wave.

with n the index of refraction and κ the extinction coefficient of the medium. The index of refraction gives a ratio of c_0 relative to the phase velocity in the considered medium v. The extinction coefficient is linked with the absorption coefficient α of the medium as

$$\alpha = \frac{4\pi\kappa}{\lambda} = \frac{2\kappa\omega}{v}\,, \tag{2.16}$$

with λ the wavelength of the EM wave. The complex index of refraction can be written as

$$\widetilde{N} = \sqrt{\widetilde{\epsilon}_{\mathrm{r}}\widetilde{\mu}_{\mathrm{r}}}\,, \tag{2.17}$$

where $\widetilde{\epsilon}_{\mathrm{r}}$ and $\widetilde{\mu}_{\mathrm{r}}$ are complex relative permittivity and permeability of medium, respectively. For most materials $\widetilde{\mu}_{\mathrm{r}} \approx 1$, whereas $\widetilde{\epsilon}_{\mathrm{r}}$ is in general frequency-dependent. Therefore, we write

$$\widetilde{N}(\omega) = n(\omega) - i\kappa(\omega) \approx \sqrt{\widetilde{\epsilon}_{\mathrm{r}}(\omega)}\,. \tag{2.18}$$

Finally, the electric field of the light wave in a medium will be given by

$$\vec{E}(\vec{r},t) = E_0 \mathrm{e}^{i\left(\vec{r}\cdot\vec{k}\widetilde{N} - \omega t + \beta\right)}\,. \tag{2.19}$$

2.3.2 Light reflection and refraction at the interface

Part of the traveling optical plane wave is reflected and part of it is transmitted (refracted) at the planar interface between two media (Fig. 2.6). Here we assume an abrupt change in the refractive index across the interface and assign $\widetilde{N}_0$ and $\widetilde{N}_1$ to the media. The total fields inside the media obey Maxwell's equations and the boundary conditions at the interface. For the boundary conditions to be satisfied: (1) the direction of propagation of the incident, transmitted and reflected light must lie in plane of incidence, which is perpendicular to the interface, (2) the angles of incidence and reflection must be equal, and (3) the angles of incidence ϕ_0 and refraction ϕ_1 must be related by

$$\widetilde{N}_0 \sin\phi_0 = \widetilde{N}_1 \sin\phi_1\,, \tag{2.20}$$

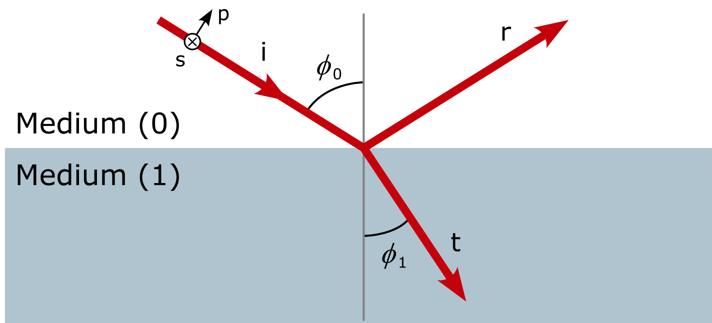

Figure 2.6: Oblique reflection (r) and transmission (t) of incident (i) light at the interface between two media. ϕ_0 and ϕ_1 are the angles of incidence and refraction, respectively.

which is known as Snell's law. In order to find ratios between incident (i) and reflected (r) or transmitted (t) electric fields one needs to match the tangential $\vec{E}$ and $\vec{H}$ fields across the interface. This leads to the following Fresnel complex-amplitude reflection (r) and transmission (t) coefficients for the parallel (p) and perpendicular (s) polarizations (with respect to the plane of incidence) [68]

$$\frac{E_{\mathrm{rp}}}{E_{\mathrm{ip}}} = r_{\mathrm{p}} = \frac{\tilde{N}_1 \cos\phi_0 - \tilde{N}_0 \cos\phi_1}{\tilde{N}_1 \cos\phi_0 + \tilde{N}_0 \cos\phi_1}\,, \tag{2.21}$$

$$\frac{E_{\mathrm{rs}}}{E_{\mathrm{is}}} = r_{\mathrm{s}} = \frac{\tilde{N}_0 \cos\phi_0 - \tilde{N}_1 \cos\phi_1}{\tilde{N}_0 \cos\phi_0 + \tilde{N}_1 \cos\phi_1}\,, \tag{2.22}$$

$$\frac{E_{\mathrm{tp}}}{E_{\mathrm{ip}}} = t_{\mathrm{p}} = \frac{2\tilde{N}_0 \cos\phi_0}{\tilde{N}_1 \cos\phi_0 + \tilde{N}_0 \cos\phi_1}\,, \tag{2.23}$$

$$\frac{E_{\mathrm{ts}}}{E_{\mathrm{is}}} = t_{\mathrm{s}} = \frac{2\tilde{N}_0 \cos\phi_0}{\tilde{N}_0 \cos\phi_0 + \tilde{N}_1 \cos\phi_1}\,. \tag{2.24}$$

Usually in experiments the angle of incidence and the refractive index of media (0 and 1) are known parameters, therefore it is useful to express the Fresnel coefficients using Snell's law and to get rid of the refraction angle ϕ_1

$$r_{\mathrm{p}} = \frac{\tilde{N}_1^2 \cos\phi_0 - \tilde{N}_0\sqrt{\tilde{N}_1^2 - \tilde{N}_0^2 \sin^2\phi_0}}{\tilde{N}_1^2 \cos\phi_0 + \tilde{N}_0\sqrt{\tilde{N}_1^2 - \tilde{N}_0^2 \sin^2\phi_0}}\,, \tag{2.25}$$

$$r_{\mathrm{s}} = \frac{\tilde{N}_0 \cos\phi_0 - \sqrt{\tilde{N}_1^2 - \tilde{N}_0^2 \sin^2\phi_0}}{\tilde{N}_0 \cos\phi_0 + \sqrt{\tilde{N}_1^2 - \tilde{N}_0^2 \sin^2\phi_0}}\,, \tag{2.26}$$

$$t_{\mathrm{p}} = \frac{2\tilde{N}_0\tilde{N}_1 \cos\phi_0}{\tilde{N}_1^2 \cos\phi_0 + \tilde{N}_0\sqrt{\tilde{N}_1^2 - \tilde{N}_0^2 \sin^2\phi_0}}\,, \tag{2.27}$$

$$t_{\mathrm{s}} = \frac{2\tilde{N}_0 \cos\phi_0}{\tilde{N}_0 \cos\phi_0 + \sqrt{\tilde{N}_1^2 - \tilde{N}_0^2 \sin^2\phi_0}}\,. \tag{2.28}$$

The Fresnel coefficients versus incident angle for the AlN/air interface are plotted in Figure 2.7 (a).

In the experiment the photometrically measurable entity of light is radiant flux or radiant power Φ, i.e. the total power of monochromatic EM radiation, that is absorbed by the Si photodiode and converted into electrical current. The fraction $\mathbb{R}_{(\mathrm{p,s})}$ of the total radiant flux of an incident EM plane wave, Φ_{i}, that appears in the wave reflected

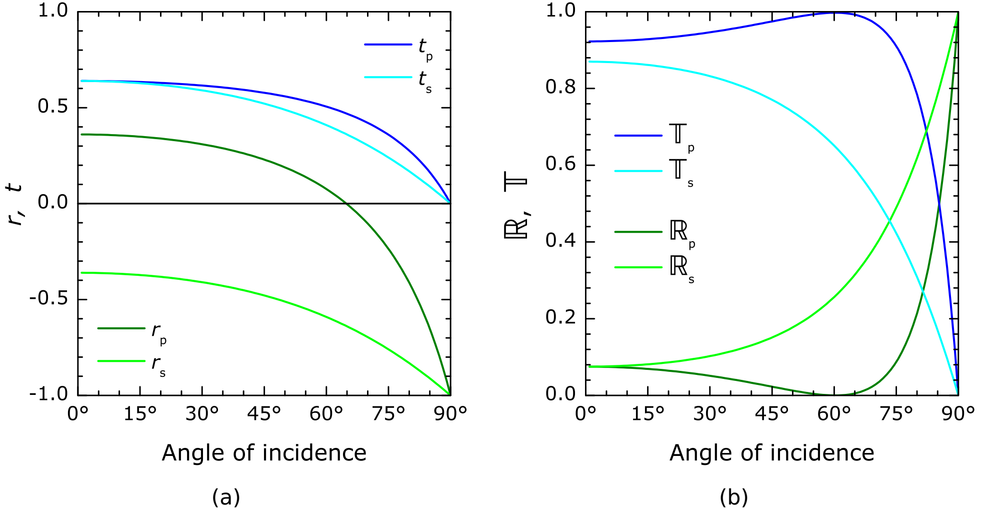

Figure 2.7: (a) Calculated Fresnel amplitude reflection ($r_{(p,s)}$) and transmission ($t_{(p,s)}$) coefficients for the AlN/air interface ($n_{air} = 1$, $n_{AlN} = 2.1$). (b) Photometrically measurable reflectance $\mathbb{R}_{(p,s)}$ and transmittance $\mathbb{T}_{(p,s)}$ of the AlN/air interface.

from the interface of two media, Φ_r, is given by (Fig. 2.7 (b))

$$\frac{\Phi_r}{\Phi_i} = \mathbb{R}_{(p,s)} = \left| r_{(p,s)}\, r^*_{(p,s)} \right| \tag{2.29}$$

and the fraction $\mathbb{T}_{(p,s)}$ in the wave transmitted through the interface, Φ_t, is given by

$$\frac{\Phi_t}{\Phi_i} = \mathbb{T}_{(p,s)} = \frac{\widetilde{N}_1 \cos\phi_1}{\widetilde{N}_0 \cos\phi_0} \left| t_{(p,s)}\, t^*_{(p,s)} \right| , \tag{2.30}$$

here the asterisk ($*$) denotes the complex conjugate. The prefactor $\widetilde{N}_1/\widetilde{N}_0$ of $t_{(p,s)}$ occurs from the ratio of irradiance in two media, as the irradiance I, i.e. power per unit area, of a monochromatic EM wave in medium is given by

$$I \approx \frac{c_0 \widetilde{N} \varepsilon_0}{2} \left| E_0 E_0^* \right| . \tag{2.31}$$

The factor $\cos\phi_1/\cos\phi_0$ (in Eq. 2.30), due to the change in the cross-section of a finite beam upon refraction, needed since the ratio of radiant flux is equal to the irradiance times area [69].

2.3.3 Transmission and reflection in thin films

In case of a thin film on a substrate (Fig. 2.8) one has two interfaces, i.e. ambient-film (0-1) and film-substrate (1-2). Here the interference phenomena in thin film appears. When incident light meets the ambient-film interface a part of it reflects back to the ambient (r_{01}) and the other part transmits into the film (t_{01}). The refracted light experiences multiple reflections inside the thin film as each time at the interface it is partly reflected (r_{12} and r_{10}) and transmitted (t_{12} and t_{10}). These transmissions and reflections are described by Fresnel complex-amplitude coefficients (Eqs. 2.25–2.28). While crossing the film, light will experience the a phase shift, i.e. the fraction of the wave cycle which is elapsed relative to the reflected wave, [4]

$$\beta = 2\pi \left(\frac{h_\mathrm{f}}{\lambda} \right) \tilde{N}_1 \cos\phi_1 \,, \tag{2.32}$$

or if Snell's law is applied

$$\beta = 2\pi \left(\frac{h_\mathrm{f}}{\lambda} \right) \sqrt{\tilde{N}_1^2 - \tilde{N}_0^2 \sin^2\phi_0} \,. \tag{2.33}$$

When each part of the beam is added (Fig. 2.8) to calculate the resultant reflected wave one gets

$$R = r_{01} + t_{01}\, t_{10}\, r_{12}\, \mathrm{e}^{-i2\beta} + t_{01}\, t_{10}\, r_{10}\, r_{12}^2\, \mathrm{e}^{-i4\beta} + t_{01}\, t_{10}\, r_{10}^2\, r_{12}^3\, \mathrm{e}^{-i6\beta} + \cdots \,, \tag{2.34}$$

[4] In the following equations the indices of appropriate polarization p or s are not mentioned for simplicity. When the total transmission or reflection of p- or s-polarizations are calculated the corresponding Fresnel coefficients of p- or s-polarization are used.

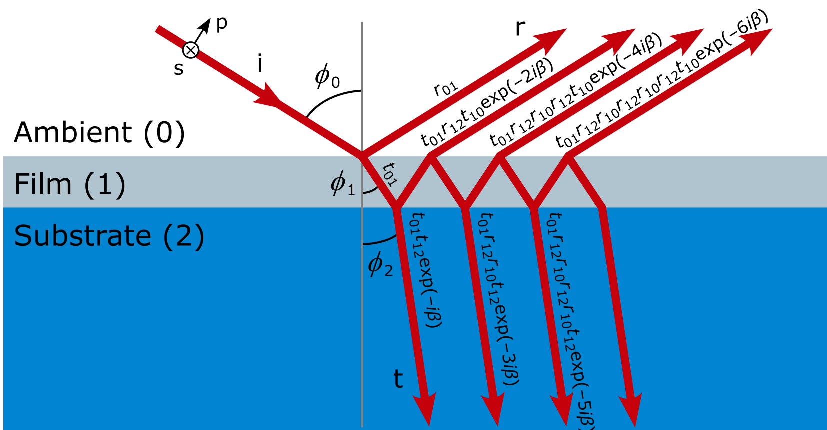

Figure 2.8: Oblique reflection and transmission of light by an ambient (0) – film (1) – substrate (2) system. ϕ_0, ϕ_1 and ϕ_2 are the angles of incidence, refraction in the film and refraction in the substrate, respectively.

here indices denote the EM wave propagation direction, for r 01 means the reflection in ambient (0) from ambient-film interface and for t 01 means transmission from the ambient (0) to the film (1). Thus in general the Fresnel complex-amplitude coefficients (Eqs. (2.25)–(2.28)) are different depending on the direction. With substitutions[5] $r_{10} = -r_{01}$ and $t_{01}\, t_{10} = 1 - r_{01}^2$ the Eq. (2.34) can be expressed as

$$R = \frac{r_{01} + r_{12}\, \mathrm{e}^{-i2\beta}}{1 + r_{01}\, r_{12}\, \mathrm{e}^{-i2\beta}} \,. \tag{2.35}$$

In the same way the total transmitted complex-amplitude of the EM wave is calculated

$$T = t_{01}\, t_{12}\, \mathrm{e}^{-i\beta} + t_{01}\, t_{12}\, r_{10}\, r_{12}\, \mathrm{e}^{-i3\beta} + t_{01}\, t_{12}\, r_{10}^2\, r_{12}^2\, \mathrm{e}^{-i5\beta} + \cdots \,, \tag{2.36}$$

which can be expressed as

$$T = \frac{t_{01}\, t_{12}\, \mathrm{e}^{-i\beta}}{1 + r_{01}\, r_{12}\, \mathrm{e}^{-i2\beta}} \,. \tag{2.37}$$

Finally, to calculate the photometrically measurable quantities the Eqs. (2.29) and (2.30) are used by replacing r and t with R and T, respectively.

2.3.4 Uniaxially anisotropic film

AlN is an uniaxial material that has one crystal axis, i.e. c-axis, that is different from the other two crystal axes, i.e. a-axis and b-axis which are identical (Fig. 1.1). This unique axis is referred to as the optic axis. The index of refraction along the optic

[5] This can be shown when the complex index of refraction, $\tilde{N}_0$ and $\tilde{N}_1$, are swapped in Eqs. (2.25)–(2.28).

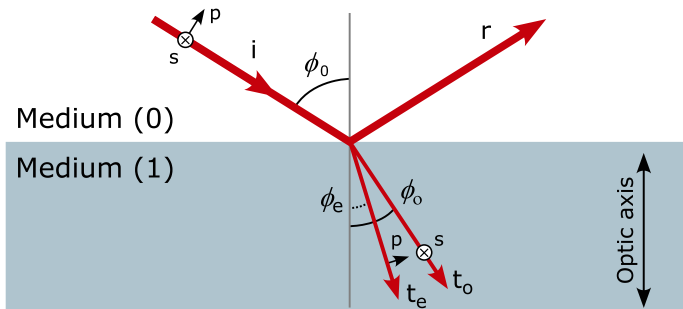

Figure 2.9: Oblique reflection (r) and transmission for ordinary (t_o) and extraordinary (t_e) rays of incident (i) light at the interface between isotropic medium (1) and anisotropic medium (2) with an optic axis parallel to the surface normal. ϕ_0 is angle of incidence, ϕ_o and ϕ_e are the angles of refraction for ordinary and extraordinary rays, respectively.

axis is called the extraordinary one, $\widetilde{N}_{1e}$, whereas the complex index of refraction in the other two directions is the ordinary one, $\widetilde{N}_{1o}$.

A special case of interest is that in which the optic axis of the uniaxial film is perpendicular to its boundaries with the ambient and substrate (Fig. 2.9), e.g. the optic axis of AlN, i.e. the *c*-axis, is parallel to the surfaces normal of AlN film and substrate. In this case, relatively simple expressions of the Fresnel reflectance r and transmittance t coefficients are obtained for each interface for p- and s-polarization of the light [70]:

$$r_{01p} = \frac{\widetilde{N}_{1o}\widetilde{N}_{1e}\cos\phi_0 - \widetilde{N}_0\sqrt{\widetilde{N}_{1e}^2 - \widetilde{N}_0^2\sin^2\phi_0}}{\widetilde{N}_{1o}\widetilde{N}_{1e}\cos\phi_0 + \widetilde{N}_0\sqrt{\widetilde{N}_{1e}^2 - \widetilde{N}_0^2\sin^2\phi_0}}\,, \tag{2.38}$$

$$r_{12p} = \frac{-\widetilde{N}_{1o}\widetilde{N}_{1e}\cos\phi_2 + \widetilde{N}_2\sqrt{\widetilde{N}_{1e}^2 - \widetilde{N}_2^2\sin^2\phi_2}}{\widetilde{N}_{1o}\widetilde{N}_{1e}\cos\phi_2 + \widetilde{N}_2\sqrt{\widetilde{N}_{1e}^2 - \widetilde{N}_2^2\sin^2\phi_2}}\,, \tag{2.39}$$

$$r_{01s} = \frac{\widetilde{N}_0\cos\phi_0 - \sqrt{\widetilde{N}_{1o}^2 - \widetilde{N}_0^2\sin^2\phi_0}}{\widetilde{N}_0\cos\phi_0 + \sqrt{\widetilde{N}_{1o}^2 - \widetilde{N}_0^2\sin^2\phi_0}}\,, \tag{2.40}$$

$$r_{12s} = \frac{-\widetilde{N}_2\cos\phi_2 + \sqrt{\widetilde{N}_{1o}^2 - \widetilde{N}_2^2\sin^2\phi_0}}{\widetilde{N}_2\cos\phi_2 + \sqrt{\widetilde{N}_{1o}^2 - \widetilde{N}_2^2\sin^2\phi_0}}\,, \tag{2.41}$$

$$t_{01p} = \frac{2\widetilde{N}_0\cos\phi_0}{\widetilde{N}_{1o}\widetilde{N}_{1e}\cos\phi_0 + \widetilde{N}_0\sqrt{\widetilde{N}_{1e}^2 - \widetilde{N}_0^2\sin^2\phi_0}}\,, \tag{2.42}$$

$$t_{12p} = \frac{2\widetilde{N}_{1o}\widetilde{N}_{1e}\sqrt{\widetilde{N}_{1e}^2 - \widetilde{N}_0^2\sin^2\phi_0}}{\widetilde{N}_{1o}\widetilde{N}_{1e}\cos\phi_0 + \widetilde{N}_0\sqrt{\widetilde{N}_{1e}^2 - \widetilde{N}_0^2\sin^2\phi_0}}\,, \tag{2.43}$$

$$t_{01s} = \frac{2\widetilde{N}_0\cos\phi_0}{\widetilde{N}_0\cos\phi_0 + \sqrt{\widetilde{N}_{1o}^2 - \widetilde{N}_0^2\sin^2\phi_0}}\,, \tag{2.44}$$

$$t_{12s} = \frac{2\sqrt{\widetilde{N}_{1o}^2 - \widetilde{N}_0^2\sin^2\phi_0}}{\widetilde{N}_0\cos\phi_0 + \sqrt{\widetilde{N}_{1o}^2 - \widetilde{N}_0^2\sin^2\phi_0}}\,. \tag{2.45}$$

Due to anisotropy, the phase shift β differs for p- and s-polarizations

$$\beta_p = 2\pi\frac{d}{\lambda}\frac{\widetilde{N}_{1o}}{\widetilde{N}_{1e}}\sqrt{N_{1e}^2 - N_0^2\sin^2\phi_0} \tag{2.46}$$

and

$$\beta_s = 2\pi\frac{d}{\lambda}\sqrt{\widetilde{N}_{1o}^2 - N_0^2\sin^2\phi_0}\,. \tag{2.47}$$

Finally, the total complex-amplitude of reflection and transmission is calculated ac-

cording to Eqs. (2.35) and (2.37), respectively, where for each polarization the corresponding Fresnel coefficients and phase shift values are inserted. Then the measurable quantity is calculated according to Eqs. (2.29) and (2.30).

2.3.5 Influence of surface roughness

In case of a rough surface, e.g. polycrystalline CVD diamond films, light is scattered while crossing the interface and in turn the reflection and transmission are hampered. Consequently, the phenomenon of interference in thin films is altered. The Fresnel coefficients of a rough interface are reduced by surface scattering factors [71]

$$S_{\mathrm{r}(0,1)} = \mathrm{e}^{-8\left(\frac{\pi \tilde{N}_{(0,1)}\,\rho}{\lambda}\right)^2}\,, \tag{2.48}$$

$$S_{\mathrm{t}} = \mathrm{e}^{-8\left[\frac{\pi\left(\tilde{N}_0 - \tilde{N}_1\right)\rho}{\lambda}\right]^2}\,, \tag{2.49}$$

where subscripts r and t denote the scattering factors that are used in combination with the Fresnel complex-amplitude reflection and transmission coefficients, respectively, indices 0 and 1 indicate in which media the reflection takes place, ρ is the surface roughness. Then for a thin film-substrate system, with the assumption that the film-substrate interface is smooth, the total reflection complex-amplitude is

$$R = \frac{S_{\mathrm{r0}}\, r_{01} + \left(S_{\mathrm{r0}}\, S_{\mathrm{r1}}\, r_{01}^2 + S_{\mathrm{t}}^2\, t_{01}\, t_{10}\right) r_{12}\, \mathrm{e}^{-i2\beta}}{1 + S_{\mathrm{r1}}\, r_{01}\, r_{12}\, \mathrm{e}^{-i2\beta}} \tag{2.50}$$

and the total transmission complex-amplitude is

$$T = \frac{S_{\mathrm{t}}\, t_{01}\, t_{12}\, \mathrm{e}^{-i\beta}}{1 + S_{\mathrm{r1}}\, r_{01}\, r_{12}\, \mathrm{e}^{-i2\beta}}\,. \tag{2.51}$$

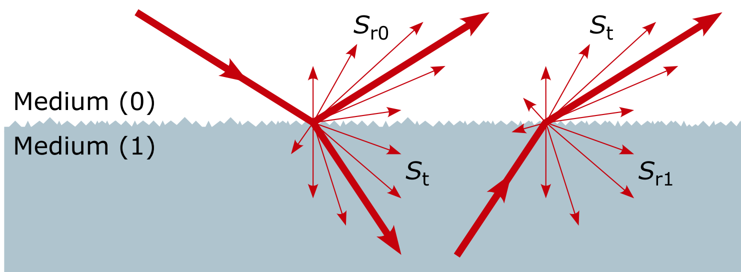

Figure 2.10: Light scattering at the interface of two media. Two different scattering factors are defined when light is: reflected back to the medium it came from (S_{r}) and transmitted through the interface of two media (S_{t}).

2.3.6 Experimental set-ups

Ex-situ measurements

The home-build experimental set-up for transmission and reflection measurements in the UV-VIS-IR range of EM wave spectrum (1 eV – 5 eV)[6] is shown in Figure 2.11. The light flux of a xenon arc lamp is chopped with an optical chopper at 79 Hz. Then light is dispersed with an Oriel Cornerstone^{TM} 260 1/4 m monochromator. A UV-grade fused silica (UV-FS) lens focuses the beam. Part of the beam is reflected from UV-FS beam splitter to the detector for monitoring the light flux that falls onto a sample. The sample is placed on the backside of the integrating sphere. The detector behind the sample is dedicated for transmission measurements, while the detector connected to the integrating sphere is gathering the reflected light. The detectors used for the measurements are Si photodiodes with UV-enhanced responsivity. These photodiodes are operated in photovoltaic (unbiased) mode, during which no external bias is applied. In this case the lowest dark current is achieved.

In order to extract reliable data, the following procedure is done: (i) the xenon lamp spectrum is measured without the sample placed behind the sphere, (ii) a NIST calibrated reflectance sample is placed and it's reflectance is measured, and (iii) the transmission and reflection spectra of a samples are measured.

Case I: no sample. With the so called transmission detector (D_T) the radiant flux that comes from the lamp is measured at each wavelength and is assigned as total flux $\Phi_{T,total}(\lambda)$. At the same time the reflection detector (D_R) measures the background level, $\Phi_{R,backg.}(\lambda)$. The detector's dark current is neglected as it was measured to be at least two orders of magnitude lower than the measured signal and at least one order of magnitude lower than the background signal. The reference

[6] 250 nm – 1250 nm, $\lambda(\text{nm}) \cdot \hbar\omega(\text{eV}) = 2\pi\hbar c$.

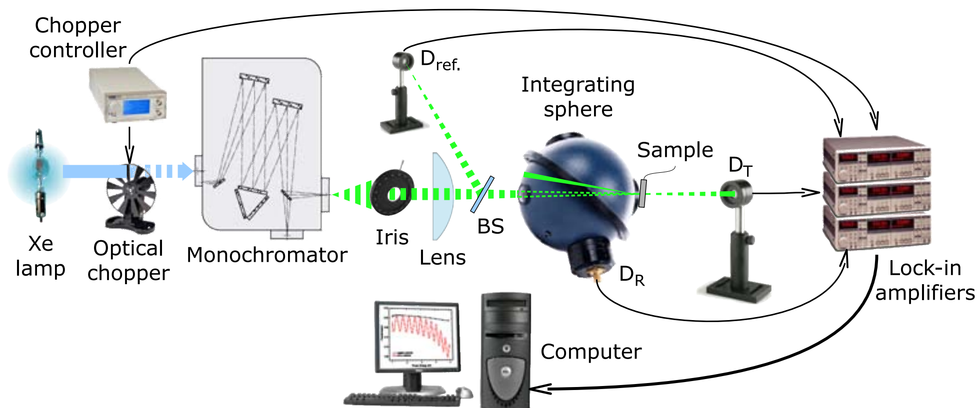

Figure 2.11: Experimental set-up of transmission and reflectance measurements in the UV-VIS-IR range. BS – beam splitter, D – silicon photodiodes: ref. – reference, T – transmission, R – reflection.

detector ($D_{ref.}$) measures the flux of light that reflects from a beam splitter, $\Phi_{ref.,1}(\lambda)$. Then the following ratios are calculated

$$\eta_T(\lambda) = \frac{\Phi_{T,total}(\lambda)}{\Phi_{ref.,1}(\lambda)}, \tag{2.52}$$

$$\eta_{backg.}(\lambda) = \frac{\Phi_{R,backg.}(\lambda)}{\Phi_{ref.,1}(\lambda)}, \tag{2.53}$$

which are used to determine the actual flux that falls onto the sample during the measurement, $\Phi_{T,total}(\lambda) = \Phi_{ref.}(\lambda)\,\eta_T(\lambda)$, and the background light level inside the integrating sphere, $\Phi_{backg.}(\lambda) = \Phi_{ref.}(\lambda)\eta_{backg.}(\lambda)$. This is performed to avoid the lamp's aging and flux fluctuation effects as the mentioned quantities are reconstructed at the same time the measurement is done, i.e. during the measurement the D_T, D_R and $D_{ref.}$ record the signal simultaneously.

Case II: NIST calibrated sample. When the NIST sample is placed the signal that D_R measures

$$\Phi_{R,NIST}(\lambda) = \Phi_{R,total}(\lambda)\,\mathbb{R}_{NIST}(\lambda)\,\Psi(\lambda) + \Phi_{R,backg.}(\lambda), \tag{2.54}$$

where $\Phi_{R,total}(\lambda)$ is the total flux[7], $\mathbb{R}_{NIST}$ is the known reflectivity of the NIST calibrated sample and Ψ is the unknown sphere's throughput efficiency[8]. Then a ratio between the measurement by $D_{ref.}$ with the signal at D_R that would be assigned for total reflectivity is constructed

$$\eta_R(\lambda) = \frac{\Phi_{R,total}(\lambda)}{\Phi_{ref.,2}(\lambda)} = \frac{\Phi_{R,NIST}(\lambda) - \Phi_{R,backg.}(\lambda)}{\Phi_{ref.,2}(\lambda)\,\mathbb{R}_{NIST}(\lambda)\,\Psi(\lambda)}. \tag{2.55}$$

Here $\Phi_{backg.}(\lambda)$ can be replaced by $\Phi_{ref.,2}(\lambda)\,\eta_{backg.}(\lambda)$ or the background data, measured in case I, can be used if measurements are done in one course.

Case III: sample. When a sample is measured the transmission and reflection spectra are calculated as

$$\mathbb{T}_{sample}(\lambda) = \frac{\Phi_{T,sample}(\lambda)}{\Phi_{ref.,3}(\lambda)\,\eta_T(\lambda)}, \tag{2.56}$$

$$\mathbb{R}_{sample}(\lambda) = \frac{\Phi_{R,sample}(\lambda) - \Phi_{backg.}(\lambda)}{\Phi_{ref.,3}(\lambda)\,\eta_R(\lambda)\,\Psi(\lambda)}. \tag{2.57}$$

When in the latter expression $\eta_R(\lambda)$ is inserted one gets rid of $\Psi(\lambda)$

$$\mathbb{R}_{sample}(\lambda) = \frac{\Phi_{ref.,2}(\lambda)\,\mathbb{R}_{NIST}(\lambda)\,\left[\Phi_{R,sample}(\lambda) - \Phi_{backg.}(\lambda)\right]}{\Phi_{ref.,3}(\lambda)\,\left[\Phi_{R,NIST}(\lambda) - \Phi_{R,backg.}(\lambda)\right]}. \tag{2.58}$$

[7] $\Phi_{R,total}(\lambda)$ and $\Phi_{T,total}(\lambda)$ are equal, however the detector is not the same, thus the quantities are treated separately to avoid error due to difference in the responsivity of the detectors.

[8] Due to aging the reflectivity of integrating sphere coating becomes unknown.

If one assumes that $\Phi_{\text{ref.},2}(\lambda) = \Phi_{\text{ref.},3}(\lambda)$ and that $\Phi_{\text{R,backg.}}(\lambda)$ is negligible[9], the latter expression reduces to

$$\mathbb{R}_{\text{sample}}(\lambda) = \frac{\Phi_{\text{R,sample}}(\lambda)}{\Phi_{\text{R,NIST}}(\lambda)} \mathbb{R}_{\text{NIST}}(\lambda) . \tag{2.59}$$

In-situ measurements

The thickness of growing NCD films was monitored in-situ by measuring the laser beam reflection from the film. A diode pumped solid state laser beam ($\lambda = 473$ nm) angled at 28° to the sample, reflected and measured with a Si photodiode. In order to avoid plasma radiation background an interference filter was used. In the measured reflectance signal constructive and destructive interference fringes are appearing with increasing NCD thickness (Fig. 2.12 (a)), allowing the determination of film thickness at these extrema by using Equations (2.29) and (2.50). Furthermore, the growth rate variation with time can be reconstructed. The amplitude of observed interference gives an indication of surface roughness and light scattering inside the film (Fig. 2.12 (b)), that can be accessed by fitting the in-situ curve.

[9] However, this was not the case for the photon energies above 3 eV.

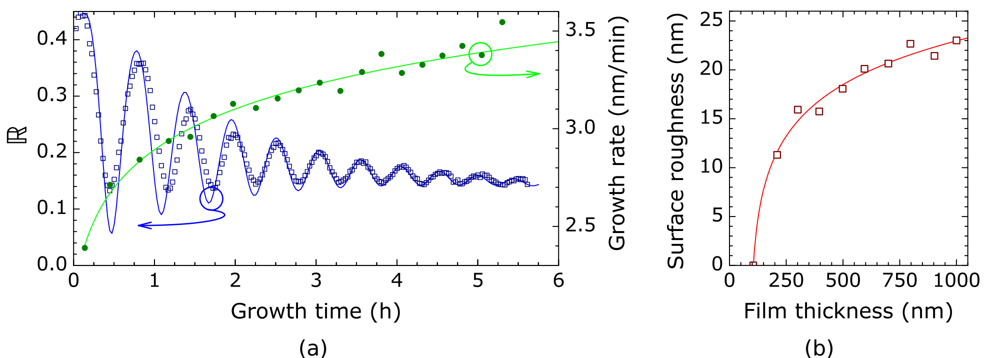

Figure 2.12: (a) In-situ measurement (open squares) and simulation (solid line) of reflection from NCD film. The index of refraction at 473 nm of NCD ($n_{\text{NCD}} = 2.44$) used in calculation is taken from the literature (Ref. [72]). The extinction coefficient ($\kappa_{\text{NCD}} = 0.12$) and surface roughness of NCD was estimated by fitting the measurement data. The full points and dashed line represents growth rate variation with growth time; the line is a guide for the eyes. (b) Calculated surface roughness versus NCD film thickness. The line is a guide for the eyes.

2.4 Film thickness determination

By analyzing the interference fringes in transmission and reflection spectra the film thickness is determined. A typical spectra of 200 nm thick AlN on sapphire substrate is presented in Figure 2.13 (a). In case of AlN on sapphire, a transparent substrate in UV-VIS-IR spectral range, one can analyze transmission spectra of the film as described by Swanepoel [74]. This method gives a recipe how to deal with transmission spectra and gives simplified form of Equations (2.25–2.28, 2.29–2.30) to calculate the refractive index and film thickness at the extrema points of interference fringes. Build on Swanepoel's method the transmission spectra of AlN/Al_2O_3 were analyzed to determine the film thickness and ordinary refractive indexes[10] of AlN (Fig. 2.13 (b), points). However, in case of AlN on silicon substrate, the analysis of the reflectance spectra is only possible. The positions of minima and maxima of interference fringes in reflection spectra were calculated using the refractive index taken from the literature [73]. These did not coincide with the experimentally observed positions. The iterative change of refraction index and the re-calculation of interference fringes positions were done in order to fit the experimental points. In Figure 2.13 (b) the solid line represents the final solution for the index of refraction with which the calculated and experimental positions of interference fringes coincided. In all cases, the obtained refractive indexes were more or less of the same value and slightly lower than for AlN single crystal (Fig. 2.13 (b), dashed line), indicating that the sputtered AlN films are of good quality [7].

[10]The *c*-axis, i.e. the optic axis, was confirmed to be parallel to the surface normal (Fig. 3.4). In this case the electric field of light that propagates along the optic axis is perpendicular to the optic axis, i.e. the ordinary directions.

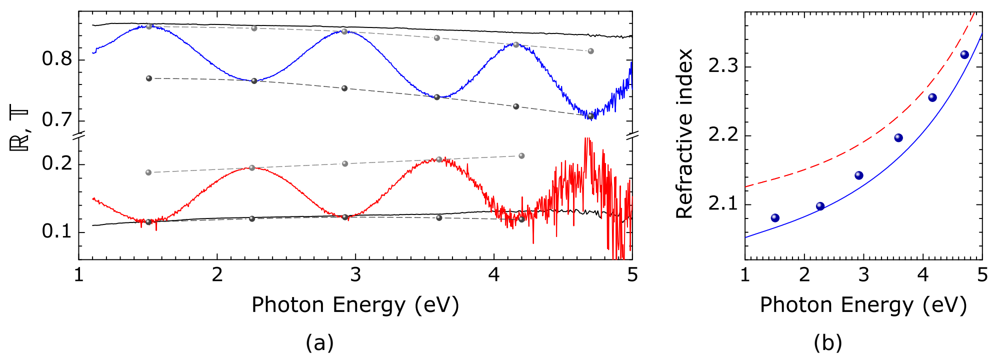

Figure 2.13: (a) Transmission (upper part) and reflection (lower part) spectra of 200 nm thick AlN film on Al_2O_3 substrate (line). The dashed lines represent a bare substrate spectra. (b) Ordinary refractive index of AlN: points – calculated using the Swanepoel's method, solid line – adapted to fit the reflection measurements, and dashed line – taken from Ref. [73].

2.5 Optical phonons in AlN

According to energy and momentum conservation laws only optical phonon modes, transverse optical (TO) and longitudinal optical (LO), can interact with light [42]. That is why they are called optical phonons. For hexagonal close-packed (hcp) crystal structures, e.g. AlN (Fig. 2.14 (a)), there is an additional subdivision of optical phonons based on symmetry [75, 76]. In AlN there are *A*, *B* and *E* symmetries denoted in Mulliken's notation [77]. In the axial *A* (symmetric) and *B* (antisymmetric) phonon modes the atomic displacement occurs along the c-axis, while in *E* (doubly degenerate[11]) mode it occurs perpendicular to the *c*-axis (Fig. 2.14 (b)).

The hexagonal AlN with the wurtzite structure belongs to the C_{6v}^4 ($P6_3mc$) space group. The group theory predicts the symmetries of Γ-point optical-phonon modes to be $A_1 + E_1 + 2E_2 + 2B_1$. The A_1, E_1 and E_2 modes are Raman active, the A_1 and E_1 modes are infrared active, and the B_1 modes are inactive (silent modes) [78]. The A_1 and E_1 modes are polar as there is a long-range electrostatic field in the crystal. The interaction of the vibrations with the long-range Coulomb field leads to an energy difference between the vibration polarized parallel and perpendicular to the direction of propagation of the phonon (LO mode and TO mode, respectively).

2.5.1 Theoretical model of dielectric functions

The best way to understand transmission and reflection spectra in the IR region is to analyze the interaction between photons and optical phonons in a solid. IR active phonons interact directly with IR light. If the atoms are charged then photons can couple to phonons trough the driving force of an alternating electric field of light. EM waves are transverse and can only apply driving forces to the transverse vibrations of the lattice. Therefore, they can only couple to TO phonon modes. In case of a III-V semiconductor, the bond between atoms is partly covalent, and shared electrons lie slightly closer to the group V atoms than to the group III atoms. Thus one has a

[11]There are two orthogonal directions perpendicular to the wurtzite *c*-axis.

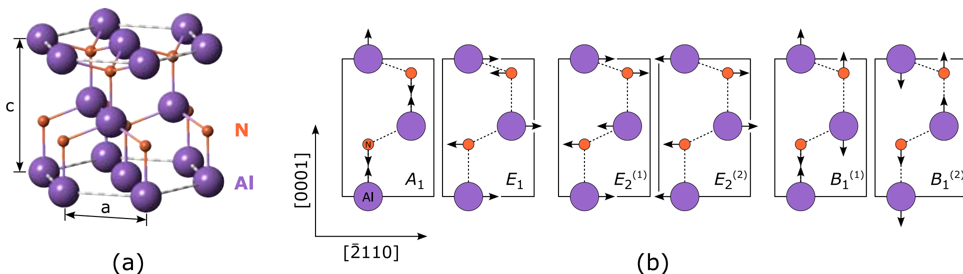

Figure 2.14: (a) Crystal structure of wurtzite AlN. (b) Displacement pattern for the six optical Γ-point phonon modes in the wurtzite AlN. TO phonons propagate perpendicular to the displacement direction, whereas LO phonons propagate along the displacement direction, e.g. the E_1(TO) phonon and the A_1(LO) phonon will propagate along [0001] direction.

partly ionic bond, where an asymmetric electron cloud creates a dipole that can interact with the electric field. The interaction between TO phonon and light can be simulated using a classical Lorentz oscillator model that describes complex relative permittivities as[12] [79–83]

$$\widetilde{\varepsilon}_{(\perp,\parallel)}(\omega) = \varepsilon_{\infty(\perp,\parallel)} + \sum_j \frac{4\,\pi\, F^2_{\mathrm{TO}j(\perp,\parallel)}\,\omega^2_{\mathrm{TO}j(\perp,\parallel)}}{\omega^2_{\mathrm{TO}j(\perp,\parallel)} - \omega^2 - i\omega\Gamma_{\mathrm{TO}j(\perp,\parallel)}}\,. \tag{2.60}$$

Here the indices $\perp$ and $\parallel$ are related to the E_1 and A_1 symmetry, respectively, of TO phonons, j denotes the phonon mode index, $\varepsilon_{\infty(\perp,\parallel)}$ is the high-frequency limit of the complex permittivity, F is the oscillator strength, $\omega_{\mathrm{TO}(\perp,\parallel)}$ is the resonant frequency of the TO phonon and $\Gamma_{\mathrm{TO}(\perp,\parallel)}$ is the damping constant. In view the of latter expression, a resonant excitation of TO phonons by EM light waves causes a large dielectric displacement $\vec{D}$, and corresponds to the poles[13] of the dielectric function.

The electric-displacement density $\vec{D}$ is related to $\vec{E}$ and polarization $\vec{P}$ through

$$\vec{D} = \varepsilon_0\vec{E} + \vec{P} = \varepsilon_0\widetilde{\varepsilon}\vec{E}\,, \tag{2.61}$$

where $\vec{P} = \varepsilon_0\chi\vec{E}$, with $\chi = 1+\widetilde{\varepsilon}$ the electric susceptibility. In a medium with no electric charge, according to the Gauss law [84]

$$\nabla\vec{D} = \nabla\cdot\left(\widetilde{\varepsilon}\varepsilon_0\vec{E}\right) = 0\,. \tag{2.62}$$

When considering the propagation of EM waves through the medium, the solution of the wave equation (Eq. (2.19)) is substituted into the Equation (2.62) with the usual assumption that $\widetilde{\varepsilon} \neq 0$. By solving it one gets that the solution is $\vec{k}\cdot\vec{E} = 0$, i.e. that the electric field must be perpendicular to the propagation direction (transverse EM waves). However, if $\widetilde{\varepsilon} = 0$, one can satisfy the Equation (2.62) with waves in which $\vec{k}\cdot\vec{E} \neq 0$, i.e. with longitudinal EM waves. Therefore, the propagation of polar LO phonon modes requires zero divergence of the dielectric displacement ($\nabla\vec{D} = 0$), and therefore zeros in the complex permittivity and thus the poles of

$$\widetilde{\varepsilon}^{-1}_{(\perp,\parallel)}(\omega) = \varepsilon^{-1}_{\infty(\perp,\parallel)} + \sum_j \frac{4\,\pi\, F_{\mathrm{LO}j(\perp,\parallel)}\,\omega^2_{\mathrm{LO}j(\perp,\parallel)}}{\omega^2_{\mathrm{LO}j(\perp,\parallel)} - \omega^2 - i\omega\Gamma_{\mathrm{LO}j(\perp,\parallel)}}\,. \tag{2.63}$$

As a result the complex permittivity may be written in the alternative form as the factorized damped oscillator

$$\widetilde{\varepsilon}_{(\perp,\parallel)}(\omega) = \varepsilon_{\infty(\perp,\parallel)} \prod_j \frac{\omega^2_{\mathrm{LO}j(\perp,\parallel)} - \omega^2 - i\omega\Gamma_{\mathrm{LO}j(\perp,\parallel)}}{\omega^2_{\mathrm{TO}j(\perp,\parallel)} - \omega^2 - i\omega\Gamma_{\mathrm{TO}j(\perp,\parallel)}}\,. \tag{2.64}$$

[12] In the following equations the subscript r for 'relative' are dropped for simplicity.
[13] For a pole of $f(x)$ at point a the function approaches infinity as x approaches a.

The high-frequency limit of the complex permittivity, $\varepsilon_{\infty,\perp} = 3.93$ and $\varepsilon_{\infty,\parallel} = 4.05$, were deduced by Kazan *et al.* in AlN single crystals [50]. The phonon frequencies $\omega_{TO(\perp,\parallel)}$ and $\omega_{LO(\perp,\parallel)}$ together with the damping constants $\Gamma_{TO(\perp,\parallel)}$ and $\Gamma_{LO(\perp,\parallel)}$ are the fitting parameters in the model.

As AlN is an uniaxial anisotropic material, the complex permittivity tensor has the diagonal form

$$\tilde{\varepsilon} = \begin{pmatrix} \tilde{\varepsilon}_\perp & 0 & 0 \\ 0 & \tilde{\varepsilon}_\perp & 0 \\ 0 & 0 & \tilde{\varepsilon}_\parallel \end{pmatrix} .$$

In these dielectric functions lies the core of the modeled FTIR spectra, because they are used to construct the ordinary ($\tilde{\varepsilon}_\perp$) and the extraordinary ($\tilde{\varepsilon}_\parallel$) complex index of refraction (Eq. (2.18)). The second milestone is the formation of Fresnel coefficients (Eqs. 2.38–2.45). Then the total complex-amplitude transmission of unpolarized light $T_u = (T_s + T_p)/2$ is calculated considering the multiple reflections at the interfaces and light interference in the film (Eq. (2.37)) and the measured transmission is calculated according to Equation (2.30).

In Figure 2.15 the step-by-step simulation results of FTIR spectra are presented. Here the optic axis of the film is considered to be parallel to the surface normal (Sec. 2.3.4). The permittivity describes the response of a material to an electrical field and it depends on the angular frequency of the field. The absorption of electric field is incorporated through the imaginary part of the permittivity ($\Im(\tilde{\varepsilon})$, Fig. 2.15 (b)), whereas the real part ($\Re(\tilde{\varepsilon})$, Fig. 2.15 (a)) is related to the stored energy within the medium. For an ideal oscillator, i.e. without damping (the dash-dotted lines), there would be poles of the permittivity function at the TO phonon frequencies. Due to the presence of damping (the solid lines) the $\Re(\tilde{\varepsilon})$ reaches maximum at $\omega_{TO(\perp,\parallel)} - \Gamma_{TO(\perp,\parallel)}/2$. Then $\Re(\tilde{\varepsilon})$ falls sharply crossing zero at $\omega_{TO(\perp,\parallel)}$, reaches minimum at $\omega_{TO(\perp,\parallel)} + \Gamma_{TO(\perp,\parallel)}/2$ and rises to the high frequency limit ε_∞ while crossing zero again at $\omega_{LO(\perp,\parallel)}$. Meanwhile, the $\Im(\tilde{\varepsilon})$ shows a peak function with maximum at $\omega_{TO(\perp,\parallel)}$ and full width at half maximum $\Gamma_{TO(\perp,\parallel)}$. One should note that there is no peak in $\Im(\tilde{\varepsilon})$ associated with the LO phonon modes. From the complex permittivity function the complex index of refraction is calculated (Eq. (2.18), Fig. 2.15 (c,d)). In the ideal case $\Gamma = 0$, the complex index of refraction has only the imaginary part ($n = 0$, $\kappa > 0$) between $\omega_{TO(\perp,\parallel)}$ and $\omega_{LO(\perp,\parallel)}$. When $\kappa > 0$, the medium is absorbing the EM waves (Eq. (2.16)).

To analyze the phase shift of the EM wave in a 200 nm thick film (Fig. 2.15 (e,f)) one has to insert Equation (2.15) into Equation (2.32)[14]. This leads to the following form of the phase shift

$$\beta = 2\pi \left(\frac{h_f}{\lambda}\right)(n_1 - i\kappa_1)\cos\phi_1 . \tag{2.65}$$

Then the exponent, in Equations (2.35) and (2.37), becomes

$$e^{-i\beta} = \underbrace{e^{-i2\pi(h_f/\lambda)n_1\cos\phi_1}}_{\text{phase shift}} + \underbrace{e^{-2\pi(h_f/\lambda)\kappa_1\cos\phi_1}}_{\text{absorption}} = e^{-i\Re(\beta)} + e^{-\Im(\beta)} . \tag{2.66}$$

[14] This equation was chosen for simplicity.

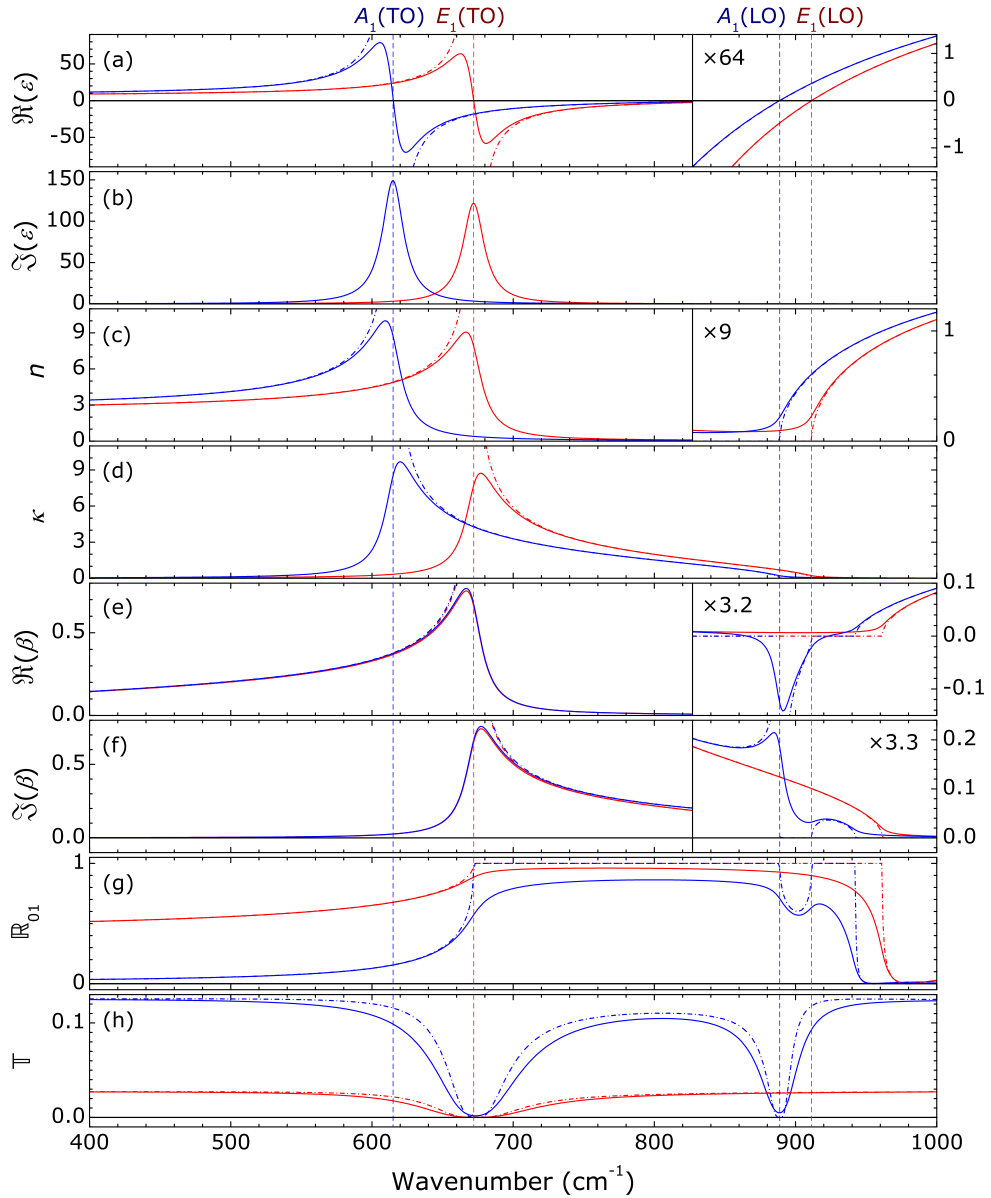

Figure 2.15: Step-by-step results of FTIR spectra simulation: the real (a) and imaginary (b) part of permittivity (Eq. (2.64)), the index of refraction (c) and extinction coefficient (d) (Eq. (2.18)), the real (e) and imaginary (f) part of phase shift (Eqs. (2.46) and (2.47)), the reflectance of the air/AlN (bulk) interface (g) (Eq. (2.29)) and the transmission through the AlN(200 nm)/Si system (Eq. (2.30)). The red curves are attributed to $\tilde{\varepsilon}_{\perp}$, $\tilde{N}_{1\mathrm{o}}$, β_{s}, $\mathbb{R}_{\mathrm{s}}$ and $\mathbb{T}_{\mathrm{s}}$. The blue curves are attributed to $\tilde{\varepsilon}_{\parallel}$, $\tilde{N}_{1\mathrm{e}}$, β_{p}, $\mathbb{R}_{\mathrm{p}}$ and $\mathbb{T}_{\mathrm{p}}$. The vertical dashed lines indicate the phonon frequencies used in the model, other parameters used in the simulation: $\Gamma_{\mathrm{TO},(\perp,\parallel)} = 18.2\ \mathrm{cm}^{-1}$, $\Gamma_{\mathrm{LO},(\perp,\parallel)} = 10.7\ \mathrm{cm}^{-1}$, $h_{\mathrm{f}} = 200$ nm, $\phi_0 = 60°$ and $n_{\mathrm{Si}} = 3.42$. The dash-dotted curves are attributed for the ideal oscillator, $\Gamma_{\mathrm{TO,LO}(\perp,\parallel)} = 0$. The optic axis parallel to the surface normal is considered.

Here two separate parts appear: (i) the exponent which governs the phase shift and (ii) the exponent which corresponds to the absorption. The shift in the phase determines the amplitude of two superimposed waves, i.e. the interference phenomenon. In order to see this, one needs to use Euler's formula[15] and multiply by the complex conjugate. Then the phase shift factor becomes a cosine function in which the argument is the well known condition for constructive interference ($\cos(2\pi m) = 1$)

$$h_\mathrm{f} n_1 \cos\phi_1 = m\lambda \tag{2.67}$$

and destructive interference ($\cos[2\pi(m - 1/2)] = -1$)

$$h_\mathrm{f} n_1 \cos\phi_1 = \left(m - \frac{1}{2}\right)\lambda\,, \tag{2.68}$$

with m an integer. Thus the variation of $\Re(\beta)$ (Fig. 2.15 (e)) yields the variation in the intensity of the measured light through the interference phenomena.

In a similar way, taking into account that $I \propto E_0^2$ (Eq. (2.31)) and the connection between the extinction coefficient and the absorption coefficient (Eq. (2.16)), the absorption part in Equation (2.66) leads to the Beer-Lambert law of light absorption in a medium

$$I(x) = I_0 \mathrm{e}^{-\alpha x}\,. \tag{2.69}$$

Thus we link $\Im(\beta)$ to the absorption in a medium.

Now, after these clarifications, one can see a link between phase shift of the EM wave in the film and appearing peaks in transmission spectra (Fig. 2.15 (b)) that are attributed to the E_1(TO) and A_1(LO) phonon modes. Therefore, in $\Im(\beta)$ are two peaks nearby these phonon frequencies, thus light is absorbed stronger here. In $\Re(\beta)$ there is dip close to $\omega_{\mathrm{LO}(\|)}$ that also makes a contribution through the interference phenomenon. In order to illustrate the interference of light, the total transmitted complex-amplitude of the EM wave (Eq. (2.36)) is rewritten as series

$$T = t_{01}\, t_{12}\, \mathrm{e}^{-i\beta} \left[1 + \sum_{j=0}^{m=\infty} r_{10}^{j}\, r_{12}^{j}\, \mathrm{e}^{-i2j\beta}\left(1 - \delta_{j,0}\right)\right]\,, \tag{2.70}$$

with $\delta_{j,0}$ the Kronecker delta. In Figure 2.16 photometric values (Eq. (2.30)) of the latter expression are plotted for p-polarized light with various m values. When $m = 0$ only the prime transmitted beam is considered (Fig. 2.8). In this case one can observe the dip at $\omega_{\mathrm{LO}(\perp)}$, i.e. E_1(LO) phonon. However, adding one by one the reflected beams, i.e. increasing m, the beams superimpose and interfere. Thus the dip at $\omega_{\mathrm{LO}(\perp)}$ is canceled out and the uprise between the E_1(TO) and A_1(LO) phonon frequencies is flattened out.

Finally, an example of calculated reflection from semi-infinite medium, i.e. bulk, is

[15] $\mathrm{e}^{ix} = \cos(x) + i\sin(x)$.

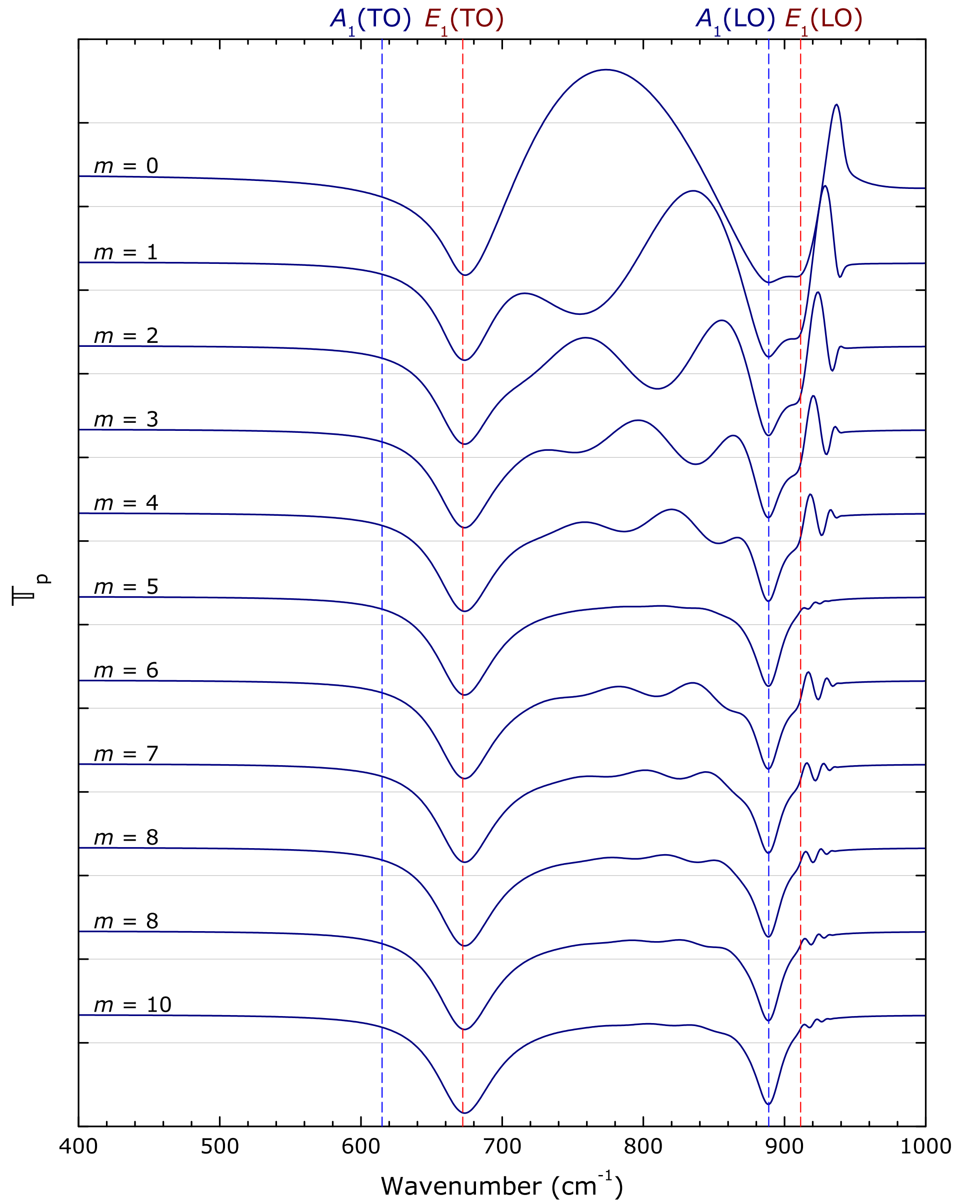

Figure 2.16: Transmission spectra of AlN/Si for p-polarized light, when different number (m) of multiple-reflected beams is taken into account (Eqs. (2.70) and (2.30), Fig. 2.8). The parameters used in the simulation are the same as in Fig. 2.15. The spectra are shifted for clarity.

illustrated in Figure 2.15 (g). In the ideal case, above the E_1(TO) mode till a certain frequency[16] the reflectivity is equal to unity with a dip between the A_1(LO) and E_1(TO) phonons for a p-polarized wave. This region is called the Reststrahlen band. An EM wave cannot propagate into a medium in the Reststrahlen band [84].

2.5.2 Experimental set-ups

FTIR spectroscopy

FTIR transmittance spectra were recorded in a nitrogen environment at room temperature with a NICOLET™ 8700 spectrometer, that is based on the Michelson interferometer. The measurements were done at normal (0°) and oblique (60°) angles of incidence using an unpolarized light over the 400-1200 cm^{-1} spectral range with a resolution of 0.25 cm^{-1}. The oblique angle of 60°, close to the Brewster's angle (≈ 64°), was chosen to have maximum transmission for p-polarized light trough the AlN/air interface (Fig. 2.7), because the p-polarization is needed to observe the LO phonon modes (Fig. 2.17). If the optic axis is parallel to the surface normal only the E_1(TO) and A_1(LO) mode phonons are asserting in the spectra and the modeling of such spectra was discussed in previous Section 2.5.1. If the optic axis of a film is not parallel to the surface normal the other two A_1(TO) and E_1(LO) mode phonons appear. However, the spectra modeling of such film is much more complicated and the inclination of the optic axis, i.e. *c*-axis of AlN, has to be known. All measured spectra were normalized to the transmission of a bare silicon substrate.

[16] Under normal angle of incidence it is up to $\omega_{LO(\perp)}$, s- and p-polarizations become equal.

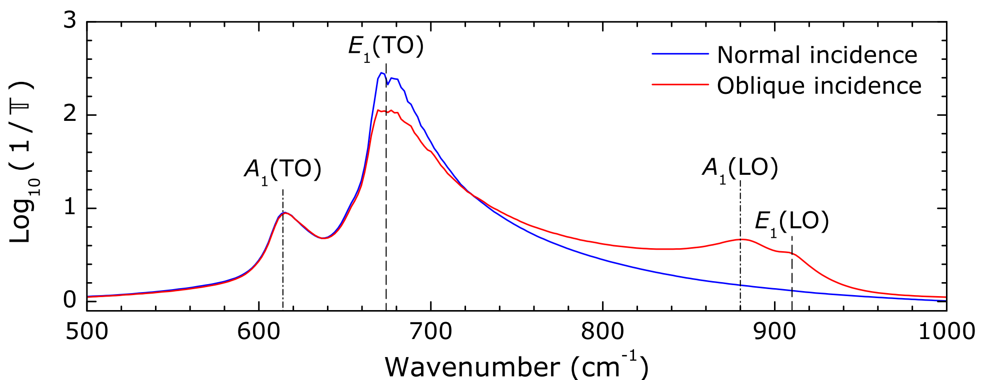

Figure 2.17: Measured FTIR transmission spectra of a 1100 nm thick AlN film taken at normal (0°) and oblique (60°) angles of incidence. The AlN film was deposited on a Si substrate using Ar:N_2 (20:30 sccm) gas discharge plasma at 400 W and 8 cm target-to-substrate distance. In-plane stress $\sigma = (0.32 \pm 0.04)$ GPa. The optic axis is not parallel to the surface normal.

Raman spectroscopy

Raman scattering with phonons is the inelastic scattering of light under emission or absorption of an optical phonon. Six phonons are allowed in Raman scattering from wurtzite AlN: A_1(TO), A_1(LO), E_1(TO), E_1(LO), E_2^1 and E_2^2 (Fig. 2.14 (b)). The allowed configurations, labeled with Porto notation [85] (Fig. 2.18), for Raman scattering are summarized in Table 2.2 [86].

In order to correctly evaluate the phonon lifetime from the Raman spectral line-width, the contribution of the instrumental bandpass broadening should be considered [46]. The Raman spectra had been acquired at successive slit widths ranging from 0.4 mm down to 0.08 mm (Fig. 2.19); the measured line-width values W_m were plotted as a function of the slit width W_s and extrapolated to the zero-slit value W_0 via the relation

$$W_\mathrm{m} = \sqrt{W_0^2 + (16.7 \times W_\mathrm{s})^2}. \tag{2.71}$$

Here the second term is the instrumental bandpass (in cm^{-1}/mm), i.e. the slit width multiplied by the monochromator linear dispersion.

Raman spectra were recorded with a HORIBA Jobin Yvon T64000 spectrometer using laser light of 488 nm wavelength at $z(yy)\bar{z}$ backscattering configuration. The slits of the monochromator were set to 0.1 mm.

2.6 NCD growth

As a prime pretreatment highly resistive (10-20 kΩ) Si(100) substrates were wet-cleaned using a standard cleaning procedure [87]. First they were sunk in hot sulfuric acid (H_2SO_4) and hydrogen peroxide (H_2O_2) (SPM, 1:1, 120°C) and after in ammonium hydroxide (NH_4OH), hydrogen peroxide (H_2O_2) and DI water mixture (APM, 1:1:5, 70°C). Substrates were then rinsed in DI water and dried under nitrogen gas flow. In case of AlN, the surface was cleaned in the same way as described in Section 2.1, to avoid surface damage by etching.

Initially cleaned substrates, Si and AlN/Si, were divided into six groups. Five groups were exposed to different plasma (Tab. 2.3): argon (Ar), hydrogen (H_2), nitrogen (N_2), oxygen (O_2) and tetrafluoromethane (CF_4), and one group left without any exposure to a pretreatment plasma. The surface pretreatment with H_2 plasma was done in ASTeX 6500 series MW PE CVD reactor, where the H_2 gas over the sample was exited by the microwave radiation. The other plasma pretreatments were done in a home-made physical vapor deposition (PVD) reactor.[17] The samples were placed on a biased stage (cathode, negative) and DC-pulsed current was applied (0.75 A, 400 V, 300 W) to achieve the gas discharge plasma over the samples. The plasma surface pretreatments were done for various timings in order to achieve different surface roughness.

[17] The same reactor was used for AlN deposition (Sec. 2.1).

Table 2.2: Raman selection rules for phonon modes of hexagonal AlN.

Scattering configuration[a]	Allowed modes				
$z(yy)\bar{z}$			E_2	A_1(LO)	
$z(xy)\bar{z}$			E_2		
$x(zz)\bar{x}$	A_1(TO)				
$x(yz)\bar{x}$		E_1(TO)			
$x(yy)\bar{x}$	A_1(TO)		E_2		
$x(yz)y$		E_1(TO)			E_1(LO)
$x(zx)z$	Q^{b}(TO)			Q(LO)	
$x(yy)z$	Q(TO)		E_2	Q(LO)	

[a]See Fig. 2.18 for clearance.
[b]Quasi-mode, mixed A_1 and E_1 phonon modes.

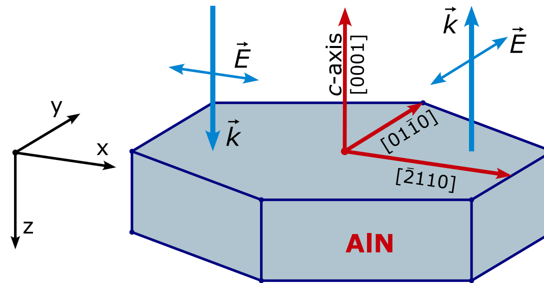

Figure 2.18: An example of Porto notation $z(xy)\bar{z}$. x, y and z are the axes of the Cartesian coordinate system. The x axis is parallel to [$\bar{2}$110], y axis is parallel to [01$\bar{1}$0], and z axis is defined parallel with the c-axis of AlN, i.e. [0001] direction. A laser beam is directed along the z direction and the backscattered light is collected $\bar{z}$, x indicates the polarization of incident light, whereas y indicates the polarization of collected light.

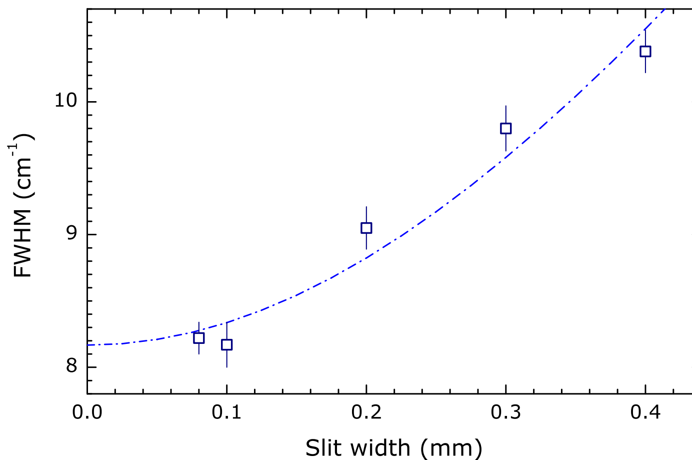

Figure 2.19: Evaluated full width at half maximum (FWHM) of the E_2^2 mode phonon as a function of monochromator slit width. The Raman spectra were measured on 3100 nm thick AlN film on Al_2O_3 from the $\mathcal{S}_{100\%}$ sample series (Tab. 2.1).

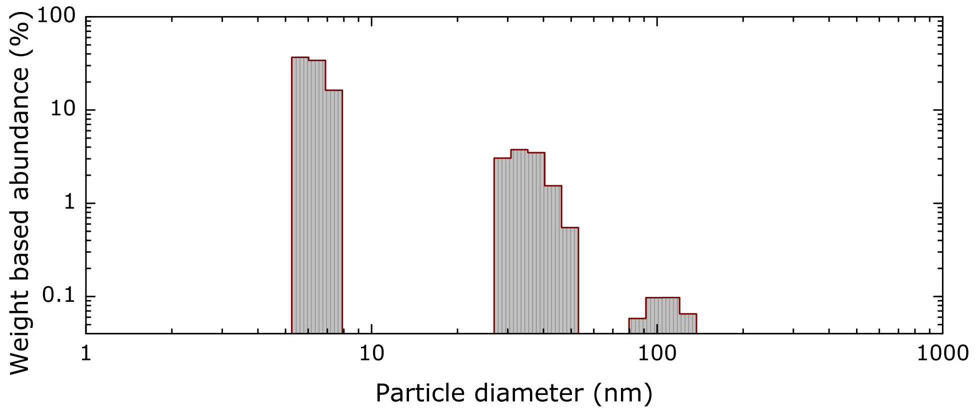

Figure 2.20: Particle size distribution as evaluated by dynamic light scattering.

After the pretreatment the substrates were immersed into an aqueous ND colloid for a few seconds. This colloid was prepared from detonation ND powder provided by the NanoCarbon Institute Co., Ltd., Japan. The ND size is 6-7 nm as measured by dynamic light scattering (Fig. 2.20) and the zeta-potential is (49 ± 5) mV at 4.8 pH. Following this treatment, the substrates were rinsed with pure DI water and dried using a spin-coater.

After the seeding procedure the samples were exposed to a conventional CH_4/H_2 plasma, typically used for a diamond growth, in an ASTeX 6500 series MW PE CVD reactor. The CH_4:H_2 ratio was 3%. The substrate temperature, monitored by a Williamson Pro92 dual wavelength pyrometer, was kept at 730°C using 3500 W of microwave power and a total gas pressure of 25 Torr. The NCD film thickness was monitored in-situ by measuring a light reflection from the grown film. The NCD growth was stoped after 12 min, when the laser reflection intensity reached the first interfernce minimum. According to calculations this corresponded to a film thickness of around 60 nm, which was later confirmed by scaning electron microscope cross-section image.

Table 2.3: Sample pretreatment conditions.

Pretreatment parameter	Ar [a]	CF_4 [a]	N_2 [a]	O_2 [a]	H_2 [b]
Substrate	Si, AlN	Si, AlN	Si, AlN	Si, AlN	Si, AlN
Gas flow rate (sccm)	50	42	50	50	500
Current (A)	0.73	0.75	0.72	0.72	
Voltage (V)	410	395	415	415	
Power (W)	300	300	300	300	3000
Base pressure (mPa)	< 0.5	< 0.5	< 0.5	< 0.5	< 0.5
Pretreatment pressure (Pa)	1.3	2.4	1.9	0.9	4000
Time (min)	0.5, 1, 2, 3	2	3	3	3

[a] Done in home build PVD system.
[b] Done in ASTeX 6500 series MW PE CVD reactor.

2.7 Morphology

2.7.1 X-ray diffraction

The structural characterizations of AlN films were performed by X-ray diffraction (XRD) using the Cu-$K_{\alpha 1}$ line (λ = 0.154056 nm). For the determination of the peak position, hence the c-lattice parameter of the AlN lattice, the θ-2θ locked coupled measurements were done on the Bruker D8 Discover. The important point is that samples were measured using a parallel beam setup. The parallel beam avoids the beam focusing issue, where due to different focus height with respect to the sample surface the observed XRD peak's position shifts. In case of a focusing beam setup, like on the Siemens D5000 Bragg-Brentano diffractometer, a small displacement of the sample can cause a beam shift. In case of parallel measurements only changes in the material itself are recorded, since the peak position is independent of the sample position. In a parallel beam setup additionally Cu-$K_{\alpha 2}$ line ($\lambda = 0.154439$ nm) is present with intensity approximately half of $K_{\alpha 1}$ line.

XRD rocking curves (θ-θ scan mode) were registered with a Siemens D5000 diffractometer. This high-resolution diffractometer uses focusing Bragg-Brentano geometry and is equipped with a primary Ge(111) monochromator, which allows the selection of a monochromatic Cu-$K_{\alpha 1}$ radiation.

2.7.2 Atomic force microscopy

The film surface topography and mean square roughness were measured with a Veeco NanoScope III MultiMode atomic force microscope (AFM) in tapping mode with a silicon cantilever. The surface roughness ρ_{rms} is represented by the root mean square value of the vertical deviations z_j of a real surface from its ideal form (z_{avg}) of all points ($N = 512 \times 512$) within a 1000×1000 nm^2 scan area

$$\rho_{\mathrm{rms}} = \sqrt{\frac{1}{N}\sum_{j=1}^{N}\left(z_j - z_{\mathrm{avg}}\right)^2}\,. \tag{2.72}$$

2.7.3 Scanning electron microscopy

The surface images were made using a FEI Quanta 200 FEG scanning electron microscope (SEM).

Part III

Main results

& Applications

Chapter 3

Stress, structural properties and phonons

In this chapter the main results are presented. The stress in AlN films (Sec. 3.1) and its relation to the structural properties of the films (Sec. 3.2.1) is analyzed. Section 3.3 focuses on the optical phonon behavior in AlN thin films, their frequency and lifetime correlation with film properties.

3.1 Stress

In this Section in-plane stress and out-of-plane strain in AlN films deposited using: (i) pure Ar (sample series $\mathcal{S}_{100\%}$) and (ii) Ar:N_2 mixture (sample series $\mathcal{S}_{50\%}$, Tab. 2.1) are investigated based on substrate curvature method and high-resolution XRD. Additionally, an etch-back experiment was done to show the existence of a stress gradient in the films.

3.1.1 In-plane stress

All sputtered AlN films showed residual in-plane stress for different film thickness (Fig. 3.1). For the films deposited using nitrogen plasma ($\mathcal{S}_{100\%}$) the highest compressive stress of −3 GPa is observed for the thinnest films (17 nm) and it gradually decreases with increasing film thickness (Fig. 3.1 (a)). In case of AlN on Si(100) substrates the decline of stress tends to level off at around −0.4 GPa, while in case of Al_2O_3(0001) substrates the stress in the AlN films undergoes a change to tensile

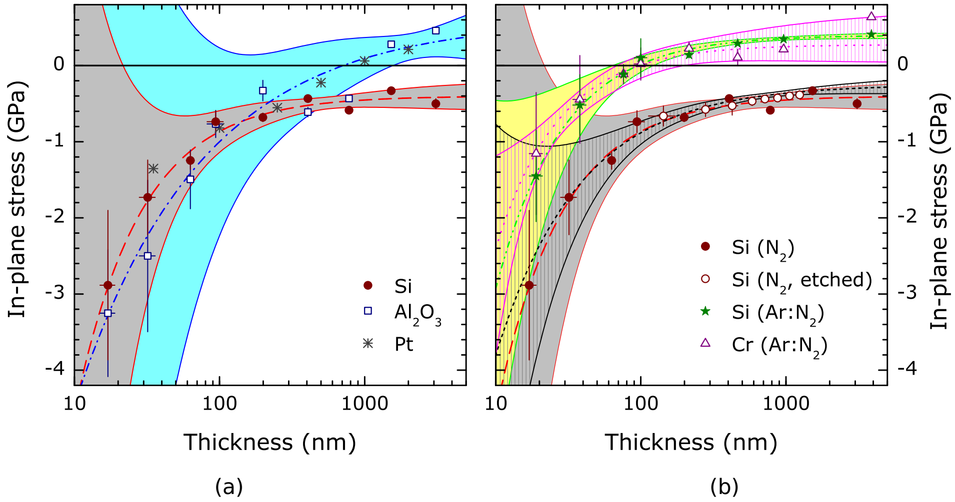

Figure 3.1: In-plane stress versus film thickness. Sample series $\mathcal{S}_{100\%}$: Si (full (a, b) and open circles (b), the latter representing the results of the etching experiment) and Al_2O_3 (open squares (a)). Sample series $\mathcal{S}_{50\%}$: Si (full stars (b)) and Cr/Si (open triangles (b)) (Tab. 2.1). The lines are fits to the data points with 90% confidence bands (Eq. (3.3), Tab. 3.1). Asterisk represents results of AlN/Pt(111), data taken from Ref. [40].

stress and tends to increase further reaching +0.46 GPa at 3100 nm film thickness. On both substrates AlN experiences the biggest reduction in stress during the first 100 nm of the film deposition. In comparison, Martin *et al.* [40] measured similar stress values in AlN on (111) oriented platinum (Pt) (Fig. 3.1 (a), asterisk). It can be clearly seen that the resulting stress behavior up to 150 nm thickness is irrespective of the used substrate material and the subsequent magnitude of lattice mismatch $f = b/a - 1$, where a and b are the lattice parameters or interplanar distances of the substrate and the film, respectively: from −29.8% to +14.6% for Si(100) depending on the epitaxial relationship [88], +13.3% for Al_2O_3(0001) [33, 89] and +12.3% for Pt(111) [40]. On the contrary, the change of the gas composition used in the AlN deposition process on Si(100) showed a much larger influence than the substrate material (Fig. 3.1 (b)). One can see that all data points are equaly shifted upwards when changing the nitrogen composition in the gas discharge plasma from 100% to 50%. This shift has been reported to be linear with $Ar{:}N_2$ ratio in the used deposition system [25].

In order to prove the possible presence of an in-plane stress gradient, a stepwise layer-by-layer etch of the 1500 nm thick AlN sample ($\mathcal{S}_{100\%}$) on Si(100) was performed (Fig. 3.1 (b), open circles). After each etch step, i.e. for thinner film, the in-plane stress increased. A similar trend was observed in sputtered thin TiN films and it was attributed to the presence of a stress gradient in the film [41].

To have a better view on the in-plane stress gradient, the results are plotted as an integrated stress versus the film thickness (Fig. 3.2 (a)). Assuming that the stress is dependent on the substrate/film interface distance z, $\sigma(z)$, the average in-plane

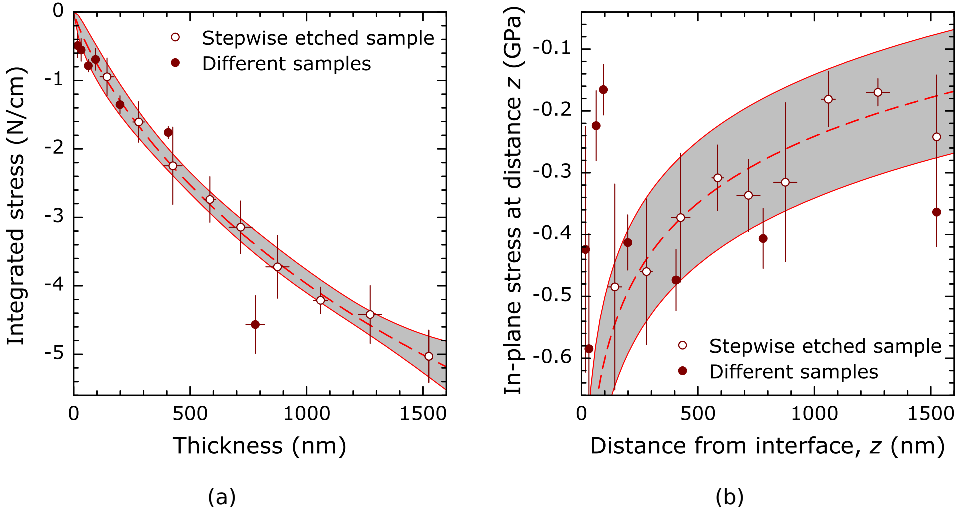

Figure 3.2: (a) Integrated in-plane stress ($\langle\sigma(h_f)\rangle\, h_f$, Eq. (3.1)) versus film thickness of the stepwise etched AlN(1500 nm)/Si sample (open circles) and different samples of different thickness (full circles), samples are from series $\mathcal{S}_{100\%}$. The dashed line is a non-linear fit to the data points with 95% confidence band. (b) The derivative of the integrated stress with respect to the thickness (Eq. (3.2)).

stress that is measured in a film with the thickness h_f, $\langle\sigma(h_f)\rangle$, follows [39,90]:

$$\langle\sigma(h_f)\rangle = \frac{1}{h_f}\int_0^{h_f} \sigma(z)\,\mathrm{d}\,z. \tag{3.1}$$

In this case, the value of $\sigma(z)$ can be calculated by differentiating $\langle\sigma(h_f)\rangle\, h_f$ with respect to h_f at the point $h_f = z$:

$$\sigma(z) = \left.\frac{\mathrm{d}\left[\langle\sigma(h_f)\rangle\, h_f\right]}{\mathrm{d}\, h_f}\right|_{h_f=z}. \tag{3.2}$$

In Figure 3.2 (a) one can see that the integrated stress $\langle\sigma(h_f)\rangle\, h_f$ (Eq. (3.1)), of the stepwise etched sample has a non-linear behavior. The derivative of the integrated in-plane stress with respect to the thickness, Equation (3.2), reveals that the stress gradient is present (Fig. 3.2 (b)).

The average in-plane stress in a polycrystalline film can be described by a power law relation [90]:

$$\langle\sigma(h_f)\rangle = A + B h_f^{-p}, \tag{3.3}$$

with the stress value A to which $\langle\sigma(h_f)\rangle$ converges at large h_f, B the coefficient related to the shrinkage of the grain boundary and p an exponent. If the latter equation is

Table 3.1: Fitting parameters of Equation (3.3) determined using nonlinear regression fitting of the average in-plane stress dependence on film thickness (Fig. 3.1).

		A (GPa)	B (Pa m^p)	p
AlN/Al_2O_3[a]	– · –	$+(0.60 \pm 0.09)$	$-(0.016 \pm 0.005)$	0.50 ± 0.07
AlN/Si[a]	– – –	$-(0.40 \pm 0.04)$	$-(0.037 \pm 0.024)$	0.95 ± 0.15
AlN/Si[a,b]	- - - -	$-(0.25 \pm 0.04)$	$-(0.020 \pm 0.010)$	0.75 ± 0.11
AlN/Si[c]	– ·· –	$+(0.40 \pm 0.02)$	$-(0.029 \pm 0.021)$	0.94 ± 0.16
AlN/Cr/Si[c]	·····	$+(0.28 \pm 0.02)$	$-(0.027 \pm 0.028)$	1.00 ± 0.24

[a]Deposited using N_2 plasma ($\mathcal{S}_{100\%}$).
[b]Combined with etching experiment.
[c]Deposited using Ar:N_2 plasma ($\mathcal{S}_{50\%}$).

differentiated as Equation (3.2), one gets

$$\sigma(z) = A + B(1-p)z^{-p}, \tag{3.4}$$

where pre-factor $B(1-p)$ and exponent p can be used to estimate the magnitude of a stress gradient. Although Equation (3.3) was derived to explain the tensile stress in polycrystalline films by the stress generation at the grain boundaries, it can also be applied to the compressive stress as it is based on extra atoms insertion in to the grain boundary [91]. Hence the competition between tension and compression occurs, which in turn depends on the deposition conditions [39]. Using Equation (3.3) the fits to the experimental points were made (Fig. 3.1). The consequent fitting parameters are listed in Table 3.1. Although the parameters obtained are not determinate by their nature [92], still they can be used to outline the trend. The in-plane stress of AlN films deposited on Si using two types of plasma were fitted with slightly different $B(1-p)$ and nearly the same $p \approx 1$, which indicates that the stress gradient in these films is smaller than in AlN films on Al_2O_3. Also one can note that the change of the plasma composition from 100% N_2 to 50% N_2 in the deposition process shifted the stress values by +0.8 GPa. A comparison of AlN films on Al_2O_3 and Si substrates implies that AlN growth on sapphire substrate must have different morphology. Such analysis is done in Section 3.2.1.

3.1.2 Out-of-plane strain

The XRD studies (Sec. 3.2.1, θ-2θ scan mode, Fig. 3.4 (a)) showed that all AlN films were with c-axis orientation perpendicular to the film surface, i.e. only the (0002) Bragg peak of AlN was present, on both Si(100) and Al_2O_3(0001) substrates and on sputtered Cr layer. In case of sputtering using N_2 plasma, the AlN(002) peak shifts with increasing film thickness. Thus, the distance between crystal planes changes (Fig. 3.3(a)), similarly as the in-plane stress, indicating that the strain along the c-axis behaves linearly with the in-plane stress (Fig. 3.3(b)). In case of biaxial stress, the in-plane stress σ and out-of-plane strain ϵ are linked via Young's modulus

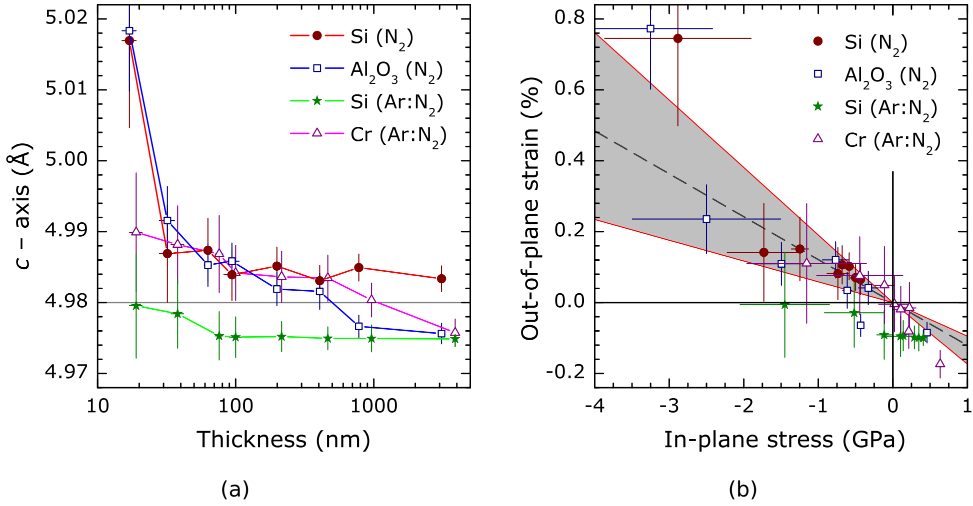

Figure 3.3: AlN *c*-lattice parameter versus film thickness (a) and out-of-plane strain versus in-plane stress (b) of AlN films on: Si(100) (full circles) and Al_2O_3(0001) (open squares), deposited using N_2 plasma, and AlN films deposited on Si(100) (full stars) and Cr/Si(100) (open triangles) using Ar:N_2 (1:1) plasma. The dashed line is a linear fit to the data points with 95% confidence band (excluding full stars) with a slope of $-(1.21 \pm 0.21)\,\mathrm{TPa}^{-1}$.

Y and Poisson's ratio ν as in [93]

$$\epsilon = -2\,\frac{\nu}{Y}\,\sigma, \tag{3.5}$$

where ν and Y are given in terms of the elastic stiffness constants[1] C_{ij} as

$$\nu = \frac{C_{13}}{C_{11} + C_{12}}, \tag{3.6}$$

and

$$Y = C_{33} - \frac{2C_{13}^2}{C_{11} + C_{12}}. \tag{3.7}$$

Thus, the slope of a linear fit will yield the $-2\nu/Y$ value. The fit result, a slope of (-1.16 ± 0.12) TPa^{-1}, falls in the range of other experimental [94–96] and calculated [93, 97–101] data available (Tab. 3.2). In order to have an intersection at zero, the strain-free *c*-lattice parameter was determined to be 4.980 Å for AlN sputtered using pure N_2 plasma. In case of AlN on Cr (Ar:N_2) *c*-lattice parameter was set to 4.984 Å. These results within the error range agree with the experimentally determined 4.9816 Å value by Angerer *et al*. [102]. Here it is pointed out that the

[1] The Hooke's law can be expressed in matrix notation as $\hat{\sigma} = \hat{C}\hat{\epsilon}$, with $\hat{C}$ the the stiffness tensor [42].

Table 3.2: Values of $-2\nu/Y$ (in TPa^{-1}) compared with results of other measurements and *Ab initio* calculations.

This work	Magnetron sputtering	1.21 ± 0.21
Experiment	Single crystal [94]	1.00
	PIMBE[a] [95]	1.03
	MOCVD[b] [96]	1.53
Calculated	DFT-LDA,[c] FP-LMTO[d] [97]	0.72
	Hartree-Fock theory [98]	1.04
	DFT-LDA, PPPW[e] [99,100]	1.23
	DFT-LDA, PPPW [93]	1.30
	DFT-LDA, PP[f] [101]	1.62

[a]Plasma-induced molecular beam epitaxy.
[b]Metal-organic chemical vapor deposition.
[c]Density functional theory within local-density approximation.
[d]Full-potential linear muffin-tin orbital method.
[e]Pseudopotential plane-wave method.
[f]Pseudopotential method.

residual in-plane stress is the main mechanism of constant c-lattice deviation from the stress-free case. Nevertheless, in Figure 3.3 (b) the first data points from the left, corresponding to the thinnest films of 17 nm, are significantly deviated from the fitted line. It is very likely that the AlN film had not yet coalesced rendering the Stoney equation invalid, leading to a miscalculation of the stress as the surface stress should be taken into account [103].

A completely different result is obtained for the sample series on Si(100) deposited using Ar:N_2 plasma. For films thicker than 80 nm the c-axis parameter does not change much with increasing film thickness as well as no significant influence of the in-plane stress on the out-of-plane strain was observed. One can speculate that: (i) there is no stress gradient after $z > 80$ nm and the upper layers are at the constant stress, thus the XRD peak does not shift, but the measured average in-plane stress is still changing according to Equation (3.1) and/or (ii) when the in-plane stress in the film makes the transition from compressive to tensile the stress relaxes through the grain boundaries and the strain along c-axis of AlN vanishes. However, in the first case it would contradict the results observed for the sample series deposited on Si using N_2 plasma as it also shows a rather small stress gradient. In the second case one would need to confirm plastic deformation at the grain boundaries. Moreover, AlN films on Cr interlayer also show similar tensile in-plane stress as on Si, but the out-of-plane stain is changing as in case of biaxial stress. Thus, the etch-back experiment should be done including XRD analysis after each etch step to confirm such behavior and correlation between the samples.

3.2 Structural properties

In this Section the structural properties of AlN films are analyzed with XRD and AFM techniques. Due to smooth surface and the fact that AlN is highly resistive material, the SEM was incapable to characterize AlN surface.

3.2.1 XRD

For the determination of the *c*-lattice parameter of AlN, the θ-2θ locked coupled measurements were done using a parallel beam setup (Fig. 3.4 (a)). In this setup the $K_{\alpha 1}$ line is accompanied by $K_{\alpha 2}$ line, thus the peak was fitted with double pseudo-Voigt profile in order to evaluate the lattice inter-plane distance (Fig.3.3 (a)). Further analysis of *c*-lattice parameter variation with film thickness was described in Section 3.1.2.

To check the crystalline quality of the films, the XRD rocking curve (RC) measurements of AlN (0002) peak (θ-θ scan mode), were performed (Fig. 3.4 (b)). The full width at half maximum (FWHM) of the RC peak variation with film thickness is plotted in Figure 3.5. Despite some scattered points, the AlN films on sapphire show the narrowest peaks indicating the highest degree of orientation. In case of AlN on silicon the growth of the film starts highly disordered and improves for thicker films. Hence, the dislocation density and other structural defects are decreasing [104]. AlN films on Si deposited under two different conditions, show the same FWHM of the rocking curve peak and both have a low in-plane stress gradient. In contrast, the AlN films on Al_2O_3 show higher quality as well as higher in-plane stress gradient than in films on Si. Thus, one can conclude that the lower the density of structural defects the higher the in-plane stress gradient is in the films. In case of AlN on Cr interlayer, RC measurements showed even broader RC peaks and the quality improve with film

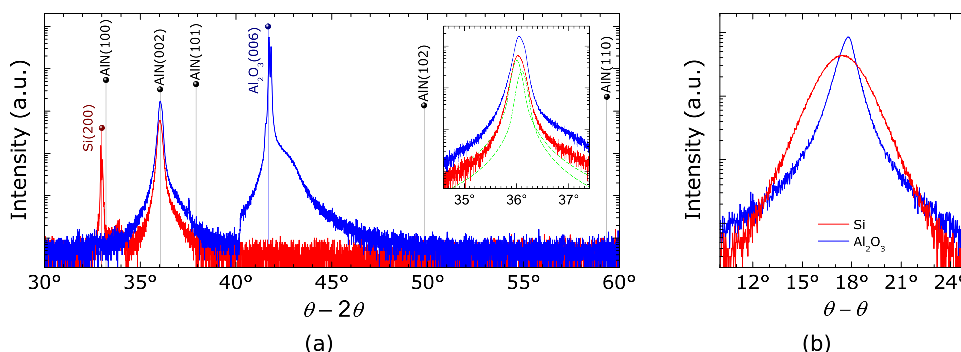

Figure 3.4: XRD θ-2θ (a) and θ-θ (b) scans of 200 nm thick AlN on Si (red curve) and Al_2O_3 (blue curve). The layers were deposited using N_2 gas discharge plasma. Due to the presence of $K_{\alpha 2}$ line in θ-2θ scan mode the observed peaks have a shoulder on the right side (a, inset). The peak 33° is attributed to Si(200) forbidden mode confirmed by measuring bare Si substrate.

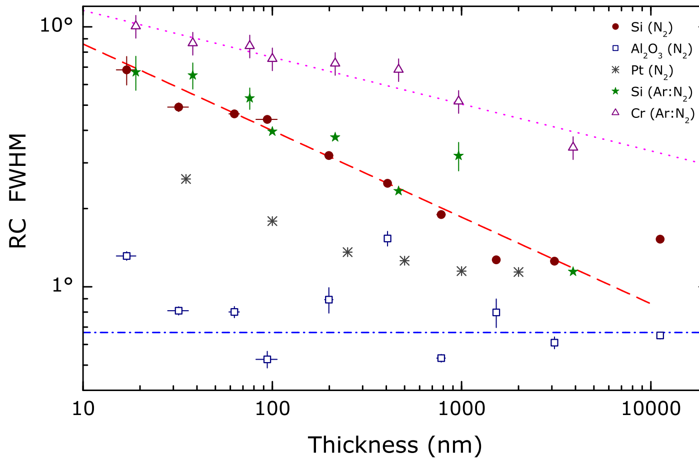

Figure 3.5: Full width at half maximum (FWHM) of a rocking curve (RC) versus thickness of AlN films on: Si(100) (full circles), Al_2O_3(0001) (open squares) and Pt(111) (asterisk, data obtained from Ref. [40]), deposited using N_2 plasma, and AlN films deposited on Si(100) (full stars) and on Cr/Si (open triangles) using Ar:N_2 (1:1) plasma. The dashed lines are guides for the eyes.

thickness was the slowest. A comparison study of AlN on different metal interlayer is presented in Section 4.1.

3.2.2 AFM

Atomic force microscopy was applied to evaluate the surface morphology of the films (Fig. 3.6). Independent of the substrate material, the roughness is increasing with increasing thickness (Fig. 3.7(a)). This trend was also observed by Meinschien *et al*. [89] and explained by the columnar growth of AlN along the *c*-axis. However, these results do not support the presumption of Martin *et al*. [40] that an increasing roughness and shadowing effect cause a tensile stress in thicker films.

Indicated by AFM, both the lateral size and height of the AlN crystallites increased with film thickening, whereas the measured density of grain boundaries (length per surface area) decreased (Fig. 3.7(b)). One can see that for the same film thickness AlN samples on Si deposited using Ar:N_2 plasma have a lower density of grain boundaries compared to samples deposited using N_2 plasma. This is one of the reasons why the in-plane stress values are different, i.e. equally shifted. The lower density of grain boundaries the less possibility for extra atoms to be inserted in to the grain boundary, which in turn decreases the compressive stress. The second factor, which reduces the compressive stress in the films, is the deposition conditions. Sheldon *et al*. [39] observed higher tensile stress in AlN grown at higher rates by molecular beam epitaxy. In this work the deposition rate using Ar:N_2 plasma was higher (81 nm/min)

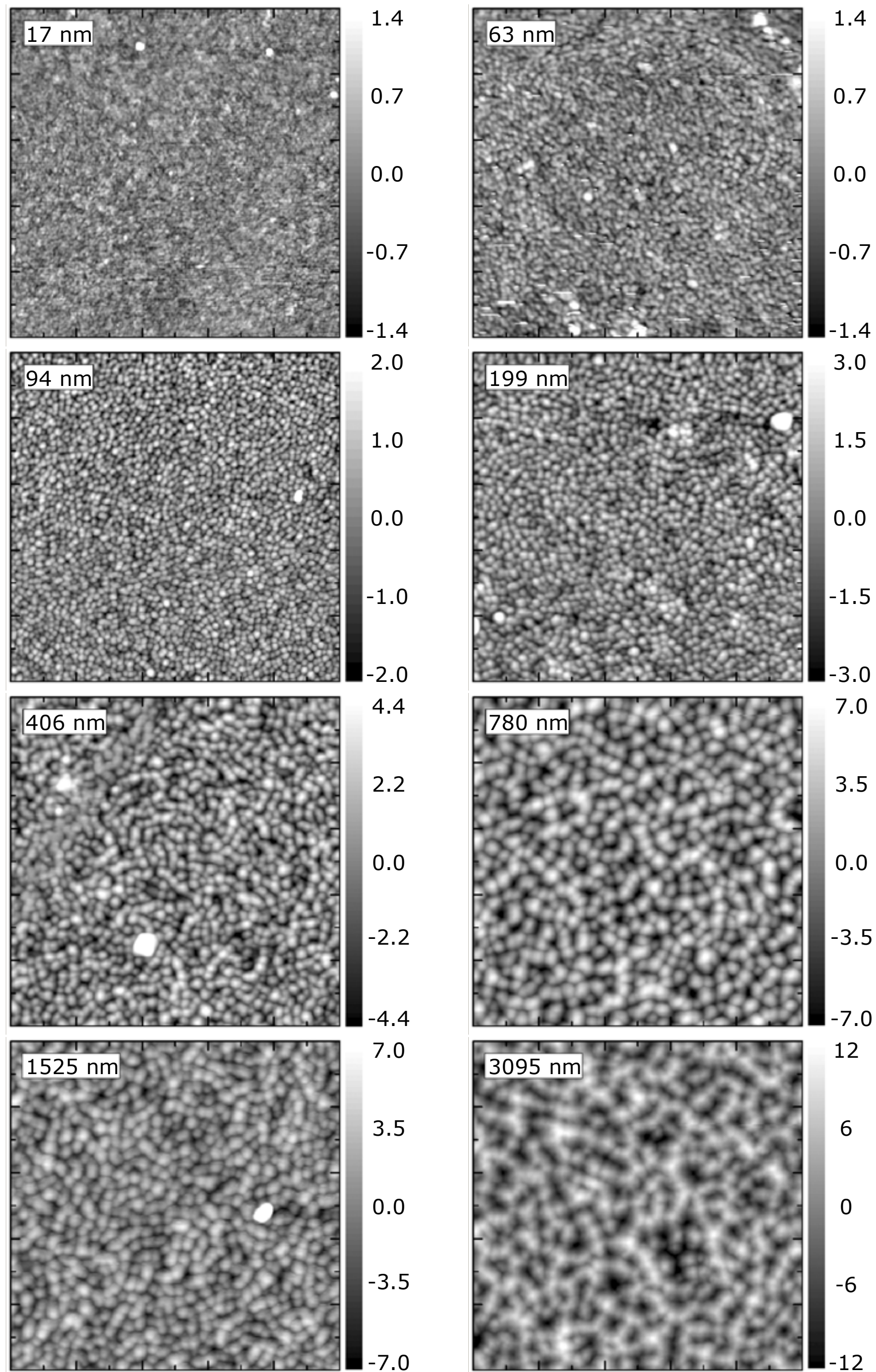

Figure 3.6: AFM images of AlN on Al_2O_3 substrates. Scan area 1000 × 1000 nm, the scales on the right indicate the surface height variation in nanometers.

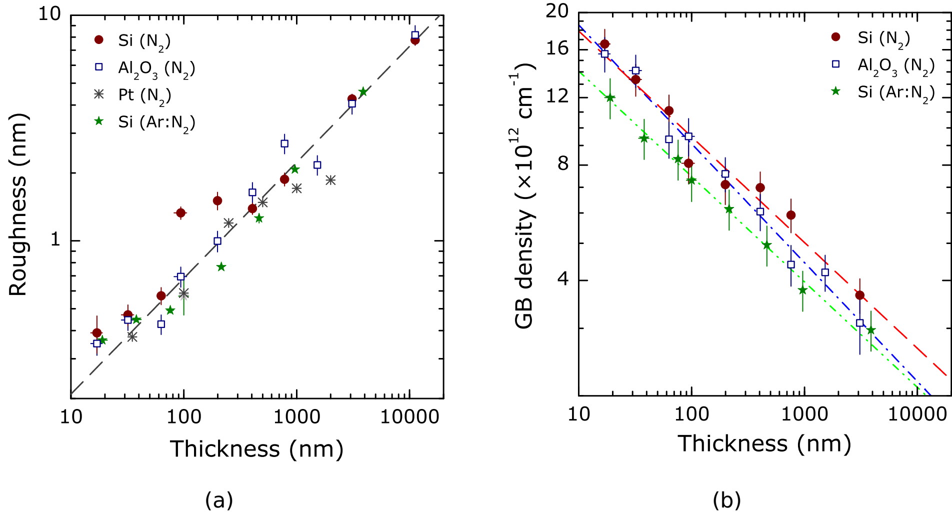

Figure 3.7: Roughness (a) and density of grain boundaries (b) versus thickness of AlN films on: Si(100) (full circles), Al_2O_3(0001) (open squares) and Pt(111) (asterisk, data obtained from Ref. [40]), deposited using N_2 plasma, and AlN films deposited on Si(100) (full stars) using Ar:N_2 (1:1) plasma. The dashed lines are guides for the eyes.

than using N_2 plasma (64 nm/min). A similar situation appears comparing AlN films on Si and Al_2O_3 substrates deposited using N_2 plasma, where the deposition rate is the same, but the density of grain boundaries is decreasing slightly faster on Al_2O_3 substrates. Hence, this confirms the observation of higher stress gradient in the AlN films on Al_2O_3 substrates. However, the average in-plane stress and the stress gradient differ more radically between the films than the density of grain boundaries. This implies that the density of grain boundaries has minor importance, whereas the quality of the film has much more influence on the in-plane stress behavior for the sputtered AlN thin films.

3.3 Optical phonons

For better insight in the AlN films, an infra-red light absorption measurements were performed in order to analyze the phonon dynamics. As predicted theoretically, the experimental observation shows that optical phonons shift to lower energies with increasing AlN film thickness, i.e. with decreasing stress (Fig. 3.10). As well the phonon absorption peak width can give additional information on film quality, but here further modeling is needed. In the end estimated lifetime of observed phonon mode can be used as a quality control procedure for thin films.

In this section thin AlN films of different thickness deposited on silicon substrates using N_2 plasma are studied. The investigation of the films is performed by FTIR and

Raman spectroscopy. In former case the transmission spectra are recorded under normal and oblique angles. With the intent to extract the properties of the E_1(TO) and A_1(LO) optical phonon modes, simulations of the spectra were made using the factorized model of a damped oscillator, taking into account the presence of birefringence and the thin film interference phenomenon (Sec. 2.5). As a result the E_1(TO) and A_1(LO) phonon modes were characterized by their energy and lifetime. Additionally, rough estimation of A_1(TO) and E_1(LO) phonon modes frequencies is made. In the Raman spectra only the E_2^2 phonon mode is sufficiently intense for reliable investigation. An additional investigation of correlation between the stress and morphology of the films with the phonon behavior, leads to a better fundamental understanding.

3.3.1 FTIR

In FTIR spectra measured under the normal light incidence only the E_1(TO) phonon mode is visible (Fig. 3.8). Under oblique angle conditions the A_1(LO) phonon mode is visible because an alternating electric field of p-polarized light has a component parallel to the lattice *c*-axis, which induces a response from the extraordinary dielectric function and gives rise to Berreman effect [79]. In films under the investigation, only E_1(TO) and A_1(LO) phonon modes are represented by two peaks as the the optical axis of AlN is perpendicular to the film surface. There is other case possible, when the optical axis is under oblique angle respect the surface, more complicated Fresnel coefficients emerge [68] and light-matter interaction gives rise for A_1(TO) and E_1(LO) phonon modes peaks (Fig. 2.17). XRD studies showed, that the samples have a perfect *c*-axis orientation perpendicular to the film surface, so the optical axis of AlN too, we continue with simpler case of the Fresnel equations (Sec. 2.3.4).

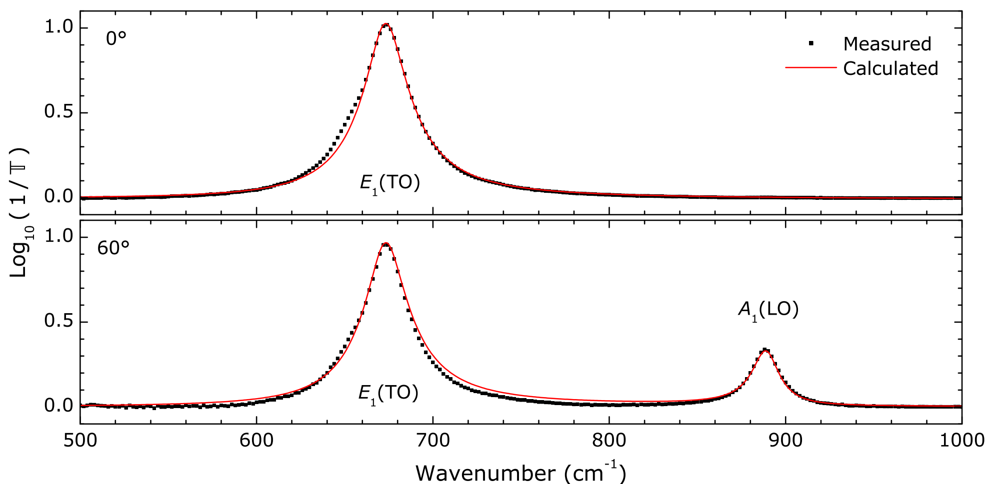

Figure 3.8: Measured (points) and calculated (line) FTIR transmission spectra of a 200 nm thick AlN film taken at normal (0°) and oblique (60°) angles of incidence.

In the calculated spectra the phonon frequencies and damping constants of E_1(TO) and A_1(LO) modes determine the peak position and width, respectively. Although in the FTIR spectra there are only two peaks visible, the frequencies and damping constants of E_1(LO) and A_1(TO) phonon modes are also used. The parameters of these phonon modes were determined by means of modeling, though they showed a negligible influence on the peaks. From the damping constants of the E_1(TO) and A_1(LO) phonon modes the corresponding lifetimes τ are estimated using the energy-time uncertainty

$$\Gamma\tau = \hbar, \tag{3.8}$$

with $\hbar = 5.3\times10^{-12}$ cm^{-1} s the reduced Planck constant (Fig. 3.9). The experimental line broadening has two origins: homogeneous (intrinsic) and inhomogeneous (extrinsic). The measured average in-plane stress in the films changes with the film thickness (Fig. 3.1), therefore the presents of a stress gradient and inhomogeneous broadening of the peaks would be expected. However, the in-plane stress analysis in Section 3.1 reveals that the stress gradient, i.e. the variation of $\sigma(z)$, is of 0.3 GPa order (Fig. 3.2 (b)). Such change in $\sigma(z)$ will shift the phonon resonance peak by $\lesssim 1$ cm^{-1} and give an inhomogeneous peak broadening [93], which is negligible when compared to the estimated $\Gamma_{\mathrm{TO},\perp} \approx 18$ cm^{-1} and $\Gamma_{\mathrm{LO},\parallel} \approx 9$ cm^{-1}. Although it is difficult to predict stress evolution at small thickness (< 100 nm) the inhomogeneous peak broadening resulting from it is negligible. After all, even if a higher stress gradient than the one detected now would be present in the below 100 nm layers, the additional broadening would be small compared to Γ. Thus we assume that the compressive stress in the film is quasi-homogeneous and is generated at the film/substrate interface due to high lattice mismatch.

In case of a homogeneous film there are three possible contributions to the phonon broadening: (i) the anharmonic decay of zone-center optical phonons into zone-edge acoustic phonons, (ii) the inhomogeneous scattering of phonons by defects, and (iii) the confinement of phonons. The phonon confinement is not expected because the thickness of the films and the crystalline size estimated by XRD and AFM are well above 10 nm [105]. The main contributions to the total phonon lifetime τ_{t} come from an anharmonic decay time τ_{a} and a defect scattering time τ_{d} according to

$$\tau_{\mathrm{t}}^{-1} = \tau_{\mathrm{a}}^{-1} + \tau_{\mathrm{d}}^{-1}. \tag{3.9}$$

Usually there are three classes of defects in sputtered AlN: (i) impurities and other point defects, (ii) dislocations (line defect) and (iii) grain boundaries (planar defect). It is safe to assume that some of the defects are homogeneously incorporated over the film thickness and constitute a background defect level, e.g. impurities, whereas the amount of other defects is changing with film thickness, e.g. dislocations and grain boundaries.

The full width at half maximum (FWHM) of the rocking curve (RC) peak is determined by the structural features and dislocation densities [104]. In our films the FWHM of AlN (002) RC peak decreases with the film thickness (Fig. 3.5). Although a sophisticated analysis of broadening is required to determine the density of dislocations,

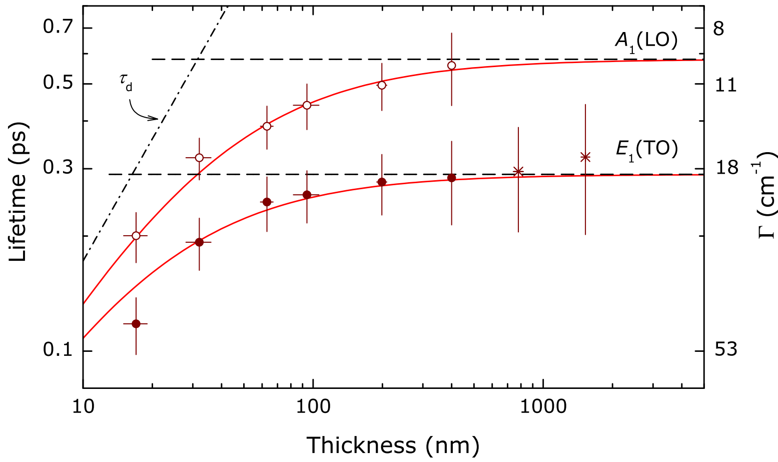

Figure 3.9: E_1(TO) and A_1(LO) phonon mode lifetimes versus AlN films thickness denoted in full and open points, respectively. The solid lines are fits using Eq. (3.9), the dashed lines are the τ_a components affected by background defects and the dashed-dot line is τ_d component. Asterisks are the rough estimations from so-called truncated FTIR spectra that were hampered by detector limitations due to high absorption in thick films.

falling outside the scope of this thesis, we use the broadening of the RC as a figure of merit for the number of imperfections in the film. Therefore, the density of defects ϱ_d should also decrease proportionally with film thickness and increase τ_d as $\tau_d \propto \varrho_d^{-1} \propto h_f^p$. With this assumption and keeping in mind that there is a background defect concentration the fitting of the data points using Equation (3.9) were made (Fig. 3.9). The decay times, governed by anharmonic decay and background defect scattering, were estimated at (0.29 ± 0.03) ps and (0.58 ± 0.05) ps for the E_1(TO) and A_1(LO) phonon modes, respectively. In Table 3.3 we compare our data of thin films with the experimental values obtained on bulk crystals [46–48, 50] and calculated data [106, 107] available in the literature. The lifetime of the E_1(TO) phonon mode in AlN thin film is strongly reduced. The result obtained for the A_1(LO) phonon mode is similar as in single crystal. This observation could be due to the fact that sputtered AlN has a columnar structure [108]. The grain boundaries thread along the *c*-axis and the displacement of atoms in the A_1(LO) phonon mode are not disturbed (Fig. 2.14 (b)). The displacement of atoms in the E_1(TO) phonon mode appears perpendicular to the *c*-axis, thus the lifetime of this mode is strongly affected by the grain boundaries.

Upon an increase of AlN film thickness the frequencies of all the phonon modes redshift (Fig. 3.10). This shift is due to the decrease of stress in the films. Wagner and Bechstedt calculated the coefficients of phonon frequency linear shift per unit stress [93], which fit well to our data allowing to determine the stress-free phonon frequencies (Tab. 3.3).

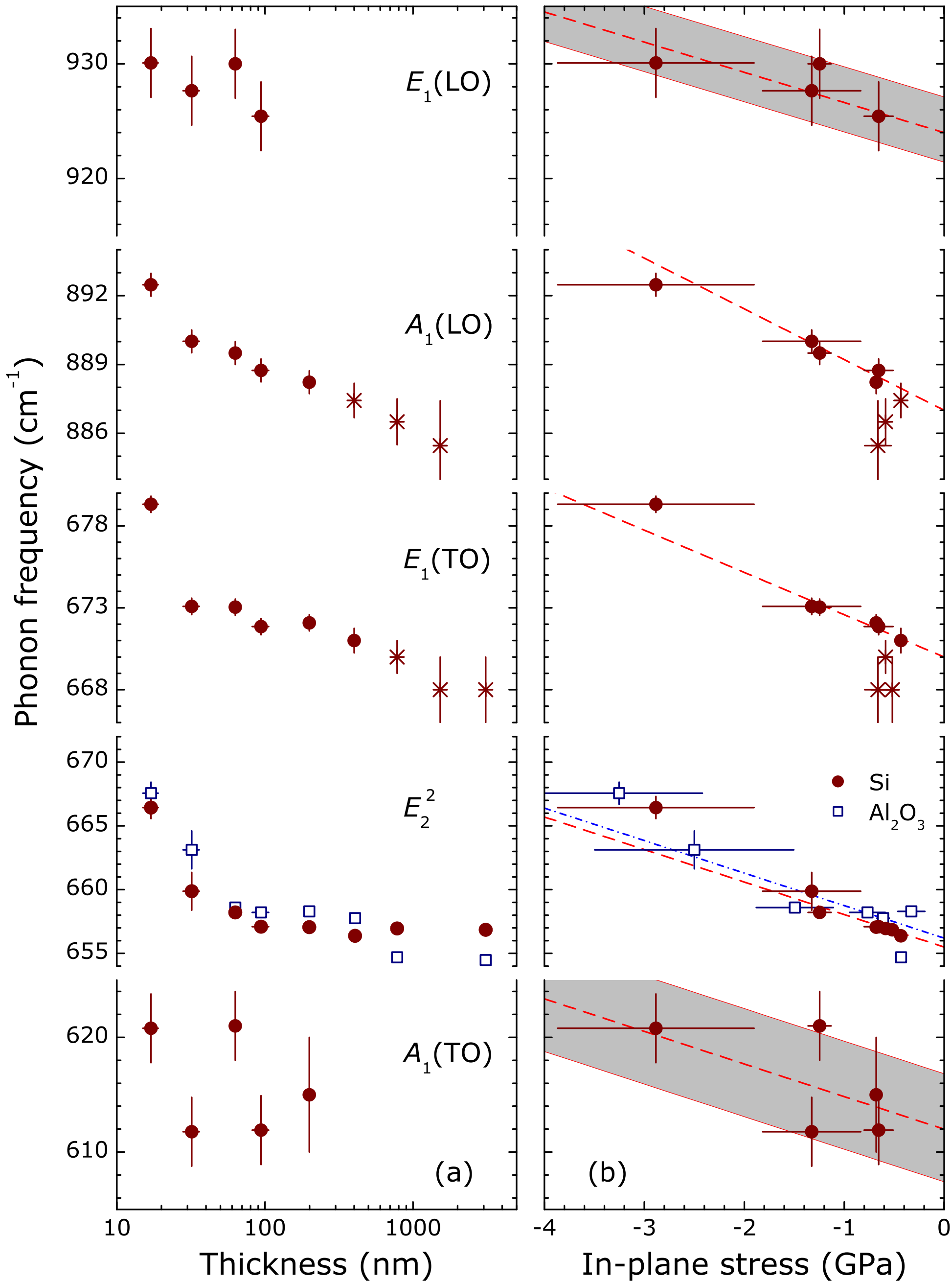

Figure 3.10: A_1(TO), E_2^2, E_1(TO), A_1(LO) and E_1(LO) phonon mode frequencies versus AlN film thickness (a) and in-plane stress (b). The full points are for AlN on Si and open squares are for AlN on Al_2O_3. The dashed lines are fits to the data points with slopes taken from Ref. [93]. Asterisks are the rough estimations from truncated FTIR spectra. The grey bands are the confidence of 95%.

Table 3.3: Phonon frequencies ω (in cm^{-1}) and lifetimes τ (in ps) in AlN.

	A_1(TO)		E_1(TO)		E_2^2		A_1(LO)		E_1(LO)	
	ω	τ	ω	τ	ω	τ	ω	τ	ω	τ
This work[a]	612 ± 5		670 ± 1	0.29 ± 0.03	655.5 ± 0.5	0.71 ± 0.05	887 ± 1	0.58 ± 0.05	924 ± 5	
This work[b]					656.2 ± 0.5	0.88 ± 0.05				
Exper.[c]	609		668				885.8			
Exper.[d]			663							
Exper.[e]	608		668	0.91[f], 0.53[g]	655	0.83[f], 0.43[g]	890	0.45[f], 0.28[g]		
Exper.[h]	608.5	1.20	667.2	1.80	655.1	1.70	888.9	0.72	909.6	0.70
Exper.[i]	610	0.79	669	1.00			889	0.60	916	0.51
Exper.[j]	610		670		657	1.75	890	0.57	912	
Calc.[k]	618		677		667		898		924	
Calc.[l]		0.41		0.46		0.89		0.16		
Calc.[m]								0.80		

[a] Thin film on Si(100), reactive DC magnetron sputtering, FTIR.
[b] Thin film on Al_2O_3(0001), reactive DC magnetron sputtering, Raman.
[b] Thin film on Si(111), MBE, Raman, Ref. [51].
[c] Thin film on *a*-sapphire, reactive DC magnetron sputtering, FTIR, Ref. [52].
[d] Bulk single crystal, Raman, Ref. [46].
[e] Sample referred to as transparent.
[f] Sample referred to as blue; the density of Si and C impurities is two orders of magnitude higher than in a transparent sample.
[g] Bulk single crystal, Raman, Ref. [48].
[h] Bulk single crystal, FTIR, Ref. [50].
[i] Bulk single crystal, Raman, Ref. [47, 109].
[j] *Ab initio*, Ref. [93].
[k] Fermi's golden rule involving anharmonic interaction between phonons, with the Grüneisen's constant $\gamma = 0.8$, Ref. [106]. Results of Ref. [47] fitted with $\gamma = 0.41$.
[l] An adiabatic bond charge model and crystal anharmonic potential within the isotropic elastic continuum model, Ref. [107]. Results of Ref. [47] fitted with $\tau_d = 2.1$ ps.

3.3.2 Raman

In the Raman spectra only the E_2^2 phonon mode is clearly visible (Fig 3.11), whereas the other Raman active modes, E_2^1 and A_1(LO), are not visible in $z(yy)\bar{z}$ backscattering configuration due to the quasi-polycrystalline nature of AlN. Thus only the E_2^2 mode was analyzed. In order to analyze the other phonon modes, the backscattering configurations from the film cross-section have to be employed (Tab. 2.2). This turned out extremely difficult to perform on sub-micron thick films as the area of signal accumulation is very small.

The observed E_2^2 phonon mode red-shift with increasing film thickness as the other modes observed in FTIR (Fig. 3.10). This shift is linear with in-plane stress. The advantage of Raman spectroscopy over FTIR is that there is no limitation for thicker films, the thicker the film the more intense phonon peak is obtained. The estimated E_2^2 phonon mode lifetime values are also strongly reduced as compared to single crystal (Fig. 3.12, Tab. 3.3), thus the same reason as for the E_1 phonon mode can be attributed, i.e. that the displacement of vibrating atoms is perturbed by the grain boundaries of AlN (Fig. 2.14 (b)). The lifetime governed by anharmonic decay and background defect scattering of the E_2^2 phonon mode in AlN sputtered using N_2 plasma on Si and Al_2O_3 substrates are evaluated to be (0.71 ± 0.05) ps and (0.88 ± 0.05) ps, respectively. Here, as in the analysis of XRD RC data, the conclusion is that AlN on sapphire substrate is of better quality, i.e. possesses lower density of defects. The phonon lifetimes in AlN films sputtered using Ar:N_2 plasma on Si and Cr surfaces are evaluated to be (0.67 ± 0.05) ps and (0.39 ± 0.04) ps, respectively. The change in deposition process did not influence much the quality of the AlN layer as it was seen in Section 3.2.1 (Fig. 3.12 (a)). However, the AlN thin film deposition on Cr layer is of much worse quality as on Si or Al_2O_3. This could be explained by the fact that sputtered Cr is polycrystalline and has a rough surface ($\rho \approx 8$ nm). Moreover, in the Raman spectra of the thickest AlN film on Cr the A_1(TO) mode was visible (Fig. 3.13). The A_1(TO) mode is only visible in $x(zz)\bar{x}$ and $x(yy)\bar{x}$ backscat-

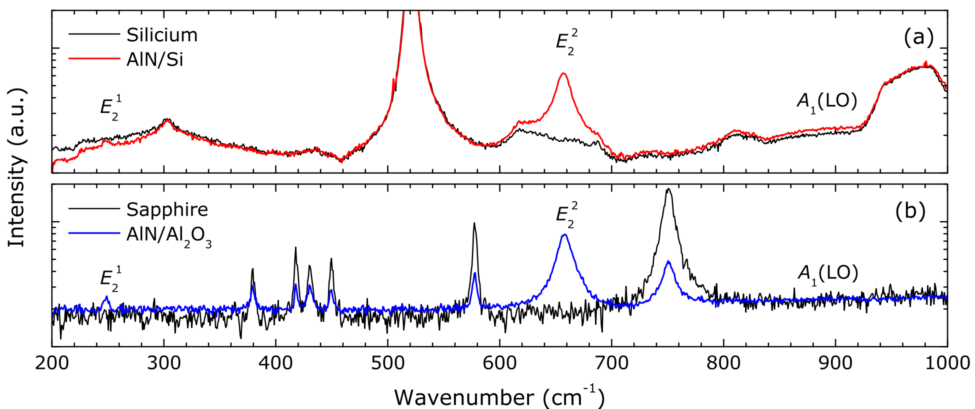

Figure 3.11: Raman spectra of a 200 nm thick AlN film deposited using N_2 plasma on Si (a) and Al_2O_3 (b) measured at $z(yy)\bar{z}$ backscattering configuration.

tering configurations. This fact evidences that there are AlN grains whose c-axis lies perpendicular to the surface normal. This time a Bragg diffraction peak near 32.7° in XRD θ-2θ scan could be attributed to AlN(100), although the possibility remains that it is the forbidden Si(200) peak.

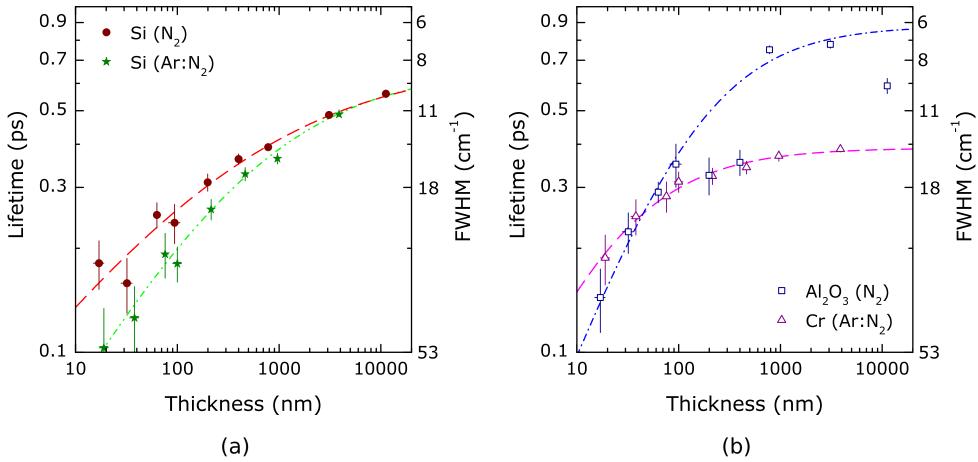

Figure 3.12: E_2^2 phonon mode lifetimes versus AlN films thickness as determined from the Raman line width. (a) AlN on Si(100) deposited using N_2 plasma (circles) and Ar:N_2 plasma (stars). (b) AlN on Al_2O_3(0001) (squares) and on a Cr interlayer on Si (triangles). The dashed lines are guides for the eyes.

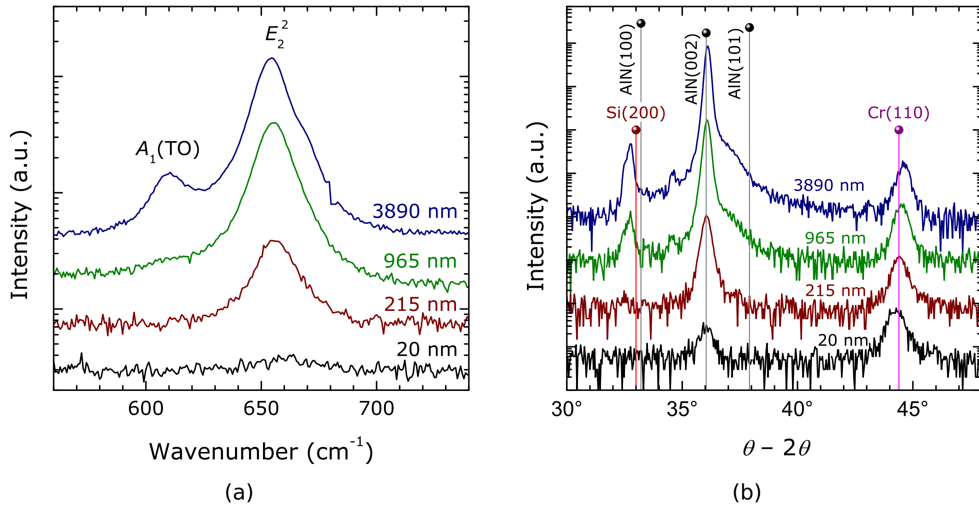

Figure 3.13: Raman spectra measured at $z(yy)\bar{z}$ backscattering configuration (a) and XRD θ-2θ scan (b) of AlN film deposited using Ar:N_2 plasma on Cr/Si. The curves are shifted for clarity. XRD patterns are measured using a focusing beam setup with a Siemens D5000 diffractometer.

Chapter 4

Route towards applications

In this Chapter the possible routes and obstacles for AlN to become a part of a device will be covered. The first issue that AlN encounters is its deposition on metal contacts, which is one of the ways to exploit the piezoelectric properties of AlN. The second encounter comes when one wants to combine AlN and diamond. The possibilities of AlN on NCD and NCD on AlN will be discussed in the second part of this chapter.

4.1 AlN on metals

In most cases, when AlN is used in devices as piezoelectric material, the electrical field has to be applied on AlN, thus electrical contacts are needed. There are two possibilities: (i) metal deposition on AlN or (ii) AlN sputtering on the metal contact. This Section will give a short overview of the second case, i.e. AlN deposition on different metals interlayers on Si: Al, Ti, V, Cr, Zr, Nb, Mo, Ta, and W. Additionally, the variation of the deposition power on the properties of AlN, sputtered on Al, Cr, Ta, and W, will be analyzed.

The metal thin films were sputtered on Si(100) substrates (sample series $\mathcal{S}_{\mathrm{Metal}}$, Tab. 2.1) and their surface roughnesses were determined by AFM. Later, AlN films were deposited ($\mathcal{S}_{100\%}$) and their XRD RC peaks were analyzed (Fig. 4.1). One of the worst quality of AlN film is obtained on Al layers, although Al is most widely used as contact metal due to its low price. This can be explained by the high roughness of the Al layer. Therefore, to use Al as contacts the deposition conditions should be optimized. Chromium, which is also often used in device fabrication, showed better

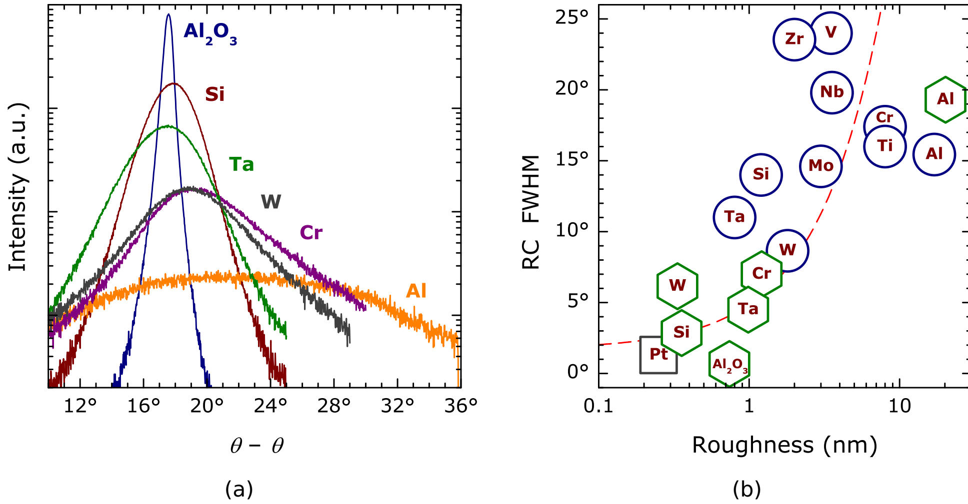

Figure 4.1: (a) XRD RC of AlN ($\mathcal{S}_{Power,600W}$) deposited on sputtered metal interlayer, Si(100) and Al_2O_3(0001). (b) FWHM of XRD RC peaks versus substrate surface roughness of $\mathcal{S}_{100\%}$ (circles) and $\mathcal{S}_{Power,600W}$ (hexagons) AlN sample series (Tab. 2.1). The result of AlN on Pt(111) is taken from Reference [40]. The dashed line is a linear dependence of the FWHM on surface roughness taken from Ref. [110].

results than aluminum. Artieda *et al.* have demonstrated that the FWHM of the RC has a linear dependence on the surface roughness of amorphous Si [110]. Thus, one could speculate that for those metals on which AlN is achieved with the FWHM of RC below the dashed line in Figure 4.1 are more suitable that those which are achieved above the line. However, it remains difficult to assess the influence of the metals on the FWHM of the RC. The only conclusion, that can be repeated, is that the smallest width of the RC peak is achieved on the smoothest metal surfaces.

Another approach to compare the results of AlN on different metals is to employ Raman spectroscopy (Fig. 4.2). By analyzing the E_2^2 mode phonon peak shift, a conclusion on the average stress in the films can be made (Fig. 4.2 (a)). An almost stress-free AlN film is achieved on Al layers ($\mathcal{S}_{Power}$) although the FWHM of the RC was one of the broadest. Rather a small in-plane stress is detected in AlN on Al_2O_3(0001) ($\mathcal{S}_{Power}$) and Cr, Nb, V from the sample series $\mathcal{S}_{100\%}$. Once more, when comparing the results obtained on different metals, which are polycrystalline, one can notice a link with the surface roughness. AlN on Al ($\mathcal{S}_{Power}$), which had the roughest surface, showed the smallest stress in the film, contrary to AlN on Al from $\mathcal{S}_{100\%}$ sample series. Then one can note two groups of samples with diferent tendencies: (i) increasing compressive and (ii) increasing tensile in-plane stress as the surface roughness decreases. When the surface becomes smoother the inclination of columnar grains and in turn the gaps between them gets smaller. Then the behavior of the compressive stress with different surface roughness can be explain by the stress relaxation through the grain boundaries, the larger the gaps that are present between the AlN grains the smaller the stress is. The behavior of the tensile stress, could be explained by inclined grains,

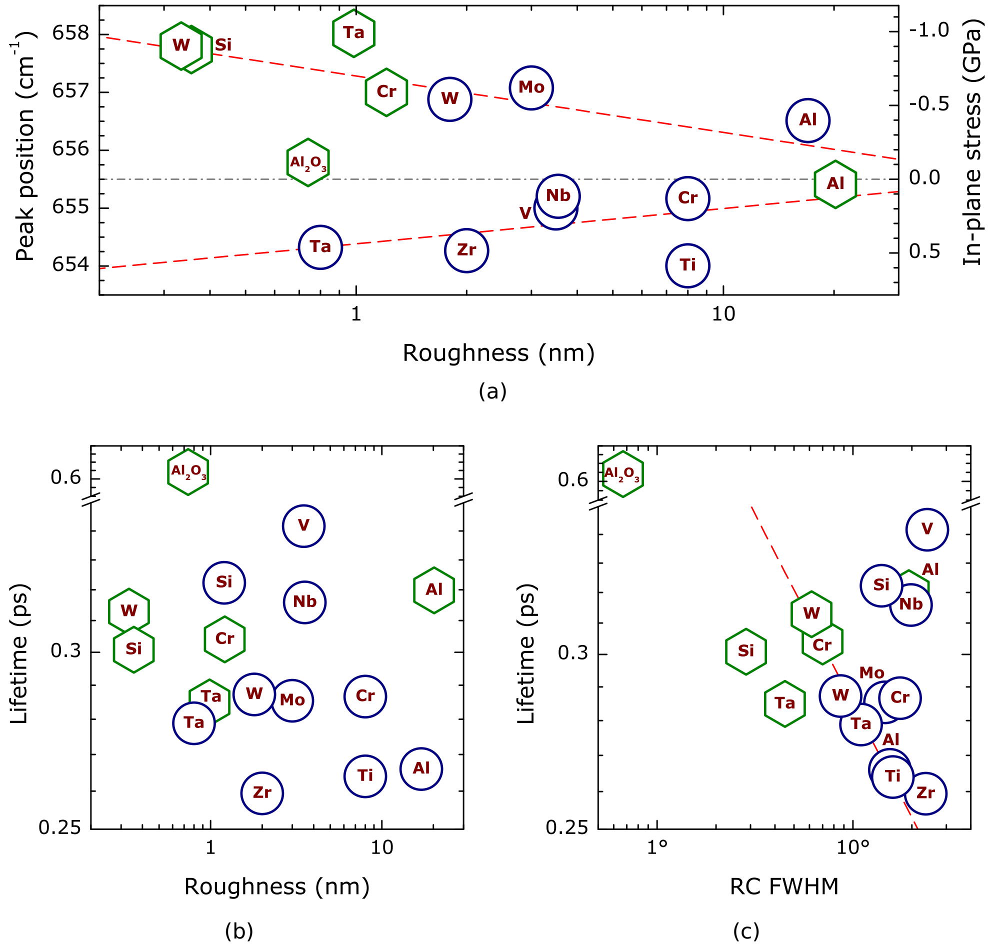

Figure 4.2: E_2^2 phonon mode peak position (a) and lifetime (b) versus substrate surface roughness of $\mathcal{S}_{100\%}$ (circles) and $\mathcal{S}_{\text{Power,600W}}$ (hexagons) AlN sample series (Tab. 2.1). (c) Lifetime versus FWHM of RC. In graph (a) the dash-dotted line represents the stress-free phonon peak position, 655.5 cm^{-1}, the phonon frequency shift from this value is converted into the in-plane stress (right hand side scale) using the phonon frequency linear shift per unit stress (2.55 cm^{-1}/GPa, Ref. [93]). The dashed lines are guides for the eyes.

the more they incline the less space is left for the other grains. However, in order to draw such conclusions a more sophisticated analysis, e.g. transmission electron microscopy (TEM), is required.

The peak width of the Raman peak and so the lifetime of the E_2^2 mode phonon does not show a strong correlation (Fig. 4.2 (b)). The lifetime is inversely proportional to the density of defects[1], $\tau_d \propto \varrho_d^{-1}$. If the lifetime is plotted against the FWHM of the RC (Fig. 4.2 (c)), which is influenced by the dislocation density and the struc-

[1]Defects include: point, line and planar defects.

tural features[2] [104], one can envisage the trend of the lifetime decrease, i.e. the increase of the defect density, with the broadening of the RC. This is not surprising, as the lifetime is also dependent on dislocation density, but independent of the structural features. Thus, one could speculate that the samples laying on the dashed line (Fig. 4.2 (c)) differ only in the number of dislocations, although a sophisticated analysis of dislocation density connection with the FWHM of the RC is needed [104].

A further study is made on the sample series $\mathcal{S}_{\text{Power}}$ (Tab. 2.1) and the features of Raman peaks were investigated (Fig. 4.3). One of the observations is that the stress tends to get smaller when AlN is deposited at higher power on Si, W and Al_2O_3. This could be due to the fact that better quality is obtained at higher deposition power (Fig. 4.4 (a)). Moreover, these substrates had smooth surfaces, $\rho < 1$ nm. In case of Al, Cr and Ta, $\rho \geq 1$ nm, no substantial stress variation is noticed above 300 W. At the lowest deposition power (200 W) AlN films on all metal layers showed significant deviation in stress values. The tensile in-plane stress (+1.2 GPa) in AlN films deposited under 200 W power on Al layer and later reduction with power can be explained by the model of extra atoms insertion into the grain boundary [39, 91]. When the target power is increased N_2 ions are accelerated faster towards the target and so more energetically AlN compounds reach the surface of a sample. This means they will show a higher jump rate from site to site on the surface, thus a higher flow rate into the grain boundary that shifts the film's stress towards compression. In case of other metals (Cr, Ta, W) the compressive stress appears to be much higher at 200 W deposition power. This cannot be explained by the same model as for the AlN on Al case. Rather the mixed orientation, (002) and (103), of AlN films that appear under these conditions [37] could be the cause of high compressive in-plane stress.

By analyzing the width of the Raman peak of the E_2^2 mode phonon one can immediately notice the supreme lifetime in AlN on Al_2O_3(0001) substrates, which is at least twice longer when compared to the other substrates. This is not unexpected as the narrowest FWHM of the RC was obtained on this substrate. However, the phonon lifetime in AlN on other substrates does not differ significantly, i.e. not as much as the FWHM of the RC. This implies that the density of defects is more or less the same in these films. By analyzing the deposition power influence, in all cases except Cr, the phonon lifetime increases with increasing power. The increase of lifetime stops at 500 W and stays constant for AlN on Si, Al and Al_2O_3, while for Ta and W it keeps increasing. For Cr it tends to decrease for power higher than 600 W. There is no correlation between such behavior of phonon lifetimes and the roughness of the substrate surface. If, again, the lifetime is presented as a function of the FWHM of the RC (Fig. 4.4 (b)), one gets a linear relationship in a double-log scale graph. This time, the substrate is the same, i.e. Si, thus the factor for the grain tilt, i.e. the surface roughness, is eliminated and one has a stronger argument that the increase in the phonon lifetime is due to the reduction of dislocation density. However, the TEM analysis is essential for confirmation that the grain tilt does not change with increasing deposition power.

[2] Heterogeneous strain, correlation lengths normal and parallel to the substrate surface, and the degree of mosaicity, i.e. a measure of the long-range disorder, expressed by the tilt and twist angles.

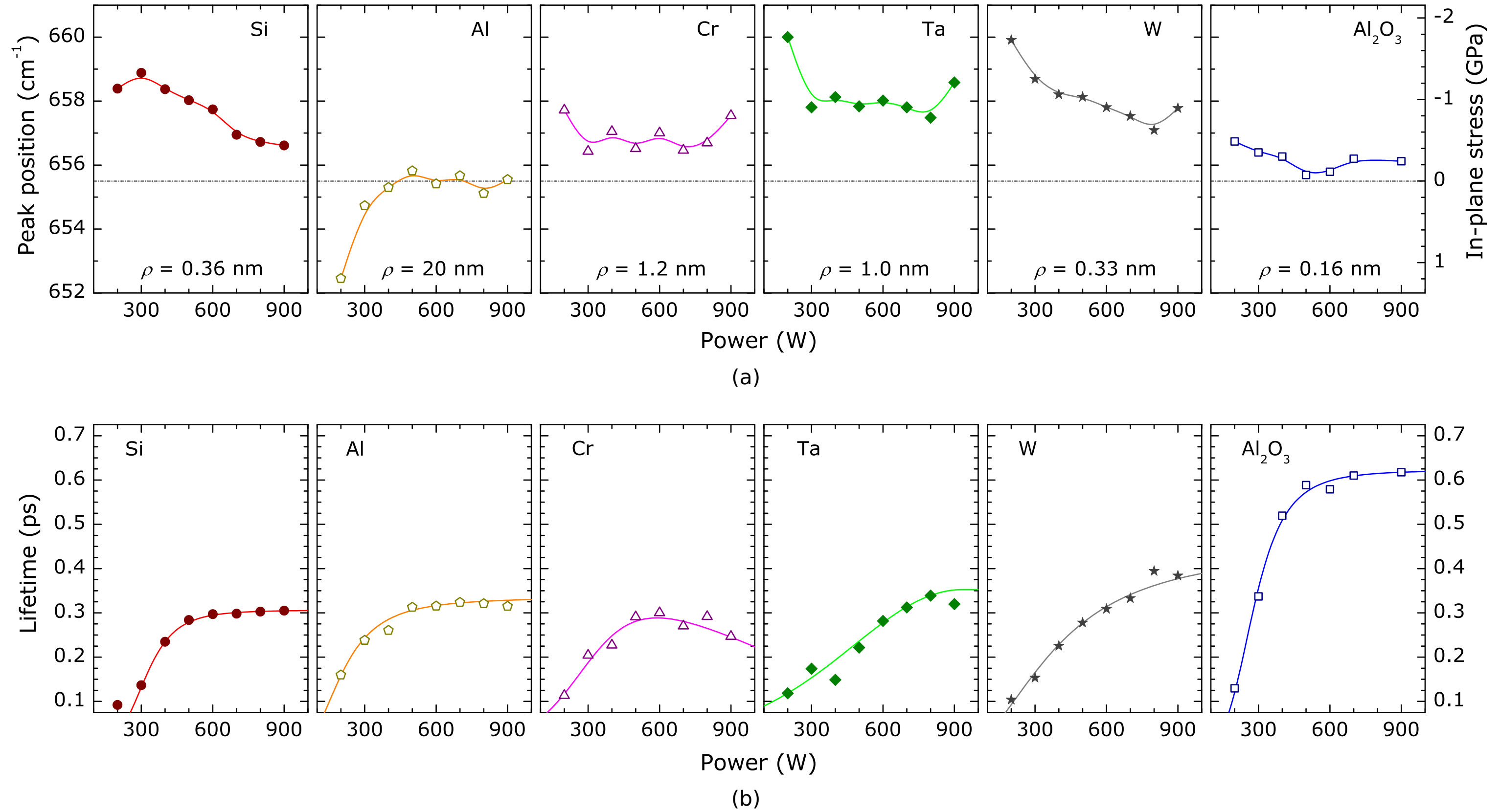

Figure 4.3: (a) E_2^2 phonon mode peak position of 500 nm thick AlN deposited on Si(100), sputtered metal layer (Al, Cr, Ta, W) and Al_2O_3(0001) under various target supply powers ($\mathcal{S}_{\text{Power}}$, Tab. 2.1). The dashed line represents the stress-free phonon peak position, 655.5 cm^{-1}. (b) Lifetime of E_2^2 mode phonon as determined from FWHM of the Raman peak. The lines are guides for the eyes.

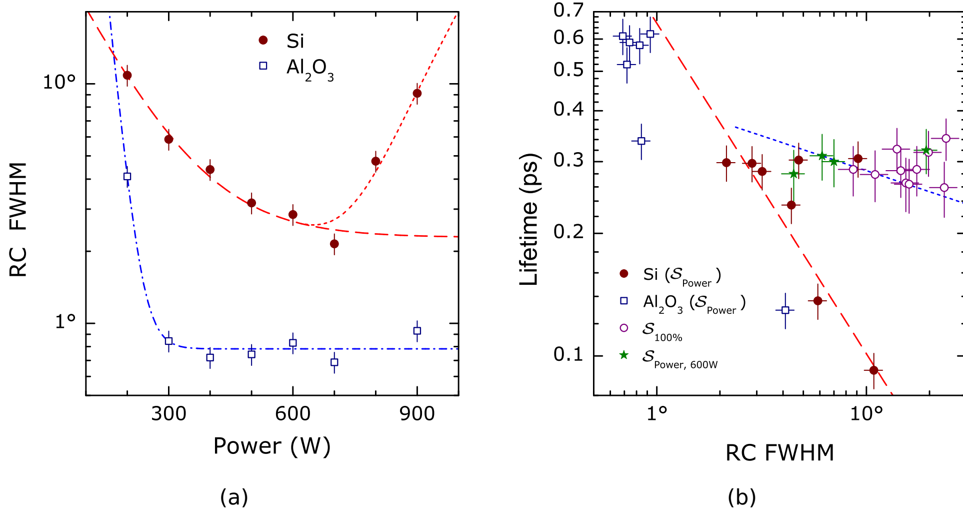

Figure 4.4: (a) RC peak FWHM of (0002) AlN sputtered on Si (full circles) and Al_2O_3 (open squares) versus target supply powers ($\mathcal{S}_{\text{Power}}$, Tab. 2.1). (b) Lifetime of E_2^2 phonon mode versus FWHM of RC, open circles and full stars denote $\mathcal{S}_{100\%}$ and $\mathcal{S}_{\text{Power,600W}}$ sample series, respectively. The lines are guides for the eyes.

4.2 AlN & Diamond

In this Section the AlN on diamond combination will be analyzed. The main focus is put on how to achieve a high seeding density of nanodiamond particles on AlN layers and subsequent pinhole-free NCD film growth.

4.2.1 AlN on NCD

The easiest approach to fabricate AlN/NCD heterostructures is to sputter AlN on NCD film (Fig. 4.5). However, in this case the surface roughness of NCD film is unacceptable. If surface acoustic wave (SAW) device is fabricated on such surfaces, the excited SAWs will experience extreme scattering while propagating. Thus the SAW device will simply not work. In order to smoothen the surface of the NCD film expensive and sophisticated polishing of NCD surfaces is needed. In the case of thiner NCD films the surface is less but still rough. However, the polishing of > 100 nm thick NCD films is extremely difficult.

4.2.2 NCD on AlN

The nanodiamond (ND) seeding and growth of NCD layers on AlN is not straightforward. If AlN is seeded using the ND colloidal seeding process and exposed to

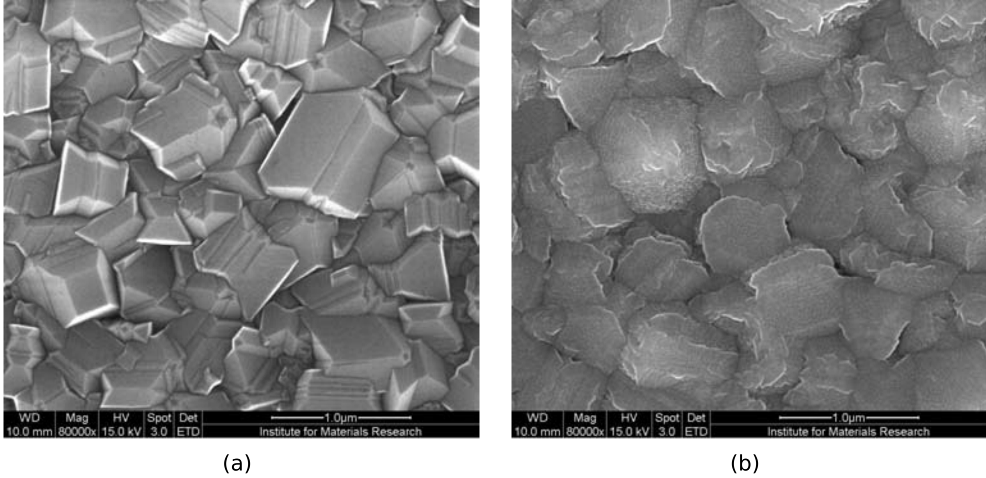

(a) (b)

Figure 4.5: (a) NCD film, 1000 nm thick, grown on Si(100) by MW PE CVD. (b) AlN, 1000 nm thick, sputtered on NCD.

a conventional CH_4 and H_2 plasma, the grown NCD film appears to be inhomogeneous (Fig. 4.6). This is due to the hydrophobic nature of AlN and consequent low seeding density on such surface. In order to achieve a high and homogeneous seeding density the surface of AlN needs to be modified in a way that the adhesion force between ND particle and the surface is enhanced.

A simple experiment can show that ND particles adhere to the surface by the Van der Waals (VdW) force; one has to increase the roughness of silicon surfaces by Ar plasma pretreatment and seed with NDs after. The achieved density of ND seeds varied with the surface roughness (Fig. 4.7). Argon plasma pretreatment is adequate for ion milling, thus the native silicon oxide layer of 2 nm is removed approximately after 10 s (etching rate 39 nm/min [111]). However, upon an exposure to air and dipping into the seeding water based colloid, a native oxide layer of around 2 Å is formed [112]. Plasma exposures of different timing cause different surface roughness. If ND particles adhere to the surface by the VdW force, the seeding density should be proportional to the this force $\mathcal{F}_{\mathrm{VdW}}$ that acts between the ND particle and the rough surface. Rabinovich developed a model that quantitatively predicts adhesion forces between a particle and the rough surface [113]:

$$\mathcal{F}_{\mathrm{VdW}} = \frac{\mathcal{A}_{\mathrm{H}}\tilde{r}}{6d_0}\left[\frac{1}{1+\tilde{r}/(1.48\rho)} + \frac{1}{(1+1.48\rho/d_0)^2}\right], \tag{4.1}$$

where $\mathcal{A}_{\mathrm{H}}$ is the Hamaker coefficient, that depends on the material properties and intervening medium, $\tilde{r}$ is the radius of the adhering particle, d_0 is the distance of closest approach between a surface and ND particle (≈ 0.3 nm), and ρ is the roughness of the surface. The average radius of a ND particle ≈ 3 nm (Fig. 2.20). The curve according to Equation (4.1) drawn through the experimental points proofs that

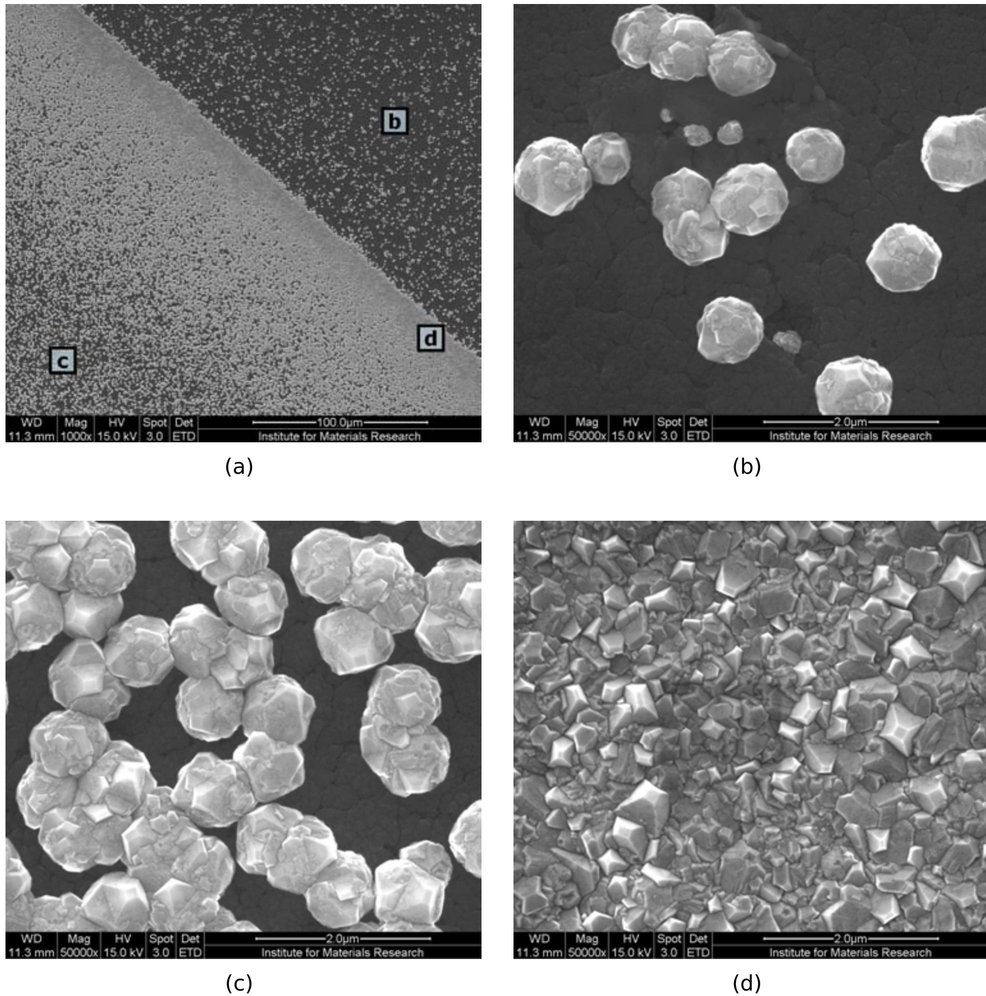

Figure 4.6: NCD grown on as deposited AlN. The NCD film coverage varied from very low (b) to very high (d) indicating inhomogeneous seeding density of ND prior the growth of NCD film.

ND adhere to silicon surfaces through the Van der Waals interaction.

The surface treatment of Si with N_2 and O_2 plasmas works as nitriding and oxidation, respectively. Thus, as no etching of silicon occurs the surface does not roughens much after these exposures. However, surfaces of Si_3N_4 and SiO_2 have different interaction strengths with ND particles, i.e. different Hamaker constants. Thus, one gets different seeding densities as compared to the pure Si case.

After H_2 and CF_4 plasma pretreatment the native silicon oxide is removed due to reactive ion etching and the silicon surface is hydrogen or fluorine terminated, respectively. The H or F atoms present at the surface induce negative charge on the surface and this yields electrostatic interaction between adhering ND particles, which

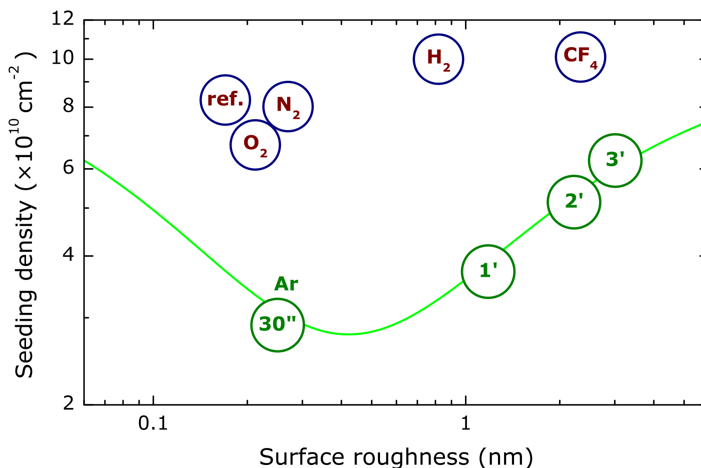

Figure 4.7: Seeding density versus the surface roughness after various plasma pretreatments (Ar, CF_4, H_2, N_2, and O_2) and various pretreatment times in case of Ar. A reference sample (ref.) was only cleaned with SPM/APM. The line represents the seeding density proportional to the VdW force (Eq. (4.1)).

have positive zeta-potential, and the surface [114]. Thus the seeding efficiency is enhanced and reaches 10^{11} cm^{-2}.

In order to achieve a high seeding density on AlN and homogeneous NCD film coverage, the surface of AlN was exposed to different plasmas: Ar, CF_4, H_2, N_2, and O_2. After plasma pretreatments the surface charge, groups and roughness are changed. Hence, the interaction force between ND particle and surface is changed. The wetting properties after the plasma exposure were studied (Fig. 4.8). Here it should be noted, that 1,2-ethanediol was used for contact angle measurements. After Ar, N_2 and O_2 pretreatment the surface wetting properties have not changed much, whereas after CF_4 and H_2 the surface of AlN became hydrophilic. The determined surface roughness after the pretreatments showed that there is no pronounced correlation between contact angle value and roughness (Fig. 4.9 (a)). The interesting effect is observed that the surface of AlN became smother after N_2 treatment. This could be practical for AlN smoothing when preparing surface acoustic wave devices.

After the ND seeding the density of nucleation sites was calculated (Fig. 4.9 (b)). A strong dependency between the contact angle and seed density is observed. In case of Ar ion milling, nitriding and oxidation of the AlN surface there is not much change in measured contact angle as well as achieved ND seeding density. However, after CF_4 and H_2 plasma the surface became hydrophilic and the obtained seeding density increased almost by four orders of magnitude in comparison with untreated AlN surface. As the roughness of AlN surface has not changed a lot after the plasma pretreatments, the seeding density enhancement is due to functional groups present on the AlN surface. Hydrogen and fluorine atoms on the surface accumulate negative charge and by electrostatic force the ND particles are attracted to the surface.

After the seeding of the AlN surface, the growth of NCD films followed and the results

are presented in Figures 4.10 and 4.11. In case of high nucleation density the pinhole-free NCD layers of 100 nm is observed, whereas in case of low seeding density only separate diamond grains are present.

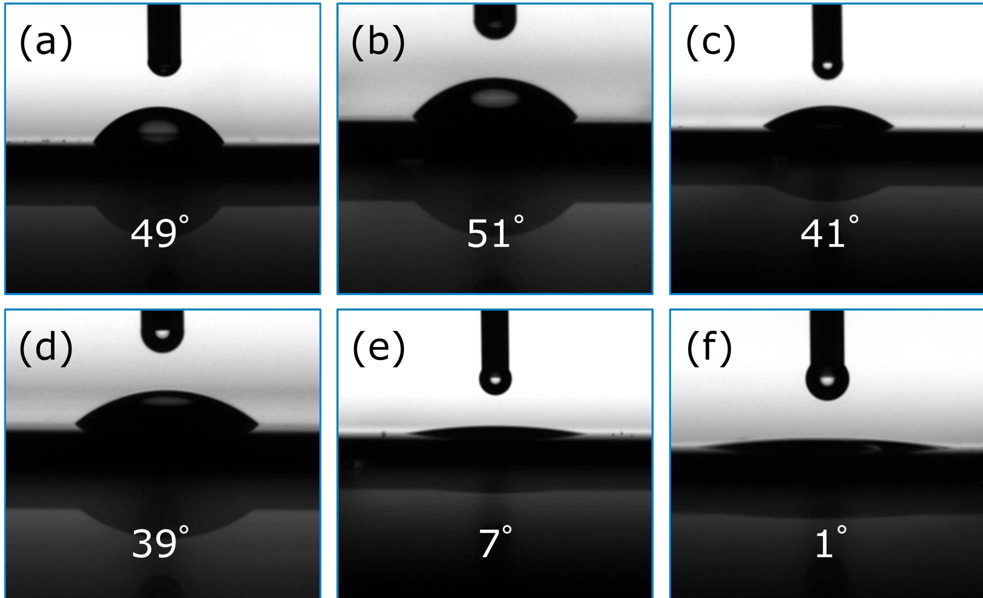

Figure 4.8: Wetting properties of AlN surface after ethanol cleaning (a) and after plasma pretreatment: (b) Ar, (c) N_2, (d) O_2, (e) CF_4, (f) H_2. 1,2-ethanediol was used as a test liquid.

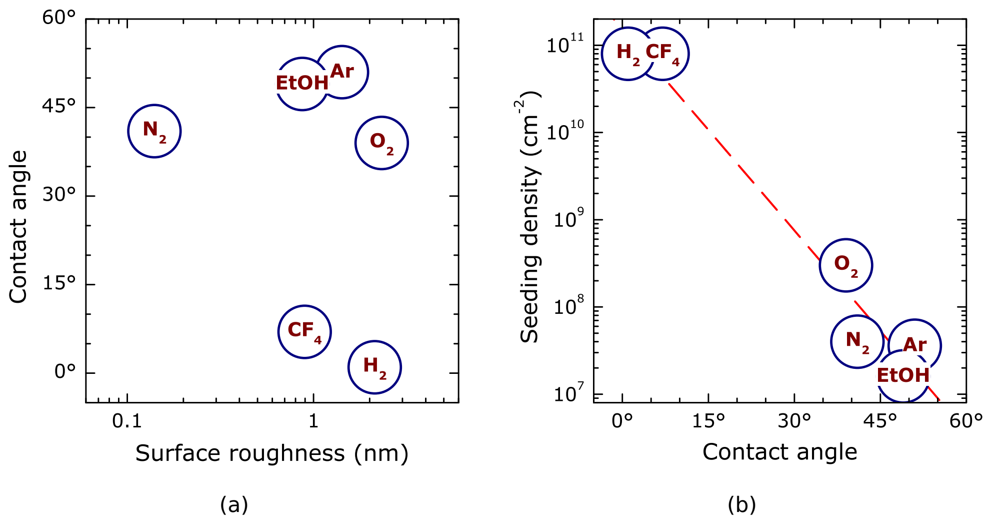

Figure 4.9: Contact angle of 1,2-ethanediol on AlN surface versus surface roughness (a) and achieved density of ND versus wetting angle after ethanol (EtOH) cleaning and after plasma pretreatment: Ar, N_2, O_2, CF_4, H_2. The line is guide for the eyes.

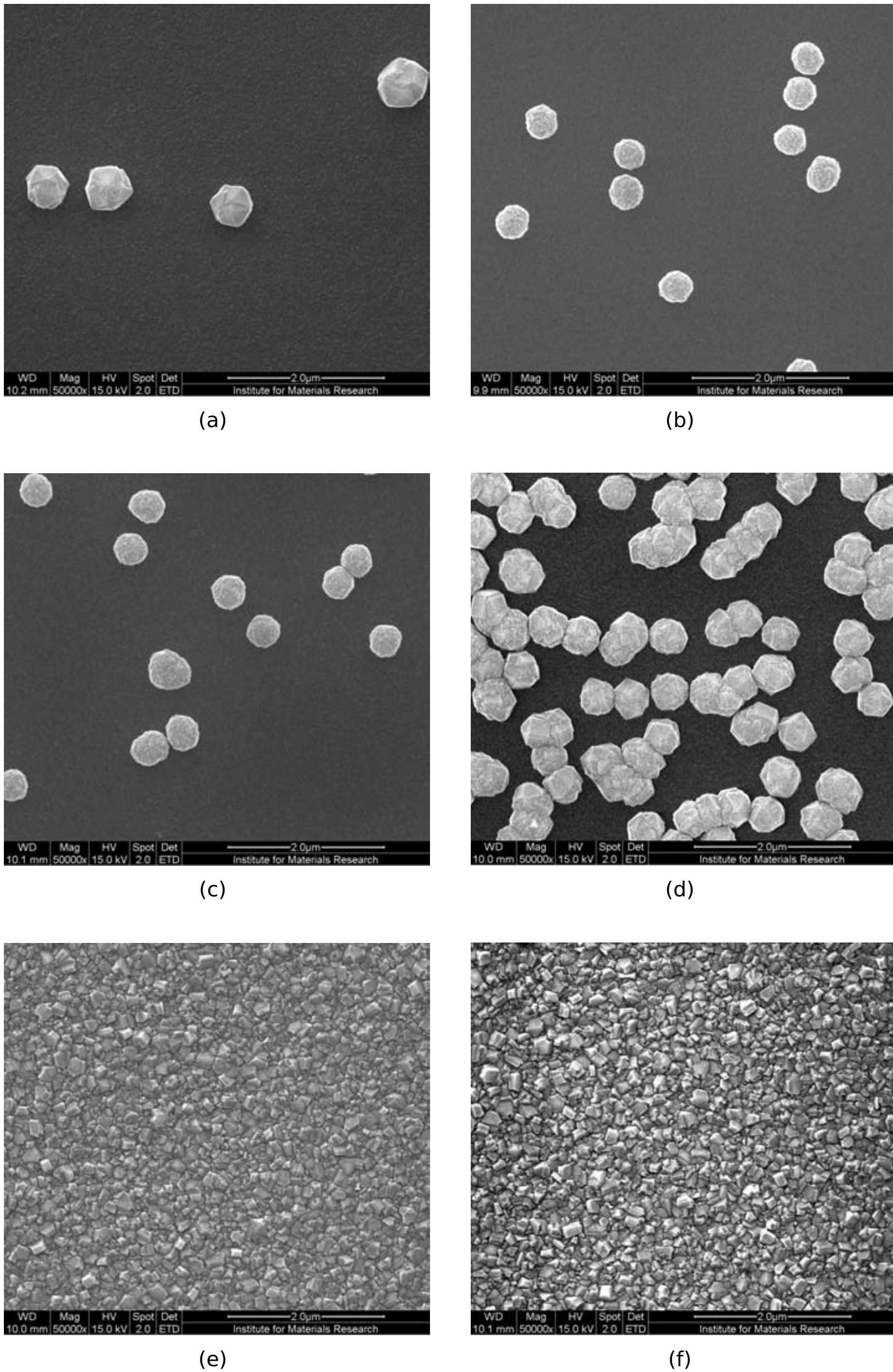

Figure 4.10: NCD growth on AlN surface after ethanol cleaning (a) and after plasma pre-treatment: (b) Ar, (c) N_2, (d) O_2, (e) CF_4, (f) H_2.

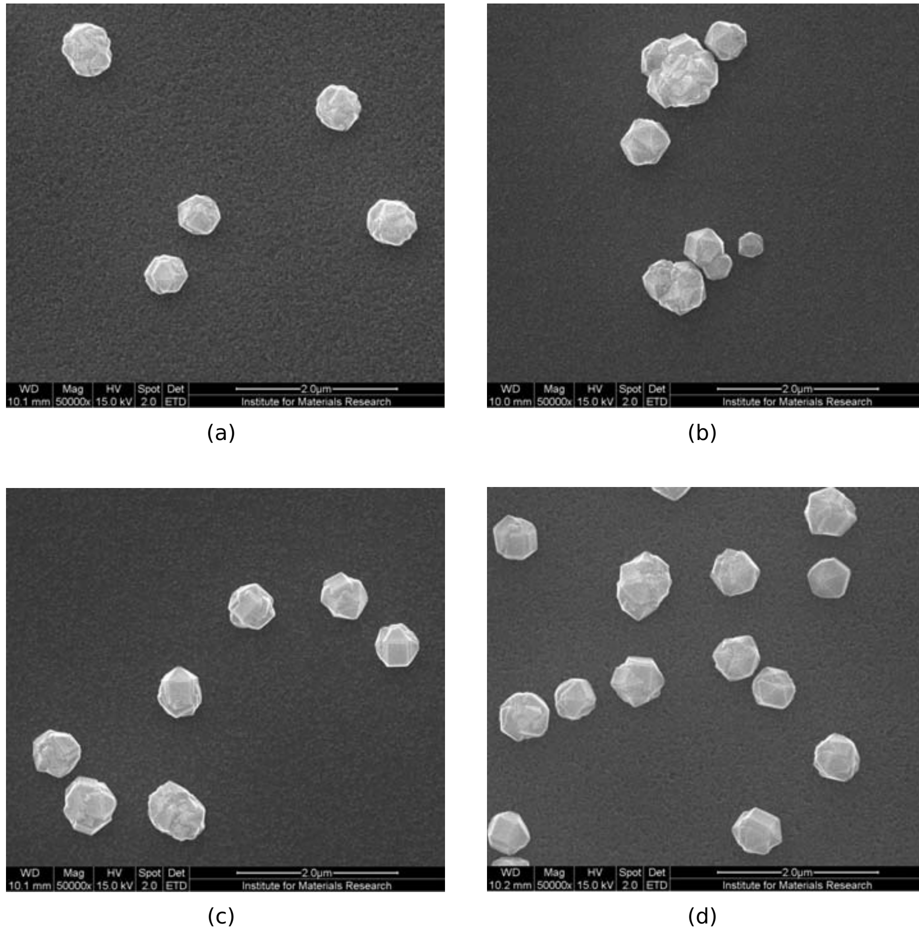

Figure 4.11: NCD growth on AlN surface after acidic surface cleaning: (a) SPM, (b) HCl, (c) HNO_3, (d) H_3PO_4.

Chapter 5

Conclusions & Outlook

Aluminum nitride films of different thickness, ranging from 17 nm to 3900 nm, were deposited by DC-pulsed reactive magnetron sputtering on silicon (100), sapphire (0001) substrates, and various metal interlayers. In case of sputtering using a nitrogen plasma, it is shown that the average residual in-plane stress is compressive and substrate independent up to 150 nm film thickness. For thicker AlN films on Si substrates the in-plane stress stays compressive, while the transition from compression to tension occurs near 1000 nm for AlN films on Al_2O_3 substrates. Additionally, a stepwise thickness reduction of a 1500 nm thick AlN film on Si by wet chemical etching has proven that a stress gradient exists. A non-linear fit of experimental data points indicates that this stress gradient is higher in AlN films on Al_2O_3 than on Si substrates, which in turn allows the transition from compression to tension to occur. This observation is linked to better quality of the AlN films on Al_2O_3 as indicated by XRD rocking curve analysis. For comparison, a series of AlN films was deposited on Si substrates using Ar:N_2 plasma. This change in deposition conditions shifted the in-plane stress values towards tensile stress, retaining the same degree of crystallite disorientation as well as the same stress gradient.

X-ray diffraction analysis of strain along the *c*-axis in the AlN films has shown linear behavior with respect to the in-plane stress indicating that AlN films are biaxially strained and that the residual in-plane stress is the main mechanism governing the variation of the lattice constants. The investigation of the XRD rocking curves has confirmed the high quality of AlN layers on *c*-cut sapphire substrates for each sample thickness, while on Si and Cr/Si the quality improves for thicker layers. This quality improvement can be attributed to a decrease of dislocation density, which prevents a high stress gradient to appear. The AlN surface roughens with increasing thickness independently of the substrate material and the deposition conditions that were used. Finally, the density of grain boundaries has only a minor effect on the observed in-plane stress behavior.

The optical phonons were investigated by Fourier transform infrared spectroscopy in AlN on Si deposited using nitrogen plasma. The frequencies and lifetimes were calculated based on the factorized model of a damped oscillator. The stress-free phonon frequencies of $(670 \pm 1)\,\mathrm{cm}^{-1}$ and $(887 \pm 1)\,\mathrm{cm}^{-1}$, as well as decay times of at least (0.29 ± 0.03) ps and (0.58 ± 0.05) ps were deduced for the E_1(TO) and A_1(LO) phonon modes, respectively. Additionally, E_2^2 phonon modes were investigated by the Raman scattering technique and the same trend was observed. The stress-free phonon frequency $(655.5 \pm 0.5)\,\mathrm{cm}^{-1}$, and a lifetime of at least (0.71 ± 0.05) ps were determined. As a comparison, the phonon lifetime in AlN films on Al_2O_3 was (0.88 ± 0.05) ps. The lifetimes clearly become longer for thicker films as the quality of the films improves. The A_1(LO) phonon mode is less than the E_1(TO) phonon mode affected by film imperfections, which is attributed to the stronger scattering effect of grain boundaries on the latter.

The film deposition on different metal interlayers showed that surface smoothness is essential for achieving high quality films, although the tendency of lower in-plane stress on rougher surfaces is observed. The investigation of the E_2^2 mode phonon revealed that the lifetime of the phonon correlates with the width of the rocking curve as both quantities depend on a common factor, i.e. the density of dislocations. However, to confirm the main role of dislocations and differentiate the influence of the other type of defects, heterogeneous strain, correlation lengths, and the degree of mosaicity, a more sophisticated analysis is required, e.g. transmission electron microscopy.

On the way of producing diamond films on AlN layers, it is shown that surface treatments altering the charge, chemical groups and roughness of the surface are important for nanodiamond seeding. The ND particles used for seeding adhere to the surface by the Van der Waals and electrostatic forces. Therefore, after an appropriate surface treatment of silicon and aluminum nitride with a plasma it is possible to successfully increase the nucleation density. The intended Si surface roughening by Ar plasma and subsequent seeding showed that ND adhere due to VdW forces. The surface chemical group modification by H_2 and CF_4 plasma pretreatment notably enhanced the seeding density on Si and AlN surfaces, reaching 10^{11} cm^2 of ND particles.

ND seeding and in turn NCD layer growth directly on AlN has proven to be very difficult due to its hydrophobic surface properties, hampering seeding and subsequent growth. In a similar way as silicon treatment, the treatment of the AlN surface with H_2 and CF_4 plasma enhanced the ND seeding, which led to a sufficiently high nucleation density and allowed to form a pinhole-free NCD layer on top of this piezoelectric material. Moreover, the hydrogenation and fluorination made the AlN surface hydrophilic.

To support the observations of change in the film properties with thickness, deposition power and substrate's surface roughness variation, a detailed analysis of the film structure by TEM is essential. Also a more sophisticated analysis by the XRD technique is required to determine the density of dislocations in the films. Concerning the FTIR modeling, the stress gradient in the films could be incorporated into the calculations in order to check its influence on the spectra. This is particularly needed

for AlN films on sapphire, as there high stress gradients are observed. Moreover, the inclination of the optic axis should be taken into account for analysis of the films with high c-axis of-angle, e.g. AlN on Al. Finally, concerning the adherence of ND particles on AlN (and Si) further experiments have to be performed in order to confirm the electrostatic nature of the ND seeding enhancement on AlN (and Si) surfaces, e.g. by means of X-ray photoelectron spectroscopy.

Bibliography

[1] P. J. Steinhardt, N. Turok, A cyclic model of the universe, Science 296 (5572) (2002) 1436 – 1439.

[2] P. J. Mohr, B. N. Taylor, CODATA recommended values of the fundamental physical constants: 2002, Science 77 (1) (2005) 1 – 107.

[3] S. Strite, H. Morkoç, GaN, AlN, and InN: A review, J. Vac. Sci. Technol. B 10 (4) (1992) 1237 – 1266.

[4] H. Morkoç, S. Strite, G. B. Gao, M. E. Lin, B. Sverdlov, M. Burns, Large-band-gap SiC, III-V nitride, and II-VI ZnSe-based semiconductor device technologies, J. Appl. Phys. 76 (3) (1994) 1363 – 1398.

[5] I. Vurgaftman, J. R. Meyer, L. R. Ram-Mohan, Band parameters for III-V compound semiconductors and their alloys, J. Appl. Phys. 89 (11) (2001) 5815 – 5875.

[6] V. Cimalla, J. Pezoldt, O. Ambacher, Group III nitride and SiC based MEMS and NEMS: materials properties, technology and applications, J. Phys. D: Appl. Phys. 40 (20) (2007) 6386 – 6434.

[7] M. E. Levinshtein, S. L. Rumyantsev, M. S. Shur, Properties of advanced semiconductor materials: GaN, AlN, InN, BN, SiC, SiGe, Wiley-Interscience, 2001.

[8] F. A. Ponce, D. P. Bour, Nitride-based semiconductors for blue and green light-emitting devices, Nature 386 (6623) (1997) 351 – 359.

[9] C. R. Miskys, J. A. Garrido, C. E. Nebel, M. Hermann, O. Ambacher, M. Eickhoff, M. Stutzmann, AlN/diamond heterojunction diodes, Appl. Phys. Lett. 82 (2) (2003) 290 – 292.

[10] Y. Taniyasu, M. Kasu, T. Makimoto, An aluminium nitride light-emitting diode with a wavelength of 210 nanometres, Nature 441 (2006) 325 – 328.

[11] M. S. Shur, R. Gaska, Deep-Ultraviolet Light-Emitting Diodes, IEEE Trans. Electron Devices 57 (1) (2009) 12 – 25.

[12] K. Hirama, Y. Taniyasu, M. Kasu, Electroluminescence and capacitance-voltage characteristics of single-crystal n-type AlN (0001)/p-type diamond (111) heterojunction diodes, Appl. Phys. Lett. 98 (1) (2011) 011908.

[13] A. Žukauskas, M. S. Shur, R. Gaska, Introduction to solid-state lighting, Wiley-Interscience, 2002.

[14] T. Y. Sheng, Z. Q. Yu, G. J. Collins, Disk hydrogen plasma assisted chemical vapor deposition of aluminum nitride, Appl. Phys. Lett. 52 (7) (1988) 576 – 578.

[15] H. Fritze, High-temperature piezoelectric crystals and devices, J. Electroceram. 26 (1 - 4) (2011) 122 – 161.

[16] Y. Ooishi, K. Kishi, M. Akiyama, H. Noma, I. Ohshima, High temperature and high pressure response of aluminum nitride thin films prepared on inconel substrates, J. Ceram. Soc. Jpn. 114 (1327) (2006) 296 – 298.

[17] L. La Spina, E. Iborra, H. Schellevis, M. Clement, J. Olivares, L. K. Nanver, Aluminum nitride for heatspreading in RF IC's, Solid-State Electron. 52 (9) (2008) 1359 – 1363.

[18] C.-M. Lin, T.-T. Yen, V. V. Felmetsger, M. A. Hopcroft, J. H. Kuypers, A. P. Pisano, Thermally compensated aluminum nitride Lamb wave resonators for high temperature applications, Appl. Phys. Lett. 97 (8) (2010) 083501.

[19] T. Aubert, M. B. Assouar, O. Legrani, O. Elmazria, C. Tiusan, S. Robert, Highly textured growth of AlN films on sapphire by magnetron sputtering for high temperature surface acoustic wave applications, J. Vac. Sci. Technol. A 29 (2) (2011) 021010.

[20] P. Kirsch, M. B. Assouar, O. Elmazria, V. Mortet, P. Alnot, 5 GHz surface acoustic wave devices based on aluminum nitride/diamond layered structure realized using electron beam lithography, Appl. Phys. Lett. 88 (22) (2006) 223504.

[21] V. V. Felmetsger, P. N. Laptev, R. J. Graham, Deposition of ultrathin AlN films for high frequency electroacoustic devices, J. Vac. Sci. Technol. A 29 (2) (2011) 021014.

[22] S. Fujii, High-frequency surface acoustic wave filter based on diamond thin film, Phys. Status Solidi A 208 (5) (2011) 1072 – 1077.

[23] V. Yantchev, L. Arapan, I. Katardjiev, V. Plessky, Thin-film zero-group-velocity Lamb wave resonator, Appl. Phys. Lett. 99 (3) (2011) 033505.

[24] V. Mortet, A. Soltani, A. Talbi, P. Pobedinskas, K. Haenen, J.-C. De Jaeger, P. Pernod, P. Wagner, AlN on nanocrystalline diamond piezoelectric cantilevers for sensors/actuators, Procedia Chemistry 1 (1) (2009) 40 – 43.

[25] V. Mortet, K. Haenen, J. Potmesil, M. Vanecek, M. D'Olieslaeger, Diamond – Application to piezoelectric bimorph cantilever sensors, Phys. Status Solidi A 203 (12) (2006) 3185 – 3190.

[26] O. A. Williams, V. Mortet, M. Daenen, K. Haenen, Nanocrystalline diamond enhanced thickness shear mode resonator, Appl. Phys. Lett. 90 (6) (2007) 063514.

[27] V. Mortet, O. A. Williams, K. Haenen, Diamond: A material for acoustic devices, Phys. Status Solidi A 205 (5) (2008) 1009 – 1020.

[28] F. Haussonne, Review of the synthesis methods for AlN, Mater. Manuf. Processes 10 (4) (1995) 717 – 755.

[29] N. Azéma, J. Durand, R. Berjoan, C. Dupuy, J. L. Balladore, L. Cot, Plasma-enhanced chemical vapour deposition of AlN ($10\bar{1}0$) on Si (100): Microstructural study of the interlayers, J. Cryst. Growth 129 (3 - 4) (1993) 621 – 628.

[30] A. C. Jones, S. A. Rushworth, D. J. Houlton, J. S. Roberts, V. Roberts, C. R. Whitehouse, G. W. Critchlow, Deposition of aluminum nitride thin films by MOCVD from the trimethylaluminum-ammonia adduct, Chem. Vap. Deposition 2 (1) (1996) 5 – 8.

[31] S. Shimada, M. Yoshimatsu, H. Nagai, M. Suzuki, H. Komaki, Preparation and properties of TiN and AlN films from alkoxide solution by thermal plasma CVD method, Thin Solid Films 370 (1 - 2) (2000) 137 – 145.

[32] C.-S. Oh, C.-S. Han, A Study on the preferred orientation characteristics of AlN thin films by reactive evaporation method using NH_3, Korean J. Met. Mater. 50 (1) (2012) 78 – 85.

[33] R. D. Vispute, J. Narayan, J. D. Budai, High quality optoelectronic grade epitaxial AlN films on α-Al2O3, Si and 6H-SiC by pulsed laser deposition, Thin Solid Films 299 (1-2) (1997) 94 – 103.

[34] H. Morkoç, III-Nitride semiconductor growth by MBE: Recent issues, J. Mater. Sci. - Mater. Electron. 12 (12) (2001) 677 – 695.

[35] M. Ohring, The materials science of thin films, 2nd Edition, Academic Press, 2001.

[36] A. Bogaerts, E. Neyts, R. Gijbels, J. van der Mullen, Gas discharge plasmas and their applications, Spectrochim. Acta, Part B 57 (4) (2002) 609 – 658.

[37] V. Mortet, M. Nesladek, J. D'Haen, G. Vanhoyland, O. Elmazria, M. Assouar, P. Alnot, M. D'Olieslaeger, Deposition of aluminium nitride film by magnetron sputtering for diamond-based surface acoustic wave applications, Phys. Status Solidi A 193 (3) (2002) 482 – 488.

[38] A. Guillaumot, F. Lapostolle, C. Dublanche-Tixier, J. C. Oliveira, A. Billard, C. Langlade, Reactive deposition of Al–N coatings in Ar/N_2 atmospheres using pulsed-DC or high power impulse magnetron sputtering discharges 85 (2) (2010) 120 – 125.

[39] B. W. Sheldon, A. Rajamani, A. Bhandari, E. Chason, S. K. Hong, R. Beresford, Competition between tensile and compressive stress mechanisms during Volmer-Weber growth of aluminum nitride films, J. Appl. Phys. 98 (4) (2005) 043509.

[40] F. Martin, P. Muralt, M. A. Dubois, A. Pezous, Thickness dependence of the properties of highly *c*-axis textured AlN thin films, J. Vac. Sci. Technol. A 22 (2) (2004) 361–365.

[41] R. Machunze, G. C. A. M. Janssen, Stress gradients in titanium nitride thin films, Surf. Coat. Technol. 203 (5-7) (2008) 550 – 553.

[42] C. Kittel, Introduction to solid state physics, Wiley, 2005.

[43] W. Pötz, P. Kocevar, Electronic power transfer in pulsed laser excitation of polar semiconductors, Phys. Rev. B 28 (12) (1983) 7040–7047.

[44] A. Žukauskas, Second nonequilibrium-phonon bottleneck for carrier cooling in highly excited polar semiconductors, Phys. Rev. B 57 (24) (1998) 15337–15344.

[45] M. Kazan, S. Pereira, M. R. Correia, P. Masri, Contribution of the decay of optical phonons into acoustic phonons to the thermal conductivity of AlN, Phys. Rev. B 77 (18) (2008) 180302(R).

[46] L. Bergman, D. Alexson, P. L. Murphy, R. J. Nemanich, M. Dutta, M. A. Stroscio, C. Balkas, H. Shin, R. F. Davis, Raman analysis of phonon lifetimes in AlN and GaN of wurtzite structure, Phys. Rev. B 59 (20) (1999) 12977–12982.

[47] M. Kuball, J. M. Hayes, Y. Shi, J. H. Edgar, Phonon lifetimes in bulk AlN and their temperature dependence, Appl. Phys. Lett. 77 (13) (2000) 1958–1960.

[48] J. G. Tischler, J. A. Freitas Jr, Anharmonic decay of phonons in strain-free wurtzite AlN, Appl. Phys. Lett. 85 (11) (2004) 1943–1945.

[49] P. Pandit, D. Y. Song, M. Holtz, Decay of zone-center phonons in AlN with A_1, E_1, and E_2 symmetries, J. Appl. Phys. 102 (11) (2007) 113510.

[50] M. Kazan, S. Pereira, M. R. Correia, P. Masri, Directional dependence of AlN intrinsic complex dielectric function, optical phonon lifetimes, and decay channels measured by polarized infrared reflectivity, J. Appl. Phys. 106 (2) (2009) 023523.

[51] T. Prokofyeva, M. Seon, J. Vanbuskirk, M. Holtz, S. A. Nikishin, N. N. Faleev, H. Temkin, S. Zollner, Vibrational properties of AlN grown on (111)-oriented silicon, Phys. Rev. B 63 (12) (2001) 125313.

[52] V. Darakchieva, P. P. Paskov, T. Paskova, J. Birch, S. Tungasmita, B. Monemar, Deformation potentials of the E_1(TO) mode in AlN, Appl. Phys. Lett. 80 (13) (2002) 2302–2304.

[53] P. Bergonzo, A. Bongrain, E. Scorsone, A. Bendali, L. Rousseau, G. Lissorgues, P. Mailley, Y. Li, T. Kauffmann, F. Goy, B. Yvert, J. A. Sahel, S. Picaud, 3D shaped mechanically flexible diamond microelectrode arrays for eye implant applications: The MEDINAS project, IRBM 32 (2) (2011) 91 – 94.

[54] M. Dankerl, B. Hofmann, S. Eick, M. Hauf, S. Ingebrandt, A. Offenhäuser, M. Stutzmann, J. A. Garrido, Diamond transistor array for extracellular recording from electrogenic cells, Adv. Funct. Mater. 19 (18) (2009) 2915 – 2923.

[55] O. A. Williams, V. Mortet, M. Daenen, K. Haenen, The diamond nano-balance, J. Nanosci. Nanotechnol. 9 (6) (2009) 3483 – 3486.

[56] O. A. Williams, M. Nesladek, M. Daenen, S. Michaelson, A. Hoffman, E. Ōsawa, K. Haenen, R. B. Jackman, Growth, electronic properties and applications of nanodiamond, Diam. Relat. Mater. 17 (7 - 10) (2008) 1080 – 1088.

[57] O. A. Williams, O. Douhéret, M. Daenen, K. Haenen, E. Ōsawa, M. Takahashi, Enhanced diamond nucleation on monodispersed nanocrystalline diamond, Chem. Phys. Lett. 445 (4 - 6) (2007) 255 – 258.

[58] O. A. Williams, J. Hees, C. Dieker, W. Jager, L. Kirste, C. E. Nebel, Size-dependent reactivity of diamond nanoparticles, ACS Nano 4 (8) (2010) 4824 – 4830.

[59] T. Manzaneque, J. Hernando, L. Rodríguez-Aragón, A. Ababneh, H. Seidel, U. Schmid, J. L. Sánchez-Rojas, Analysis of the quality factor of AlN-actuated micro-resonators in air and liquid, Microsystem Technologies 16 (5) (2010) 837 – 845.

[60] K. Wasa, M. Kitabatake, H. Adachi, Thin film materials technology, William Andrew, 2004.

[61] P. B. Barna, M. Adamik, Fundamental structure forming phenomena of polycrystalline films and the structure zone models, Thin Solid Films 317 (1 - 2) (1998) 27 – 33.

[62] S. Mahieu, P. Ghekiere, D. Depla, R. De Gryse, Biaxial alignment in sputter deposited thin films, Thin Solid Films 515 (4) (2006) 1229 – 1249.

[63] G. Stoney, The tension of metallic films deposited by electrolysis, Proc. R. Soc. A 82 (1909) 172–175.

[64] G. C. A. M. Janssen, M. M. Abdalla, F. van Keulen, B. R. Pujada, B. van Venrooy, Celebrating the 100th anniversary of the Stoney equation for film stress: Developments from polycrystalline steel strips to single crystal silicon wafers, Thin Solid Films 517 (6) (2009) 1858 – 1867.

[65] M. A. Hopcroft, W. D. Nix, T. W. Kenny, What is the Young's modulus of silicon?, J. Microelectromech. Syst. 19 (2) (2010) 229 – 238.

[66] R. Thokala, J. Chaudhuri, Calculated elastic constants of wide band gap semiconductor thin films with a hexagonal crystal structure for stress problems, Thin Solid Films 266 (2) (1995) 189 – 191.

[67] W. H. Press, B. P. Flannery, S. A. Teukolsky, W. T. Vetterling, Numerical recipes in C: The art of scientific computing, 2nd Edition, Cambridge University Press, 1992.

[68] R. M. A. Azzam, N. M. Bashara, Ellipsometry and polarized light, North-Holland, 1987.

[69] A. Vašíček, Optics of thin films, North-Holland, 1960.

[70] D. Den Engelsen, Ellipsometry of anisotropic films, J. Opt. Soc. Am. 61 (11) (1971) 1460–1466.

[71] I. Filiński, The effects of sample imperfections on optical spectra, Phys. Status Solidi B 49 (2) (1972) 577 – 588.

[72] F. Peter, Über Brechungsindizes und Absorptionskonstanten des Diamanten zwischen 644 und 226 um, Z. Phys. 15 (1) (1923) 358 – 368.

[73] J. Pastrňák, L. Roskovcová, Refraction index measurements on AlN single crystals, Phys. Status Solidi B 14 (1) (1966) K5–K8.

[74] R. Swanepoel, Determination of the thickness and optical constants of amorphous silicon, J. Phys. E 16 (12) (1983) 1214–1222.

[75] M. Schubert, Infrared ellipsometry on semiconductor layer structures: Phonons, plasmons, and polaritons, Springer-Verlag, 2004.

[76] B. K. Ridley, Electrons and phonons in semiconductor multilayers, Cambridge University Press, 2009.

[77] R. S. Mulliken, Report on notation for the spectra of polyatomic molecules, J. Chem. Phys. 23 (11) (1955) 1997, ibid. **24**, 1118(E) (1956).

[78] V. Yu. Davydov, Yu. E. Kitaev, I. N. Goncharuk, A. N. Smirnov, J. Graul, O. Semchinova, D. Uffmann, M. B. Smirnov, A. P. Mirgorodsky, R. A. Evarestov, Phonon dispersion and Raman scattering in hexagonal GaN and AlN, Phys. Rev. B 58 (19) (1998) 12899 – 12907.

[79] D. W. Berreman, Infrared absorption at longitudinal optic frequency in cubic crystal films, Phys. Rev. 130 (6) (1963) 2193 – 2198.

[80] A. S. Barker, Transverse and longitudinal optic mode study in MgF_2 and ZnF_2, Phys. Rev. 136 (5A) (1964) A1290–A1295.

[81] D. W. Berreman, F. C. Unterwald, Adjusting poles and zeros of dielectric dispersion to fit reststrahlen of $PrCl_3$ and $LaCl_3$, Phys. Rev. 174 (3) (1968) 791–799.

[82] R. P. Lowndes, Influence of lattice anharmonicity on the longitudinal optic modes of cubic ionic solids, Phys. Rev. B 1 (6) (1970) 2754–2763.

[83] F. Gervais, B. Piriou, Anharmonicity in several-polar-mode crystals: Adjusting phonon self-energy of LO and TO modes in Al_2O_3 and TiO_2 to fit infrared reflectivity, J. Phys. C 7 (13) (1974) 2374–2386.

[84] M. Fox, Optical properties of solids, Oxford University Press, 2001.

[85] T. C. Damen, S. P. S. Porto, B. Tell, Raman effect in zinc oxide, Phys. Rev. 142 (2) (1966) 570 – 574.

[86] V. Yu. Davydov, N. S. Averkiev, I. N. Goncharuk, D. K. Nelson, I. P. Nikitina, A. S. Polkovnikov, A. N. Smirnov, M. A. Jacobson, Raman and photoluminescence studies of biaxial strain in GaN epitaxial layers grown on 6H-SiC, J. Appl. Phys. 82 (10) (1997) 5097 – 5102.

[87] W. A. Kern, D. A. Poutinen, Cleaning solutions based on hydrogen peroxide for use in silicon semiconductor technology, RCA Rev. 31 (1970) 187 – 206.

[88] E. Valcheva, J. Birch, P. O. Å. Persson, S. Tungasmita, L. Hultman, Epitaxial growth and orientation of AlN thin films on Si(001) substrates deposited by reactive magnetron sputtering, J. Appl. Phys. 100 (12) (2006) 123514.

[89] J. Meinschien, F. Falk, R. Hergt, H. Stafast, Distinct orientation of AlN thin films deposited on sapphire substrates by laser ablation, Appl. Phys. A 70 (2) (2000) 215 – 218.

[90] G. C. A. M. Janssen, A. J. Dammers, V. G. M. Sivel, W. R. Wang, Tensile stress in hard metal films, Appl. Phys. Lett. 83 (16) (2003) 3287 – 3289.

[91] E. Chason, B. W. Sheldon, L. B. Freund, J. A. Floro, S. J. Hearne, Origin of compressive residual stress in polycrystalline thin films, Phys. Rev. Lett. 88 (15) (2002) 156103.

[92] H. J. Motulsky, L. A. Ransnas, Fitting curves to data using nonlinear regression: A practical and nonmathematical review, FASEB J. 1 (5) (1987) 365 – 374.

[93] J. M. Wagner, F. Bechstedt, Properties of strained wurtzite GaN and AlN: *Ab initio* studies, Phys. Rev. B 66 (11) (2002) 115202.

[94] L. E. McNeil, M. Grimsditch, R. H. French, Vibrational spectroscopy of aluminum nitride, J. Am. Ceram. Soc. 76 (5) (1993) 1132 – 1136.

[95] C. Deger, E. Born, H. Angerer, O. Ambacher, M. Stutzmann, J. Hornsteiner, E. Riha, G. Fischerauer, Sound velocity of $Al_xGa_{1-x}N$ thin films obtained by surface acoustic-wave measurements, Appl. Phys. Lett. 72 (19) (1998) 2400 – 2402.

[96] K. Tsubouchi, N. Mikoshiba, Zero-temperature-coefficient SAW devices on AlN epitaxial films, IEEE Trans. Sonics Ultrason. 32 (5) (1985) 634 – 644.

[97] K. Kim, W. R. L. Lambrecht, B. Segall, Elastic constants and related properties of tetrahedrally bonded BN, AlN, GaN, and InN, Phys. Rev. B 53 (24) (1996) 16310 – 16326, ibid. **56**, 7018(E) (1997).

[98] E. Ruiz, S. Alvarez, P. Alemany, Electronic structure and properties of AlN, Phys. Rev. B 49 (11) (1994) 7115 – 7123.

[99] A. F. Wright, Elastic properties of zinc-blende and wurtzite AlN, GaN, and InN, J. Appl. Phys. 82 (6) (1997) 2833 – 2839.

[100] K. Shimada, T. Sota, K. Suzuki, First-principles study on electronic and elastic properties of BN, AlN, and GaN, J. Appl. Phys. 84 (9) (1998) 4951 – 4958.

[101] R. Kato, J. Hama, First-principles calculation of the elastic stiffness tensor of aluminium nitride under high pressure, J. Phys.: Condens. Matter 6 (38) (1994) 7617 – 7632.

[102] H. Angerer, D. Brunner, F. Freudenberg, O. Ambacher, M. Stutzmann, Determination of the Al mole fraction and the band gap bowing of epitaxial $Al_xGa_{1-x}N$ films, Appl. Phys. Lett. 71 (11) (1997) 1504 – 1506.

[103] R. C. Cammarata, T. M. Trimble, D. J. Srolovitz, Surface stress model for intrinsic stresses in thin films, J. Mater. Res. 15 (11) (2000) 2468 – 2474.

[104] T. Metzger, R. Höpler, E. Born, O. Ambacher, M. Stutzmann, R. Stömmer, M. Schuster, H. Göbel, S. Christiansen, M. Albrecht, H. P. Strunk, Defect structure of epitaxial GaN films determined by transmission electron microscopy and triple-axis X-ray diffractometry, Philos. Mag. A 77 (4) (1998) 1013 – 1025.

[105] E. P. Pokatilov, D. L. Nika, A. A. Balandin, Phonon spectrum and group velocities in AlN/GaN/AlN and related heterostructures, Superlattices Microstruct. 33 (3) (2003) 155 – 171.

[106] S. Barman, G. P. Srivastava, Long-wavelength nonequilibrium optical phonon dynamics in cubic and hexagonal semiconductors, Phys. Rev. B 69 (23) (2004) 235208.

[107] G. P. Srivastava, The anharmonic phonon decay rate in group-III nitrides, J. Phys.: Condens. Matter 21 (17) (2009) 174205.

[108] V. Mortet, M. Nesladek, K. Haenen, A. Morel, M. D'Olieslaeger, M. Vanecek, Physical properties of polycrystalline aluminium nitride films deposited by magnetron sputtering, Diamond Relat. Mater. 13 (4-8) (2004) 1120 – 1124.

[109] M. Kuball, J. M. Hayes, Y. Shi, J. H. Edgar, A. D. Prins, N. W. A. van Uden, D. J. Dunstan, Raman scattering studies on single-crystalline bulk AlN, J. Cryst. Growth 231 (3) (2001) 391 – 396.

[110] A. Artieda, M. Barbieri, C. S. Sandu, P. Muralt, Effect of substrate roughness on *c*-oriented AlN thin films, J. Appl. Phys. 105 (2) (2009) 024504.

[111] K. R. Williams, K. Gupta, M. Wasilik, Etch rates for micromachining processing–Part II, J. Microelectromech. S. 12 (6) (2003) 761 – 778.

[112] M. Morita, T. Ohmi, E. Hasegawa, M. Kawakami, M. Ohwada, Growth of native oxide on a silicon surface, J. Appl. Phys. 68 (3) (1990) 1272 – 1281.

[113] Y. I. Rabinovich, J. J. Adler, A. Ata, R. K. Singh, B. M. Moudgil, Adhesion between nanoscale rough surfaces: I. Role of asperity geometry, J. Colloid Interface Sci. 232 (1) (2000) 10 – 16.

[114] H. A. Girard, S. Perruchas, C. Gesset, M. Chaigneau, L. Vieille, J.-C. Arnault, P. Bergonzo, J.-P. Boilot, T. Gacoin, Electrostatic grafting of diamond nanoparticles: A versatile route to nanocrystalline diamond thin films, ACS Appl. Mater. Interfaces 1 (12) (2009) 2738 – 2746.

Publications

Papers

1. **P. Pobedinskas**, G. Degutis, W. Dexters, C. De Dobbelaere, S.D. Janssens, J. D'Haen, A. Hardy, M.K. Van Bael, and K. Haenen, *The influence of surface plasma pretreatments on diamond nucleation*, in preparation (2012).

2. **P. Pobedinskas**, J.-C. Bolsée, W. Dexters, B. Ruttens, V. Mortet, J. D'Haen, J.V. Manca, and K. Haenen, *Thickness dependent residual stress in sputtered AlN thin films*, submitted to Thin Solid Films (2012).

3. **P. Pobedinskas**, B. Ruttens, J. D'Haen, and K. Haenen, *Optical phonon lifetimes in sputtered AlN thin films*, accepted for publication in Applied Physics Letters 100 (19) (2012).

4. M.J. Oliver, J. Hernando-García, A. Ababneh, H. Seidel, U. Schmid, J.P. Andrés, **P. Pobedinskas**, K. Haenen and J.L. Sánchez-Rojas, *Resonantly excited AlN-based microcantilevers for immunosensing*, accepted for publication in Microsystem Technologies (2012).

5. D. Croux, A. Weustenraed, **P. Pobedinskas**, F. Horemans, H. Diliën, K. Haenen, T. Cleij, P. Wagner, R. Thoelen, and W. De Ceuninck, *Development of multichannel quartz crystal microbalances for MIP-based biosensing*, online in Physica Status Solidi A (2012).

6. M.J. Oliver, J. Hernando-García, **P. Pobedinskas**, K. Haenen, A. Rios, and J.L. Sánchez-Rojas, *Reusable chromium-coated quartz crystal microbalance for immunosensing*, Colloids and Surfaces B: Biointerfaces 88 (1) (2011) 191 – 195.

7. S.D. Janssens, **P. Pobedinskas**, J. Vacik, V. Petrakova, B. Ruttens, J. D'Haen, M. Nesládek, K. Haenen, and P. Wagner, *Separation of intra- and intergranular magnetotransport properties in nanocrystalline diamond films on the metallic side of the metal-insulator transition*, New Journal of Physics 13 (8) (2011) 083008.

Proceedings

1. **P. Pobedinskas**, S.D. Janssens, J. Hernando, P. Wagner, M. Nesládek, and K. Haenen, *Selective seeding and growth of nanocrystalline CVD diamond on non-diamond substrates*, MRS Online Proceedings Library 1339 (2001) mrss11-1339-S04-02. DOI: 10.1557/opl.2011.992

2. S.D. Janssens, **P. Pobedinskas**, V. Petráková, M. Nesládek, K. Haenen, and P. Wagner, *Influence of methane concentration on the electric transport properties in heavily boron-doped nanocrystalline CVD diamond films*, MRS Symposium Proceedings Volume 1282 (2011) 1282-A15-04, 87 – 92. In "Diamond Electronics and Bioelectronics – Fundamentals to Applications IV", Eds. P. Bergonzo, J.E. Butler, C.E. Nebel, M. Nesládek, and A.T.S. Wee, ISBN 978-1-60511-259-6.

3. R. Salenbien, J. Sermeus, **P. Pobedinskas**, C. Glorieux, and K. Haenen, *Thin nano- and microcrystalline CVD diamond films for micro-channel cooling: thermal and elastic properties*, MRS Symposium Proceedings Volume 1282 (2011) 1282-A15-02, 79 – 85. In "Diamond Electronics and Bioelectronics – Fundamentals to Applications IV", Eds. P. Bergonzo, J.E. Butler, C.E. Nebel, M. Nesládek, and A.T.S. Wee, ISBN 978-1-60511-259-6.

4. M.J. Oliver, J. Hernando-García, A. Ababneh, H. Seidel, U. Schmid, J. Olivares, E. Iborra, **P. Pobedinskas**, K. Haenen, and J.L. Sánchez-Rojas, *Resonant piezoelectric AlN-actuated microcantilevers for detection of antigen/antibody interactions*, Proceedings of SPIE 8066 (2011) 80661A. In "Smart sensors, actuators, and MEMS V", Eds. U. Schmid, J.L. Sánchez-Rojas, and M. Leester-Schaedel, ISBN 978-0-81948-655-4.

5. V. Mortet, A. Soltani, A. Talbi, **P. Pobedinskas**, K. Haenen, J.-C. De Jaeger, P. Pernod, and P. Wagner, *AlN on nanocrystalline diamond piezoelectric cantilevers for sensors/actuators*, Procedia Chemistry 1 (1) (2009) 40 – 43.

Abstracts

Oral presentations

1. **P. Pobedinskas**, G. Degutis, W. Dexters, S.D. Janssens, J. D'Haen, A. Hardy, M.K. Van Bael, and K. Haenen, *The role of surface plasma pre-treatments in enhanced diamond nucleation*, The 6th International Conference on New Diamond and Nano Carbons (NDNC2012), San Juan, USA, 20–24/05/2012.

2. **P. Pobedinskas**, G. Degutis, W. Dexters, C. De Dobbelaere, S.D. Janssens, J. D'Haen, A. Hardy, M.K. Van Bael, and K. Haenen, *The influence of surface plasma pretreatments on diamond nucleation*, Hasselt Diamond Workshop (SBDD XVII), Hasselt, Belgium, 14–16/03/2012.

3. Z. Vlčková Živcová, O. Frank, V. Petrák, H. Tarábková, W. Janssen, **P. Pobedinskas**, K. Haenen, M. Nesládek, and L. Kavan, *Electrochemistry and in-situ Raman spectroelectrochemistry of low and high quality boron doped diamond layers in aqueous electrolyte solutions*, Hasselt Diamond Workshop (SBDD XVII), Hasselt, Belgium, 14–16/03/2012.

4. **P. Pobedinskas**, *Optical properties of nanocrystalline diamond thin films*, MATCON (Materials and Interfaces for Energy Storage and Conversion) Winter School (FP7-ITN-project), Freiburg im Breisgau, Germany, 20–24/02/2012.

5. S.D. Janssens, **P. Pobedinskas**, A. Taylor, V. Petráková, J. Vacik, J. D'Haen, F. Fendrych, P. Wagner, M. Nesládek, and K. Haenen, *Influence of Granularity on the Magnetotransport Properties of Thin B-Doped Nanocrystalline CVD Diamond Films*, The 5th International Conference on Innovations in Thin Films Processing and Characterisation (ITFPC2011) and the 2nd edition of Magnetrons, Ion beam processing & Arc Technologies European Conference (MIATEC2011), Nancy, France, 14–17/11/2011.

6. S.D. Janssens, **P. Pobedinskas**, J. Vacik, V. Petráková, J. D'Haen, M. Nesládek, P. Wagner, and K. Haenen, *Separation of the intra- and intergranular magnetotransport properties in heavily B-doped nanocrystalline CVD diamond films*, The 62nd Diamond Conference, Warwick, UK, 04–07/07/2011.

7. L. Goris, **P. Pobedinskas**, H.-G. Boyen, D. Vanderzande, M. Nesládek, and K. Haenen, *Realization of functional boron doped CVD diamond layers for solar absorbers: Dye design principles and coupling strategy*, The 5th International Conference on New Diamond and Nano Carbons (NDNC2011), Matsue, Japan, 16–20/05/2011.

8. **P. Pobedinskas**, S.D. Janssens, J. Hernando-García, P. Wagner, M. Nesládek, and K. Haenen, *Selective seeding and growth of nanocrystalline CVD diamond on non-diamond substrates*, MRS 2011 Spring Meeting Symposium S: Plasma-Assisted Materials Processing and Synthesis, San Francisco, USA, 25–29/04/2011.

9. L. Goris, **P. Pobedinskas**, H.-G. Boyen, D. Vanderzande, M. Nesládek, and K. Haenen, *Synthetic pathways, bonding mechanism and optical characteristics of dye functionalized CVD diamond layers*, MRS 2011 Spring Meeting Symposium QQ: Carbon Functional Interfaces, San Francisco, USA, 25–29/04/2011.

10. M.J. Oliver, J. Hernando-García, A. Ababneh, H. Seidel, U. Schmid, J. Olivares, E. Iborra, **P. Pobedinskas**, K. Haenen, and J.L. Sánchez-Rojas, *Resonant piezoelectric AlN-actuated microcantilevers for detection of antigen/antibody interactions*, SPIE Microtechnologies, Prague, Czech Republic, 18–20/04/2011.

11. R. Salenbien, B. Verstraeten, **P. Pobedinskas**, S.D. Jannssens, C. Glorieux, and K. Haenen, *Thin nanocrystalline CVD diamond films for micro-channel cooling: thermal and elastic properties*, MRS 2010 Fall Meeting Symposium A: Diamond Electronics and Bioelectronics – Fundamentals to Applications IV, Boston, USA, 29/11–03/12/2010.

12. M.J. Oliver, J. Hernando-García, **P. Pobedinskas**, K. Haenen, J. Olivares, E. Iborra, and J.L. Sánchez-Rojas, *Sputtered polycrystalline AlN as a platform for biosensing*, IV Workshop Nanociencia y Nanotecnología Analíticas (IV NyNA 2010), Zaragoza, Spain, 07–09/09/2010.

13. R. Salenbien, B. Verstraeten, **P. Pobedinskas**, S.D. Jannssens, C. Glorieux, and K. Haenen, *Thermal and elastic properties of thin film nanocrystalline CVD diamond films*, The 21st European Conference on Diamond, Diamond-like Materials, Carbon Nanotubes, and Nitrides, Budapest, Hungary, 05–09/09/2010.

14. A. Soltani, A. Talbi, J.-C. Gerbedoen, J.-C. De Jaeger, V. Mortet, **P. Pobedinskas**, K. Haenen, A. BenMoussa, J.-F. Hochedez, and W.J. Zhang, *Diamond and cubic boron nitride: properties, growth and applications*, E-MRS 2010 Spring Meeting, Strasbourg, France, 07–11/06/2010.

Poster presentations

1. **P. Pobedinskas**, G. Degutis, W. Dexters, C. De Dobbelaere, S.D. Janssens, J. D'Haen, A. Hardy, M.K. Van Bael, and K. Haenen, *Enhanced diamond nucleation by surface plasma pretreatments*, E-MRS 2012 Spring Meeting, Strasbourg, France, 14–18/05/2012.

2. G. Degutis, **P. Pobedinskas**, W. Dexters, C. De Dobbelaere, W. Janssen, S. Al-Riyami, T. Yoshitake, J. D'Haen, A. Hardy, K. Haenen, M.K. Van'Bael, *The nucleation and growth of nanocrystalline diamond on metal interlayers*, Hasselt Diamond Workshop (SBDD XVII), Hasselt, Belgium, 14–16/03/2012.

3. **P. Pobedinskas**, J. D'Haen, and K. Haenen, *Thickness Dependent Frequency and Lifetime Behaviour of Optical Phonons in Thin AlN Films*, The 5th International Conference on Innovations in Thin Films Processing and Characterisation (ITFPC2011) and the 2nd edition of Magnetrons, Ion beam processing & Arc Technologies European Conference (MIATEC2011), Nancy, France, 14–17/11/2011.

4. **P. Pobedinskas**, J. D'Haen, and K. Haenen, *Optical phonons in thin AlN films: Thickness dependent frequency and lifetime behaviour*, The 22nd European Conference on Diamond, Diamond-like Materials, Carbon Nanotubes, and Nitrides, Garmisch-Partenkirchen, Germany, 04–08/09/2011.

5. **P. Pobedinskas**, V. Mortet, and K. Haenen, *Thickness dependent stress and strain in polycrystalline aluminium nitride thin films*, The 21st European Conference on Diamond, Diamond-like Materials, Carbon Nanotubes, and Nitrides, Budapest, Hungary, 05–09/09/2010.

6. **P. Pobedinskas**, V. Mortet, and K. Haenen, *Stress gradient in polycrystalline aluminum nitride thin films*, Hasselt Diamond Workshop (SBDD XV), Hasselt, Belgium, 22–24/02/2010.

7. S.D. Janssens, **P. Pobedinskas**, K. Haenen, and P. Wagner, *The influence of methane on the boron incorporation and resistivity in B-doped nanocrystalline diamond films*, Hasselt Diamond Workshop (SBDD XV), Hasselt, Belgium, 22–24/02/2010.

8. S.D. Janssens, **P. Pobedinskas**, V. Mortet, K. Haenen, and P. Wagner, *The influence of methane concentration on the structure and transport properties of B-doped nanocrystalline CVD diamond films*, MRS 2009 Fall Meeting Symposium J: Diamond Electronics and Bioelectronics – Fundamentals to Applications III, Boston, USA, 30/11–04/12/2009.

9. **P. Pobedinskas**, V. Mortet, and K. Haenen, *Thickness dependent residual stress in polycrystalline aluminum nitride thin films*, Innovations in Thin Film Processing and Characterisation (ITFPC2009), Nancy, France, 17–20/11/2009.

10. R. Salenbien, C. Glorieux, **P. Pobedinskas**, S.D. Janssens, V. Mortet, and K. Haenen, *Determination of the thermo-elastic properties of thin nanocrystalline CVD diamond films for heat spreading applications*, The 15th International Workshop on Thermal Investigations on IC's and Systems (Therminic 2009), Leuven, Belgium, 07–09/10/2009.

11. S.D. Janssens, **P. Pobedinskas**, V. Mortet, K. Haenen, and P. Wagner, *The influence of methane on the boron incorporation in B-doped nanocrystalline diamond films*, The 20th European Conference on Diamond, Diamond-like Materials, Carbon Nanotubes, and Nitrides, Athens, Greece, 06–10/09/2009.

12. V. Mortet, A. Soltani, A. Talbi, **P. Pobedinskas**, K. Haenen, J.C. De Jaeger, P. Pernod, and P. Wagner, *AlN on nanocrystalline diamond piezoelectric cantilevers for sensors/actuators*, Eurosensors XXIII conference, Lausanne, Switzerland, 06–09/09/2009.

Awards

Best Student Poster Prize
For P. Pobedinskas, V. Mortet, and K. Haenen, *Thickness dependent stress and strain in polycrystalline aluminium nitride thin films*, at the 21st European Conference on Diamond, Diamond-like Materials, Carbon Nanotubes, and Nitrides, Budapest, Hungary, 05–09/09/2010.

Student Grant from the Societé Française du Vide (SFV)
For P. Pobedinskas, V. Mortet, and K. Haenen, *Thickness dependent residual stress in polycrystalline aluminum nitride thin films*, at Innovations in Thin Film Processing and Characterisation 2009 (ITFPC09), Nancy, France, 17–20/11/2009.